Catch me if you can: understanding the crosstalk of hypoxia metabolism and chromatin dynamics

Inaugural-Dissertation zur

Erlangung des Doktorgrades

der Mathematisch-Naturwissenschaftlichen Fakultät der

Universität zu Köln

vorgelegt von

Claudia Tonantzi Sandoval Silva

aus Mexico City, Mexico

Köln, October 2023

Berichterstatter: Prof. Dr. Peter Tessarz

Prof. Dr. Niels Gehring

Prüfungsvorsitzender: Prof. Dr. Jan Riemer

Tag der Disputation:

ACKNOWLEDGMENTS

Taking the Ph.D. road has been one of the most challenging and fruitful experiences of my life. And I would like to thank you all for your support and guidance. I will be forever grateful.

Undoubtedly, I would first like to thank my supervisor Dr. Peter Tessarz, who has guided me in this scientific endeavor since I was a master's student. I deeply appreciate the constant support, corrections, and calmness throughout all stages of this project. Thanks for supporting me during the project pitfalls and guiding me through them to find the solutions that would improve the research scope and make me grow as a scientist. Last but not least, thanks for supporting and trusting me whenever I decided to pursue parallel professional activities to my Ph.D. project.

A huge thanks to the members of my thesis advisory committee: Dr. Lena Pernas and Dr. Ivan Matic, for the fruitful discussions and amazing feedback.

I would like to thank the members of my thesis defense committee: Prof. Niels Gehring for accepting to be the second reviewer and examiner of my thesis, and Prof. Jan Riemer for accepting to be the chair of my thesis defense committee. Special thanks to Dr. Chrysa Nikopoulou for accepting to take the defense's minutes.

Of course, a huge thanks to the Core Facilities of MPI AGE. To the Metabolomics Core Facility, especially Dr. Patrick Giavalisco, Dr. Frederik Dethloff and Yvonne Hinze. To the Proteomics Core Facility, especially Dr. Xinping Li and Dr. Ilian Atanassov. To the FACS and Imaging Core Facility, especially Dr. Christian Kukat and Marcel Kirchner. To the Bioinformatics Core Facility, especially Dr. Jorge Boucas and Ayesha Iqbal.

A big thanks to the Tessarz lab (present and past), specially to the amazing and beloved Dr. Chrysa Nikopoulou (the most incredible friend and colleague), Dr. Andromachi Pouikli, and Marjana Ndoci. To the wonderful Katrin Schmitz, Niklas Kleinenkuhnen, Dr. Arthur Fischbach, Dr. Swati Parekh, Dr. Julia Mawer, Niklas Grabenhorst, and Alexander Sporleder. A big thanks to Lillian Muwonge-Mukasa and Marialena Vathi, to whom I had the amazing opportunity to supervise.

An immense thanks to the Ph.D. Coordinator Dr. Daniela Morick for her invaluable support. To the Demetriades lab, Antebi lab, and Langer lab, for sharing lab supplies, equipment and being solvers of uncountable spontaneous experimental setbacks.

Certainly, the Ph.D. difficulties were alleviated by the presence (physical or digital) of many lovely people. An endlessly thanks to my kind and loving parents Roselba and “Peri”, and my brother “Toto”. To my grandparents, aunts and uncles, who have always been a wonderful companion in every imaginable, funny and not-that-funny situation. To my fantastic cousins with whom I fall down laughing and cherish to see growing up.

To my friends in Mexico and Germany, I will always be grateful to have you in my life. Thanks for being with me throughout these years, for some even decades, filled with uncountable joyful memories. Thanks for showing me what intercontinental love means!

I have always been amazed by nature’s wonders, the ones that happen outside and inside the lab. Certainly, doing a Ph.D. allowed me to get full immersion into the wonders of cell biology, and for that, I will be forever grateful. Thank you all for being part of this ride!

TABLE OF CONTENTS

1 ABSTRACT

The crosstalk of metabolism and chromatin plays a central role in cellular homeostasis and the adaptative response to the environment. Hypoxia is a low oxygen condition developed when cells are exposed to oxygen levels below their functional range. These hypoxic conditions generate a concomitant metabolic and transcriptional response characterized by increasing glucose metabolism and reducing TCA cycle activity. Although the cellular response to hypoxia has been extensively characterized, recent studies have revealed a more diversified metabolic adaptation to these low oxygen conditions. Here we study how hypoxia impacts the interplay between chromatin modifications and intracellular metabolite cycling in fibroblasts cultured at 2% O_2. Using a multi-omics approach, we found that deficiency of the HIF1α-target PDHK1 - a well-known inhibitor of acetyl-CoA synthesis in mitochondria - rewires use of glucose-derived acetyl-CoA to enhance FA synthesis and diminish H3K27ac. This occurs via a coordinated lipid-specific posttranscriptional response. Taken together, our data identify a new role for PDHK1 in the regulation of acetyl-CoA metabolism and provides further evidence for a close link between histone acetylation and lipid biogenesis.

KURZZUSAMMENFASSUNG

Das Zusammenspiel von Metabolismus und Chromatin spielt eine zentrale Rolle für die zelluläre Homöostase und die Anpassungsfähigkeit von Zellen an ihre Umwelt. Hypoxie ist ein sauerstoffarmer Zustand, der entsteht, wenn Zellen einem Sauerstoffgehalt ausgesetzt sind, der unter ihrem normalen Funktionsbereich liegt. Diese hypoxischen Bedingungen führen zu einer gleichzeitigen Änderung des Stoffwechsels und Genexpression, die durch eine Steigerung des Glukosestoffwechsels und eine Verringerung der Zitratzyklusaktivität gekennzeichnet ist. Obwohl die zelluläre Reaktion auf Hypoxie bereits umfassend charakterisiert wurde, haben neuere Studien eine komplexere metabolische Anpassung an diese sauerstoffarmen Bedingungen aufgezeigt. Hier untersuchen wir, wie sich Hypoxie auf das Zusammenspiel zwischen Chromatinmodifikationen und intrazellulärem Metabolismus in Fibroblasten auswirkt, die bei 2 % O2 kultiviert werden. Mithilfe eines Multi-omics-Ansatzes haben wir herausgefunden, dass ein Mangel des HIF1α-Zielmoleküls PDHK1 - ein bekannter Inhibitor der Acetyl-CoA-Synthese in Mitochondrien - die Verwendung von aus Glukose gewonnenem Acetyl-CoA ändert. Geringere PDHK1 Niveaus erhöhen die FA-Synthese und verringern die Histonmodifikation H3K27ac. Interessanterweise wird dies auf posttranslationaler Ebene reguliert. Zusammengenommen zeigen unsere Daten eine neue Rolle für PDHK1 bei der Regulierung des Acetyl-CoA-Stoffwechsels und liefern weitere Beweise für eine enge Verbindung zwischen Histonazetylierung und Lipidbiogenese.

2 INTRODUCTION

2.1 Chromatin and histone PTMs

Chromatin is the dynamic structure that allows eukaryotic gene regulation and genome packaging into the nucleus (Bannister & Kouzarides, 2011). Nucleosomes are chromatin's core unit, consisting of DNA fragments of ~147 bp wrapped around an octamer of histone dimers (H2A, H2B, H3, and H4) (Dombrowski et al., 2022; McGinty & Tan, 2015). Short histone-free DNA regions (~20–50 bp) known as "linker DNA" connect individual nucleosomes and form nucleosomal arrays (Chakravarthy et al., 2005; McGinty & Tan, 2015). Nucleosomes form stable complexes due to the ionic nature of the phosphate backbone of DNA and the high content of basic residues within histones (Korolev et al., 2007). Loosening the DNA-histone interaction increases accessibility to the DNA (Korolev et al., 2007; Tessarz & Kouzarides, 2014). Accessible DNA allows the interaction with the cellular machinery in charge of DNA-templated processes, such as DNA repair, replication, and transcription (Adkins et al., 2004; Baldi et al., 2020). The differential accessibility of DNA within the nucleosomal configuration is dynamic, responds to internal and external stimuli, and plays crucial roles in regulating transcriptional responses (Bannister & Kouzarides, 2011). Hence, it is essential for a broad range of adaptive processes that, for instance, regulate cellular differentiation or maintenance of cellular identity (Bannister & Kouzarides, 2011).

Histone posttranslational modifications (PTMs) represent one mechanism that regulates chromatin structure and function (Adkins et al., 2004; Bannister & Kouzarides, 2011; Tessarz & Kouzarides, 2014). With a continuously growing histone PTM catalog, acetylation, methylation, and phosphorylation represent the best-characterized PTMs (Bannister & Kouzarides, 2011). Based on their chemical nature, location and stability within chromatin, histone PTMs mediate a plethora of functions that range from transcriptional activation/deactivation at local (e.g., promoter) and distant scales (e.g., enhancers) to chromosome condensation as preparation for mitosis (Figure 1) (Andonegui-Elguera et al., 2022; Ramazi et al., 2020; Zhang et al., 2015; Zhou et al., 2011). Many histone modifications are located in the terminal tails of the histone octamer that protrude out of the nucleosome core (Ali et al., 2018; Li et al., 2018). However, histone PTMs can also be located at the globular histone core (Li et al., 2018). Two main mechanisms, not mutually exclusive, dictate how histone PTMs modulate chromatin. The first one comprises a direct structural

modification of the histone-DNA or histone-histone contact sites that increases accessibility to the DNA and facilitates gene expression (Tessarz & Kouzarides, 2014; Zhang et al., 2015). The second one consists of the recruitment of ATP-chromatin remodelers that reorganize the nucleosomal architecture through changes in nucleosome positioning (Tessarz & Kouzarides, 2014; Zhang et al., 2015).

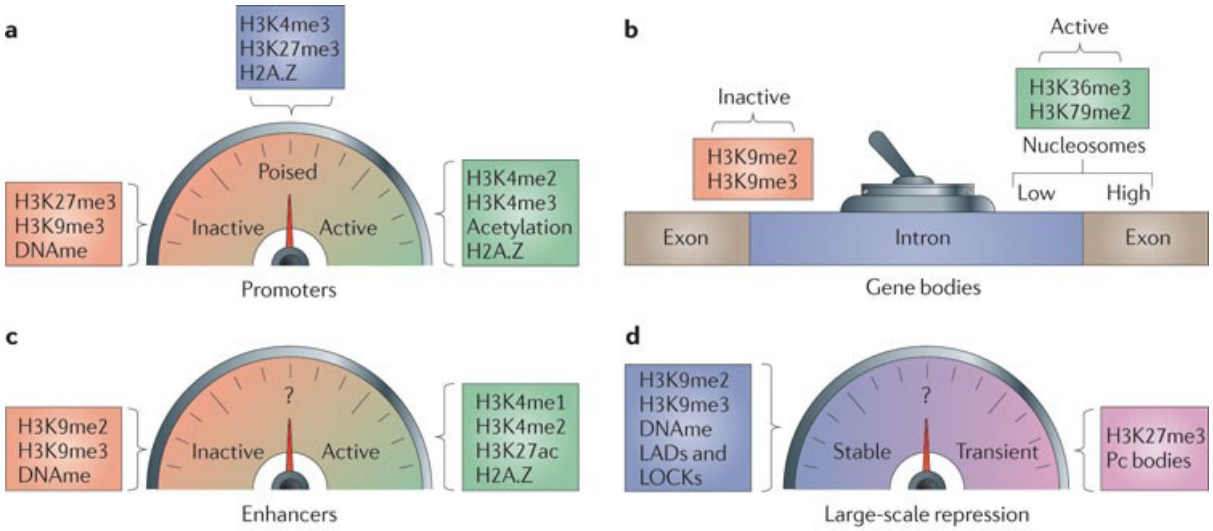

Figure 1. Histone PTMs and their functional outcomes within different chromatin regions

Schematic of representative histone PTMs associated to **(A)** promoters, **(B)** gene bodies, **(C)** enhancers, and **(D)** large-scale repression regions. Figure obtained from Zhou *et al.* (Zhou et al., 2011).

Histone acetylation is an abundant and dynamic modification that promotes open chromatin and gene activation (Shvedunova & Akhtar, 2022; Zhou et al., 2011). This modification is reversible and regulated by histone acetyltransferases (HATs) and histone deacetylases (HDACs) (Rye et al., 2011). HATs acetylate lysine residues using acetyl-CoA as cofactor and generate coenzyme A (CoA) as coproduct (Rye et al., 2011). The negative charge of the acetyl moiety neutralizes the positive charge on lysine, destabilizing the histone – DNA electrostatic interaction, and increasing accessibility of the DNA (Grunstein, 1997). Based on their most common subcellular localization, HATs are classified in nuclear (type-A) and cytoplasmic (type-B) (Bannister & Kouzarides, 2011; Sun et al., 2015). Type-A HATs acetylate nucleosomal histones and type-B HATs acetylate newly synthesized histones located in the cytoplasm (Bannister & Kouzarides, 2011; Sun et al., 2015). Contrary to the function of HATs, HDACs remove the acetyl-moiety from the lysine residues strengthening the histone-DNA interaction and restoring chromatin compaction (Grunstein, 1997). Based on their cofactor dependency, HDACs are classified in Zn^{2+}-dependent HDACs and NAD^{+}-

dependent HDACs that are also known as sirtuins (Ali et al., 2018) (Shvedunova & Akhtar, 2022).

Multiple lysine residues (>40) are known to be acetylated within the lysine-rich histones (Table 1) (Ali et al., 2018; Shvedunova & Akhtar, 2022) . However, some of these lysines are commonly acetylated in different cell types and organisms. They are considered to be evolutionarily conserved (Kurdistani et al., 2004). These conserved acetylated sites are more common in histone H3 and H4 and include H3K27ac and H4K5ac as some of their best-known examples (Kurdistani et al., 2004). H3K27ac is highly enriched in promoter and enhancer regions (Hnisz et al., 2013). In fact, H3K27ac is considered the marker of active enhancers as these regulatory regions are characterized by having increased H3K27ac (Creyghton et al., 2010; Rada-Iglesias et al., 2011).

Table 1. Representative acetylated lysine residues within histones

HISTONE	LYSINE MODIFICATION	
	Tail Domain	**Globular Domain**
H2A	K5, K9, K13, K15	K36, K118
H2B	K5, K11, K12, K15, K16, K23, K24	K46, K57, K120
H3	K4, K9, K14, K18, K23, K27	K36, K37, K56, K64, K79, K112, K115
H4	K5, K8, K12, K16, K20, K31	K77, K79, K91
H1	*K16, K33	K45, K63, K74, K89, K96, K105, K167

Table obtained from Ali *et al.* (Ali et al., 2018).

The interplay between histone acetylation/deacetylation is critical for cellular homeostasis, as perturbation of this balance has been considered critical for the onset of diseases such as cancer or neurodegeneration (Di Gennaro et al., 2004; Park & Kim, 2020). The dynamic regulation of histone acetylation and deacetylation levels depends, in part, on the abundance of HATs' and HDACs' cofactor's (Dai et al., 2020; Reid et al., 2017). For instance, the cofactor of HATs (acetyl-CoA) is a metabolite synthesized and used by multiple metabolic pathways (Li et al., 2018). Thus, the available acetyl-CoA that HATs can use also depends on complex metabolic networks. In addition, as most HATs have a low affinity (high K_D) for acetyl-CoA, the cellular fluctuations of this metabolite directly impact their catalytic activity and, thereby, histone acetylation levels (Dai et al., 2020). Another consequence of this fluctuation is the fast turnover rate that characterizes histone acetylation compared to other PTMs (e.g., histone methylation) (Dai et al., 2020).

As pointed out, histone acetylation is a posttranslational modification that integrates metabolic and chromatin regulation. Due to its fast turnover rate, histone acetylation allows the development of adaptative chromatin responses that enhance cellular plasticity. Although this modification has been heavily studied in the chromatin landscape, and its canonical functions are described in multiple biological scenarios, understanding how it is co-regulated with metabolism has led to the discovery of new regulatory networks and the update of previously known ones.

2.2 Chromatin and metabolism

Metabolism provides the biochemical plasticity that enables organisms to adapt to the ever-changing intracellular and extracellular environment (Reid et al., 2017; Vander Heiden et al., 2009). Metabolic pathways are composed of interconnected enzymatic reactions that circulate intracellular and extracellular metabolites, processing them through a complex network of biochemical reactions that synthesize new metabolic intermediates that cover specific cellular needs (Buescher et al., 2015; Jang et al., 2018; Tanner et al., 2018).

Central carbon metabolism (CCM) is composed of three of the most evolutionary conserved metabolic pathways: glycolysis, the tricarboxylic acid cycle (TCA cycle), and the hexosamine or pentose phosphate pathway (PPP) (Noor et al., 2010). CCM largely relies on carbohydrate metabolism, and glucose is considered its primary carbon source (Wu et al., 2023). However, decades of research have unveiled the importance of fatty acids (FAs) and amino acids as alternative CCM's carbon suppliers that can dampen metabolic transitions or contribute to maintain homeostatic states (Johnson & Alric, 2013; Sudarsan et al., 2014).

CCM is highly versatile, meaning that the activity of its pathways can be accelerated or reduced depending on context-specific cellular requirements (Noor et al., 2010). Through this metabolic rewiring, the energetic resources produced by one pathway (e.g., glycolysis) can change in abundance or be relocated to alternative routes that are fine-tuned towards the most necessary metabolic pathways (Alam et al., 2023).

The intricate network of CCM and its branching pathways generate the cofactors that chromatin-modifying enzymes use to regulate critical histone PTMs (Figure 2) (Lu & Thompson, 2012). For instance, the glycolytic-TCA cycle axis supplies a fraction of the acetyl-CoA pool used by HATs to acetylate histones (Cai et al., 2011; Evertts et al., 2013). Meanwhile, the crosstalk between one-carbon metabolism and methionine metabolism generates S-adenosylmethionine (SAM), the universal methyl donor used by histone methyltransferases (HMTs) to methylate histones (Locasale, 2013). Hence, the tight interaction between CCM-derived metabolites and histone modification enzymes set the stage for the communication of changes at CCM level into histone PTMs and gene expression programs.

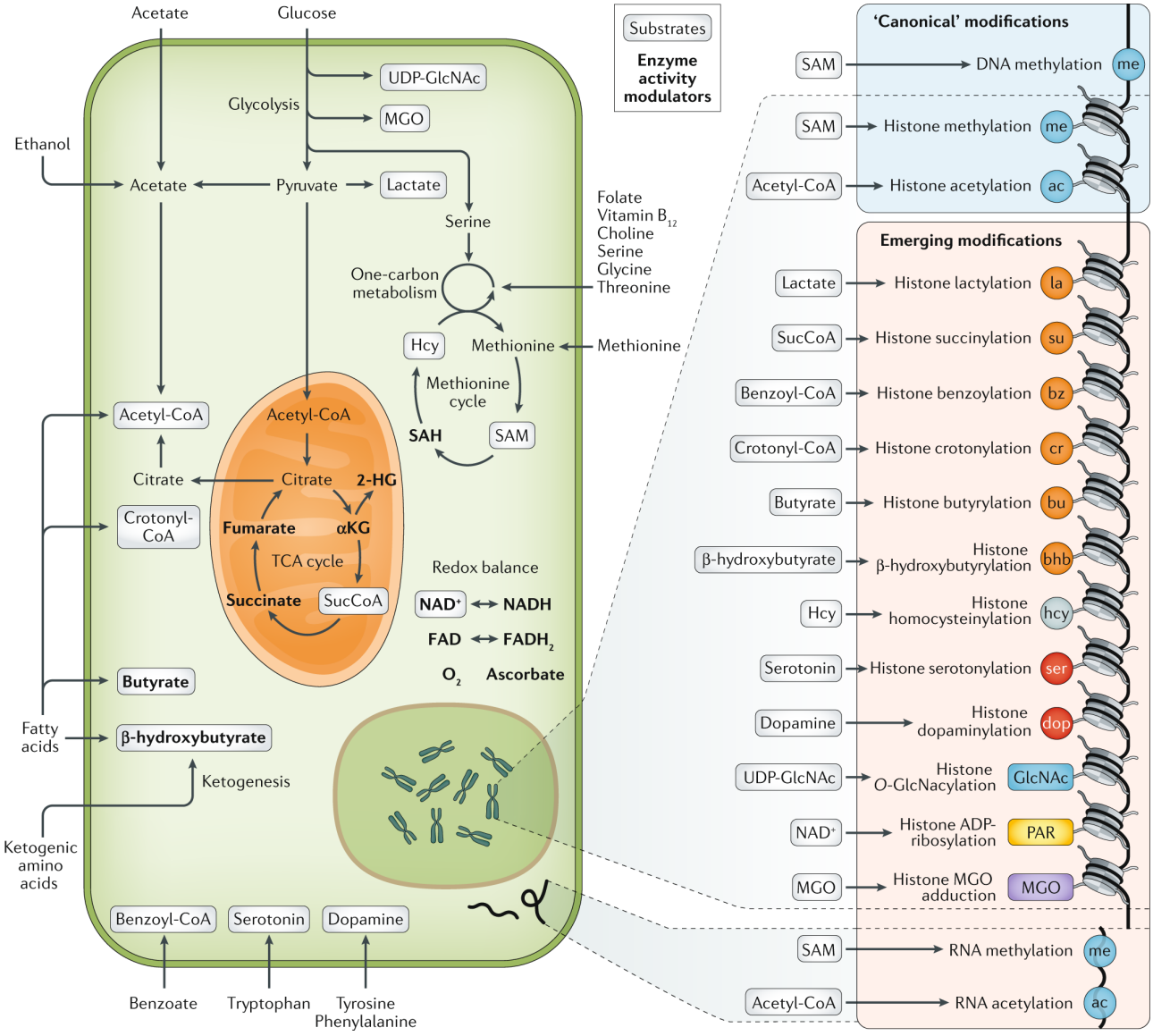

Figure 2. CCM and derived metabolites used as cofactors for histone PTMs

Schematic depicting diverse nutrient sources used by CCM pathways to produce metabolites that are subsequently used as cofactors by chromatin-modifying enzymes to establish histone PTMs, Figure obtained from Dai *et al.* (Dai et al., 2020).

A key feature of this metabolic-chromatin interaction is its interdependence, as gene expression programs also regulate CCM's activities through the transcriptional regulation of its multiple enzymes (Desvergne et al., 2006; Huether et al., 2014; Li et al., 2018; Lu et al., 2012). For instance, several studies have shown the activation of glycolytic gene expression programs that modify metabolic phenotypes in response to, for instance, environmental changes (Desvergne et al., 2006). Whether metabolism or chromatin steers the metabolic-chromatin axis is context- and cell-type-dependent, and under constant change (Pouikli et al., 2021; Pouikli & Tessarz, 2021). As alterations in the metabolic-chromatin crosstalk have shown to be involved in a broad range of physiological processes such as tumorigenesis or the immune response, studying this interaction represents a highly active research field (Lee et al., 2014; Peng et al., 2016).

2.3 Hypoxia cellular response

Oxygen delivery and consumption are fundamental to sustaining multicellular life at the organismal and cellular level (Melvin & Rocha, 2012; Zenewicz, 2017). Although oxygen is vital for a myriad of biochemical pathways, organs, tissues, and cell types are generally exposed to a broad range of oxygen concentrations (Carreau et al., 2011; McKeown, 2014). In mammalian tissues, oxygen concentration ranges from 0% to 19% (Zenewicz, 2017). Within these concentrations, tissues have their specific oxygen sub-range to function appropriately (Carreau et al., 2011). For instance, while the intestinal lumen presents oxygen concentrations close to zero in a healthy state (Albenberg et al., 2014; Wagner et al., 2011), upper airway tissues can present levels of ~19% O_2 under similar physiological conditions (Carreau et al., 2011). Even the same cell type can be exposed to a dynamic range of functional oxygen concentration (McKeown, 2014), as for immune cells that migrate from their low-oxygen bone marrow niche to circulate through the persistently oxygenated blood system (Collins et al., 2015; Luster et al., 2005) or during cellular growth in which oxygen consumption can have a threefold increase compared to lag phase cells (Wagner et al., 2011).

Hypoxia represents the oxygen-depleted condition developed when cells are exposed to oxygen levels below their functional range (Kaluz et al., 2008). This term contrasts with the atmospheric oxygen levels (~21% O_2) that comprises "normoxia," the term that represents the most common culture condition in *in vitro* tissue culture (McKeown, 2014). As tissues and cell types have diverse functional oxygen concentrations, hypoxia is cell-type dependent (Place et al., 2017). For most cell types, research has identified the hypoxia response in cells exposed to 0.5% to 5% O_2, so culture conditions within this range are considered to portray a hypoxic environment (McKeown, 2014).

The molecular response to hypoxia is largely characterized by activation of the oxygen-sensing transcription factor family named Hypoxia-Inducible Factors (HIFs) (Batie et al., 2019). HIFs activate a transcriptional program that elicits a metabolic rewiring required for cell survival under hypoxic conditions (Dengler et al., 2014). HIFs constitute a heterodimeric complex consisting of HIF1α, an oxygen-labile subunit, and HIF1β, its oxygen-insensitive counterpart (Melvin & Rocha, 2012). In normal oxygen conditions, HIF1α and HIF1β are located and regulated separately. The HIF1α subunit is located in the cytoplasm, showing a short half-life due to continuous proteasomal degradation (Jewell et al., 2001; Weidemann & Johnson, 2008). HIF1α is targeted for degradation through prolyl hydroxylation marks catalyzed by a specific class of dioxygenases known as prolyl-hydroxylases (PHDs) (Batie et al., 2019). These hydroxylation marks are then recognized by the E3 ubiquitin ligase complex named tumor suppressor von Hippel Lindau (pVHL) that ubiquitinates HIF1α, targeting it for degradation (Vanderhaeghen et al., 2020). HIF1β is located in the nucleus and has a longer half-life (Weidemann & Johnson, 2008). When oxygen levels drop, HIF1α is no longer hydroxylated and stabilized as consequence (Kaelin & Ratcliffe, 2008). The stabilized HIF1α translocates to the nucleus, dimerizing with HIF1β to form a functional transcription factor complex named HIF (Kaluz et al., 2008; Liu et al., 2008). HIF then binds to consensus DNA sequences collectively known as hypoxia-responsive elements (HREs) that generally occur in promoter or enhancer regions (Wenger et al., 2005). In addition, HIF enhances the transcription of its target genes by recruiting p300/CBP, a HAT that functions as a transcriptional coactivator (Kaluz et al., 2008; Liu et al., 2008).

HIF targets a broad range of genes (>70) that contribute to the cellular adaptation to hypoxia (Weidemann & Johnson, 2008; Wenger et al., 2005). These HIF-regulated genes enhance oxygen supply (e.g., transferrin, VEGF), glucose metabolism (e.g., GLUT, HK, PFK), cell

growth (e.g., *IGFBP-1, CTGF)*, and pro-apoptotic signaling (*NIP3, BNIP3, Noxa)*, among other mechanisms (Kaluz et al., 2008; Kim et al., 2006; Wenger et al., 2005). The HIF-regulated transcriptional program varies between tissues and cell types (Lombardi et al., 2022). Hence, the molecular response to hypoxia is adjusted to the cellular background, allowing metabolic adaptation towards a less oxygen-dependent phenotype that promotes cell survival and diminishes the energetic impact of decreased oxygen supply (Dengler et al., 2014; Kaluz et al., 2008).

Hypoxia generates a metabolic rewiring characterized by higher glucose consumption and glycolytic rates that upregulate lactate production (Figure 3) (Eales et al., 2016). Glycolytic pyruvate redirection from mitochondrial oxidation towards lactate synthesis reduces TCA cycle activity and oxidative phosphorylation (OXPHOS) (Vander Heiden et al., 2009). This reduction in OXPHOS activity drastically decreases ATP synthesis from 36 mol ATP/mol glucose (OXPHOS) to 2 mol ATP/mol glucose (glycolysis) (Schiliro & Firestein, 2021). The hypoxia-mediated metabolic rewiring also increases lactate excretion to the extracellular space, as intracellular lactate accumulation inhibits glycolysis (Eales et al., 2016; Li et al., 2022). Another feature of hypoxic metabolism is the reprogramming of glutamine metabolism from oxidation towards reductive carboxylation in the TCA cycle (Sun & Denko, 2014).

Interestingly, the main features associated with metabolic reprogramming in hypoxia have been identified and extensively studied in cancer cells grown in the presence of oxygen. Known as the “Warburg effect,” this metabolic rewiring has been considered one of the canonical alterations of tumorigenesis since its discovery in 1923 (Eales et al., 2016; Kocianova et al., 2022; Vaupel & Multhoff, 2021). Decades of research have unveiled the diversity in the hypoxia response and the “Warburg effect” and how they can deviate from their canonical models (Vaupel & Multhoff, 2021). Most corrections in this respect point towards maintaining undamaged and functional mitochondria even though glycolysis is enhanced in, for instance, most cancer cells (Vaupel & Multhoff, 2021). The hypoxic and Warburg’s hypoxic-like metabolic phenotypes are essential in a myriad of cellular processes such as embryonic development and proliferation, tissue regeneration, or erythrocyte maturation, thus highlighting the role of metabolic reprogramming as a critical driver of upscale cellular processes and its importance for adaptation. (Kaluz et al., 2008).

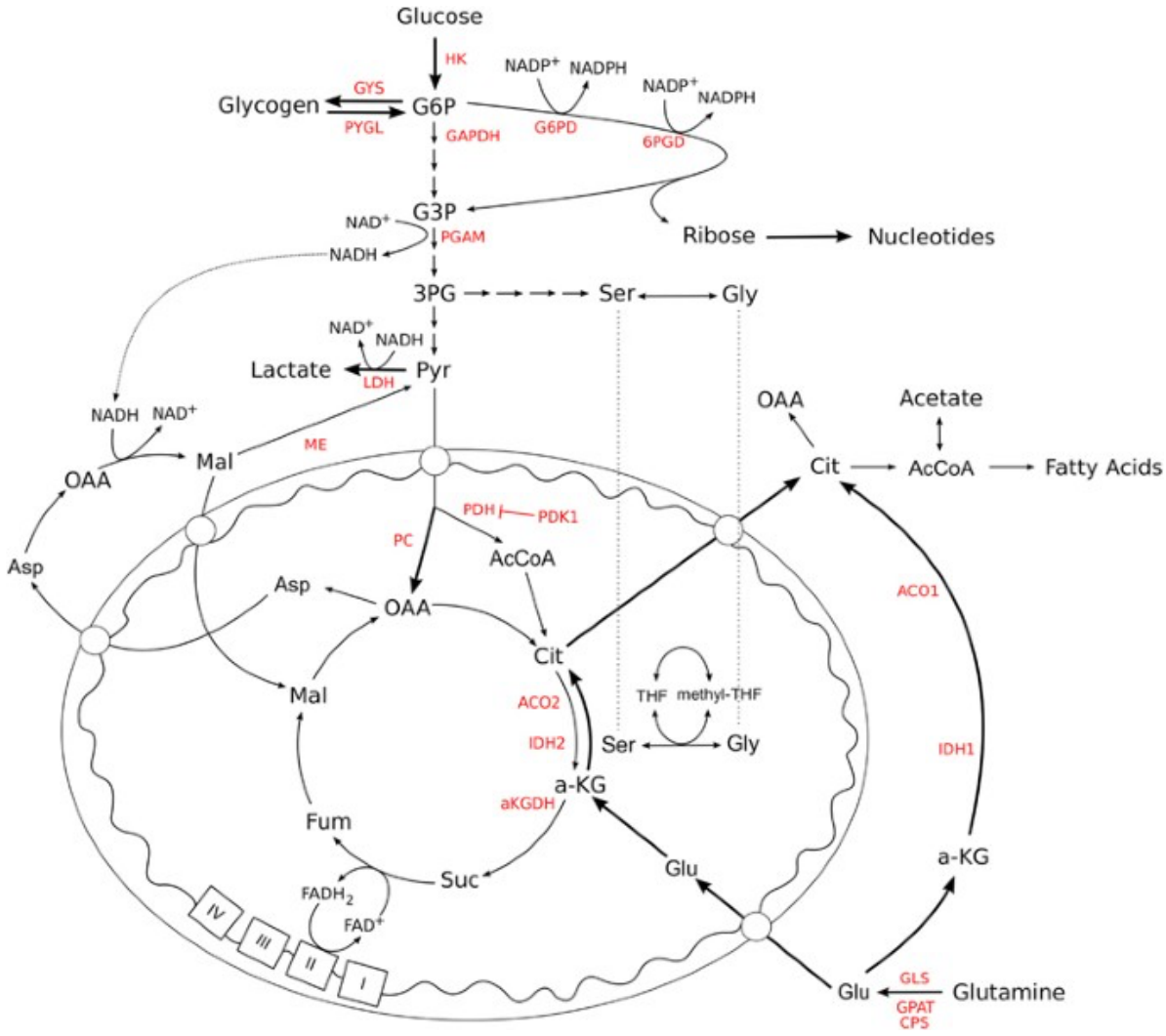

Figure 3. Hypoxic metabolic rewiring as revealed by flux measurements

Schematic representation of CCM's pathways activity obtained from glucose-derived flux measurements. Pathways with higher activity are represented with bold lines. Representative enzymes are colored red. Figure obtained from Eales *et al.* (Eales et al., 2016)

2.4 Mitochondrial pyruvate metabolism

During normoxia, the pyruvate dehydrogenase complex (PDC) converts glycolytic pyruvate into acetyl-CoA in mitochondria (Byron & Lindsay, 2017; Patel et al., 2014; Saunier et al., 2016). This reaction allows the critical metabolic transition that links glycolysis to the TCA cycle (Gray et al., 2014; Stacpoole, 2017). The generated mitochondrial acetyl-CoA conjugates with oxaloacetate, producing citrate (Patel et al., 2014; Pietrocola et al., 2015). Citrate can then be metabolized in the TCA cycle or exported to the cytoplasm, where it can reconvert to acetyl-CoA (Pietrocola et al., 2015; Sivanand et al., 2018). Cytoplasmic acetyl-

CoA can then be used for protein acetylation (histone and non-histone proteins) or *de novo* FA synthesis (Pietrocola et al., 2015; Sivanand et al., 2018).

PDC is a multimeric complex located in the inner mitochondrial membrane (DeBrosse & Kerr, 2016; Forsberg et al., 2020; Reed, 2001; Škerlová et al., 2021). It is constituted by a core of three enzymatic subunits, two regulatory enzymes and a scaffolding protein (DeBrosse & Kerr, 2016; Forsberg et al., 2020; Reed, 2001; Škerlová et al., 2021). PDC requires five coenzymes: thiamine pyrophosphate (TPP), lipoic acid (LA), coenzyme A (CoA), flavin adenine dinucleotide (FAD) and nicotinamide adenine dinucleotide (NAD^+) (Kishnani & Chen, 2013). The association of multiple copies of the enzymatic core allows for the formation of a large-size (~6000 kDa) complex (Kishnani & Chen, 2013; Škerlová et al., 2021; Sumegi et al., 1987). The enzymatic core of PDC consists of pyruvate dehydrogenase (E1), dihydrolipoamide S-acetyltransferase (E2), and dihydrolipoamide dehydrogenase (E3) (Forsberg et al., 2020; Reed, 2001). A scaffolding protein named E3-binding protein (E3BP) recruits E3 to PDC's catalytic core (Forsberg et al., 2020; Reed, 2001). The E1-E3 subunits decarboxylate pyruvate sequentially, forming acetyl-CoA, CO_2, and NADH (Patel et al., 2014). PDC activity is regulated through competitive end product inhibition (acetyl-CoA and $NADH^+ + H^+$) and reversible phosphorylation (DeBrosse & Kerr, 2016; Kantor et al., 2001; Randle & Denton, 1976; Saunier et al., 2016). Pyruvate dehydrogenase kinases (PDHK1-4) inactivate the E1 subunit through phosphorylation of up to three serine residues (Ser^{232}, Ser^{293}, Ser^{300}) (Kantor et al., 2001; Rardin et al., 2009). In contrast, pyruvate dehydrogenase phosphatases (PDP1-2) dephosphorylate E1 and restore its function (Saunier et al., 2016).

The pyruvate dehydrogenase kinase family comprises four mitochondrial isoforms (PDHK1-4) (Green et al., 2008; Kuntz & Harris, 2018; Milne, 2013; Rowles et al., 1996). Although these isoforms are highly conserved, their regulation, tissue expression, and kinetics (e.g., phosphorylation rate and specificity) vary (Kuntz & Harris, 2018; Milne, 2013). Despite these differences, the four isoforms are commonly activated by the end product of PDC (e.g., acetyl-CoA and NADH) and inactivated by PDC's substrate and coenzymes (e.g., pyruvate, NAD+, and CoA) (Green et al., 2008; Kuntz & Harris, 2018). PDHKs can function as homodimers or heterodimers, as different isoforms can be co-expressed within a tissue (Kuntz & Harris, 2018; Milne, 2013).

PDHK1 is a downstream target of HIF that is upregulated in hypoxia (Figure 3) (Atas et al., 2020). PDC inhibition by PDHK1 leads to a decrease in mitochondrial acetyl-CoA synthesis that can subsequently diminish TCA cycle activity or cytoplasmic downstream mechanism (e.g., protein acetylation and lipogenesis) (Gray et al., 2014). In addition, as pyruvate gets diverted from mitochondria, it becomes available for other cytoplasmic reactions, such as lactate synthesis (Koltai et al., 2020; Milne, 2013; Vander Heiden et al., 2009). Thus, PDHK1 function contributes to the high glycolytic rates that characterize the cellular response to hypoxia (Chatterjee et al., 2019).

2.5 Acetyl-CoA metabolism

Acetyl-CoA is a central metabolite synthesized from glucose, FAs, and amino acid metabolism (Shi & Tu, 2015; Zhao et al., 2016). Glucose represents the major carbon source for acetyl-CoA in mammals. However, FAs and amino acids are alternative sources that can compensate for a decrease in glucose-derived acetyl-CoA metabolism. Acetyl-CoA is synthesized in multiple subcellular compartments (Figure 4) (Pietrocola et al., 2015; Sivanand et al., 2018). The canonical and extensively studied routes occur in the mitochondria and cytosol (Kuna et al.; Zhao et al., 2016). However, recent findings have identified acetyl-CoA synthesis in the nucleus and peroxisomal compartments (Sutendra et al., 2014).

Acetyl-CoA is a hydrophobic molecule relatively impermeable to lipid membranes due to the thioester bond that links the acetyl moiety to CoA (Guertin & Wellen, 2023; Shi & Tu, 2015). Based on this physicochemical restriction, acetyl-CoA requires import/export shuttle systems to cross most single-membrane and double-membrane organelles (Wang et al., 2023). For instance, this transport system occurs in the mitochondria and peroxisome but not in the nucleus, as nuclear pores allow nuclear-cytosolic acetyl-CoA diffusion (Pietrocola et al., 2015; van Roermund et al., 1995). In the mitochondrial shuttle system, acetyl-CoA is exported in the form of citrate and then, reconverted to acetyl-CoA in the cytosol (Hynes & Murray, 2010). On the contrary, acetyl-CoA is imported in the form of acetyl carnitine and then, reconverted to acetyl-CoA in mitochondria (Lundsgaard et al., 2018; Wang et al., 2023). This spatial compartmentalization contributes to the forming of two major acetyl-CoA functional pools located in mitochondria and the nuclear-cytosolic space (Pietrocola et al., 2015; Sivanand et al., 2018).

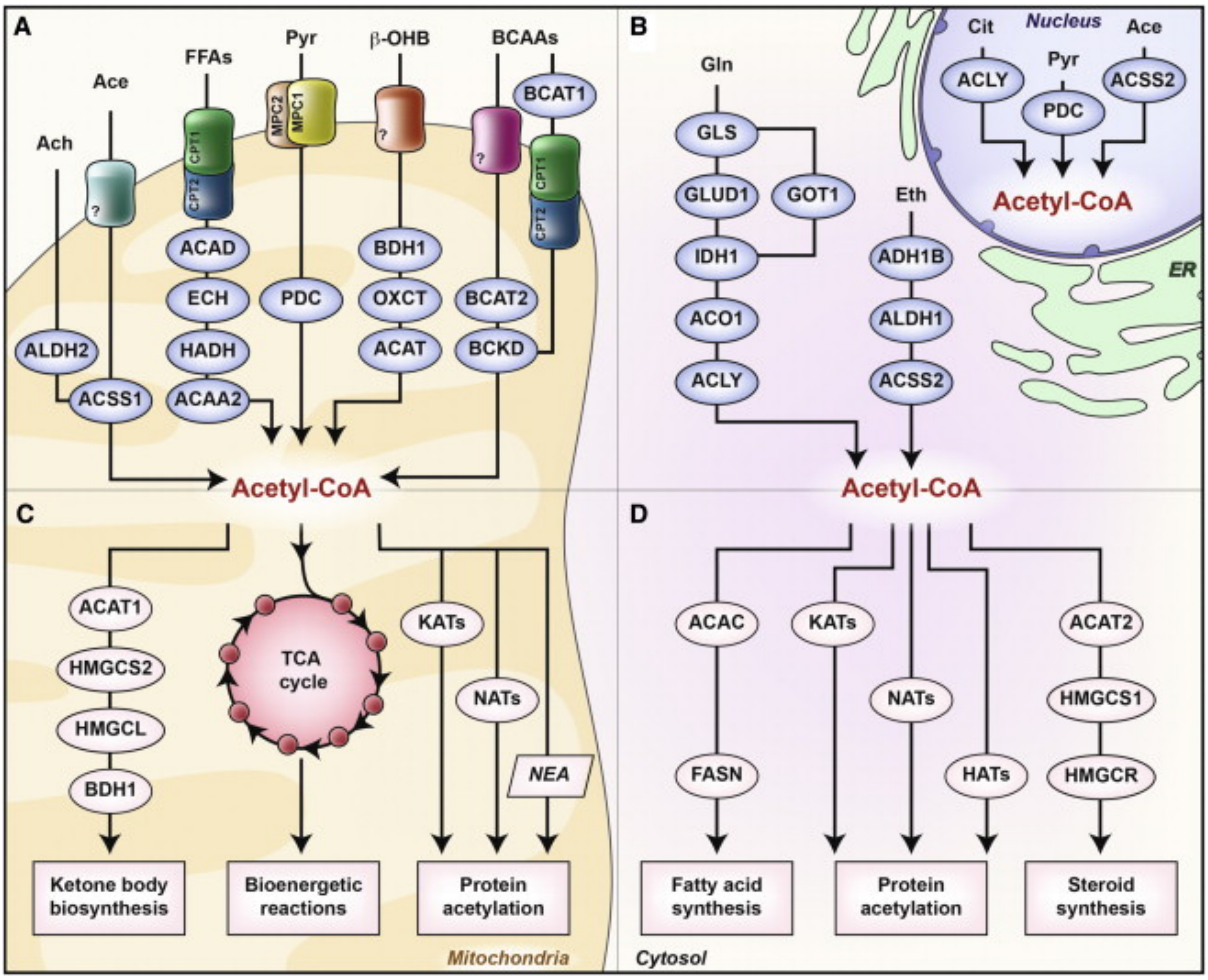

Figure 4. Acetyl-CoA metabolism in different subcellular compartments.

Schematic representation of acetyl-CoA metabolism. Precursor metabolites and their associated enzymes are showed for the **(A)** mitochondrial, and **(B)** nuclear-cytosolic compartments. Pathways and enzymes that use acetyl-CoA in **(C)** mitochondria and the **(D)** nuclear-cytosolic compartments are also depicted. Figure obtained from Pietrocola *et al.* (Pietrocola et al., 2015).

2.5.1 Mitochondrial acetyl-CoA metabolism

Mitochondrial acetyl-CoA metabolism is considered the major source of acetyl-CoA in mammals (Pietrocola et al., 2015). Within this organelle, acetyl-CoA metabolism is highly flexible, as it can process chemically diverse substrates through a plethora of metabolic pathways to generate acetyl-CoA (Figure 4) (Sivanand et al., 2018). The most common sources are glucose-derived pyruvate decarboxylation, FA β-oxidation, and branched-chain amino acid (e.g., valine, leucine and isoleucine) metabolism (Zhao et al., 2016). The activity of these pathways and contribution towards the mitochondrial acetyl-CoA pool fluctuates and adapts to the cellular microenvironment to match the bioenergetic requirements. For instance, during normoxia, acetyl-CoA's most active sources consist of the glucose-derived

pyruvate decarboxylation and FA β-oxidation pathways (Pietrocola et al., 2015). However, in hypoxic conditions, the contribution of glucose-derived pyruvate towards acetyl-CoA synthesis decreases generating a metabolic shift.

Mitochondrial acetyl-CoA serves as substrate of multiple metabolic pathways (Pietrocola et al., 2015; Sivanand et al., 2018). As mentioned previously, mitochondrial acetyl-CoA condenses with oxaloacetate forming citrate (Gerlt, 1999; Van der Kamp, 2013). Citrate can then fuel the TCA cycle or be exported to the cytosol through the tricarboxylate transport protein (SLC25A1) (Tan et al., 2020). In addition, mitochondrial acetyl-CoA can be used for mitochondrial protein acetylation or ketone bodies synthesis (Calder, 2016; Pietrocola et al., 2015). The interplay between these catabolic and anabolic pathways largely determines acetyl-CoA availability within this organelle. Moreover, since mitochondria are a major source of the total acetyl-CoA pool, fluctuations or changes in mitochondrial acetyl-CoA regulation can impact cellular homeostasis and physiological regulation.

2.5.2 Nuclear-cytosolic acetyl-CoA metabolism

The nuclear-cytosolic pool of acetyl-CoA derives from diverse pathways partially separated in the cytosolic and nuclear compartments (Figure 4) (Pietrocola et al., 2015; Sivanand et al., 2018). The most known cytosolic pathways consist of the ATP-citrate lyase (ACLY) and acetyl-CoA synthetase short-chain family member 2 (ACSS2), which uses citrate and acetate as substrates, respectively (Kuna et al.; Zhao et al., 2016) Upon export from mitochondria, ACLY converts citrate and CoA into acetyl-CoA and oxaloacetate (Zaidi et al., 2012). ACSS2 catalyzes the conversion of free acetate to acetyl-CoA using ATP and generating AMP as a coproduct (Ling et al., 2022).

Citrate to acetyl-CoA conversion by ACLY is considered the major pathway for acetyl-CoA synthesis in mammals, particularly as intracellular acetate abundance and ACSS2 activity are usually low and considered to increase only during stress conditions (Liu et al., 2018; Zhao et al., 2016). For instance, it has been shown that the absence of ACLY elicits extracellular acetate consumption and ACSS2 upregulation to support acetyl-CoA synthesis (Zhao et al., 2016). This metabolic shift compensated for the loss of ACLY-derived acetyl-CoA and contributed to cell survival and proliferation (Zhao et al., 2016). Thus, the interplay of these cytosolic pathways is critical for cellular homeostasis. However, the downstream

mechanisms generated by individual ACLY- or ACSS2-derived acetyl-CoA can also lead to different cellular outcomes (Wellen et al., 2009). A cell culture model of ACLY downregulation showed decreased global histone acetylation levels with no changes in total protein acetylation (Wellen et al., 2009). Meanwhile, ACSS2 downregulation showed no effect in either histone or non-histone protein acetylation (Wellen et al., 2009). Hence, even though these canonical pathways generate acetyl-CoA, their activity and relative contribution towards the nuclear-cytosolic acetyl-CoA pool can affect differently other regulatory networks, such as chromatin and gene expression.

In the cytosol, acetyl-CoA is the substrate of a dynamic set of pathways that regulate protein acetylation, FAs, and steroid synthesis (also known as the mevalonate pathway) (Sivanand et al., 2018). The biochemical background of protein acetylation (non-histone proteins and histones) is highly similar and was described previously. FAs and steroids are molecules with high energetic storage capacity compared to carbohydrates or proteins (Kloska et al., 2020). Hence, cytosolic acetyl-CoA is an important facilitator of energy-rich storage and a key indicator of the energetic status of the cell when converted to FAs or steroids. These high-energy storage molecules expand the cell's metabolic flexibility and homeostatic capacity since contexts of limited resources activate their catabolism to compensate for energy loss.

De novo FA synthesis or lipogenesis initiates with the conversion of acetyl-CoA to malonyl-CoA by acetyl-CoA carboxylases (ACCs) (Figure 5) (Batchuluun et al., 2022; Brownsey et al., 2006). The association of seven malonyl-CoA molecules and one acetyl-CoA is then used by the fatty acid synthase (FASN) to generate palmitate (16:0), one of the most common long-chain FAs in mammals (Batchuluun et al., 2022; Kerner et al., 2014). Although lipogenesis is a complex process regulated by different enzymatic circuitries such as ACCs and FASN, the rate-limiting step is catalyzed by the ACCs (Pietrocola et al., 2015).

ACCs consist of the biotin-dependent isoforms ACC1 (cytosolic localization) and ACC2 (outer mitochondrial membrane localization), that function as homodimers regulated by phosphorylation (Brownsey et al., 2006; Wang et al., 2022). When the energetic status of the cell decreases, as in contexts characterized by elevated AMP:ATP ratios, ACCs are phosphorylated (ACC1-Ser^{79} and ACC2-Ser^{212}) by the AMP-activated protein kinase (AMPK) (Galic et al., 2018). ACCs phosphorylation (P-ACC1/2) decreases FAs elongation, which increases lipolysis and β-oxidation (potentially increasing mitochondrial acetyl-CoA) and the

abundance of cytosolic acetyl-CoA (Chow et al., 2014; Galdieri & Vancura, 2012; McDonnell et al., 2016). Thus, P-ACC1/2 can severely impact levels of protein acetylation. How specific does P-ACC1/2 affect this PTM? Recent findings using a yeast model to analyze histone acetylation upon ACC1 downregulation reported global histone hyperacetylation (Galdieri & Vancura, 2012). The association of ACC1 downregulation and histone hyperacetylation also demonstrated that FAs and HATs utilize the same acetyl-CoA pool (Galdieri & Vancura, 2012). In contrast to these findings, mouse hepatocytes carrying a liver-specific double knockout (ACC1$^{-/-}$/ACC2$^{-/-}$) showed a differential effect on the acetylation of mitochondrial and nonmitochondrial proteins (Chow et al., 2014). While mitochondrial proteins were hypoacetylated, nonmitochondrial proteins were hyperacetylated. Although with different outcomes, these studies confirm (in different biological models) the recently discovered coordination of lipid metabolism and protein/histone acetylation. These findings also demonstrate the dynamic regulation (e.g., subcellular compartments) of this scarcely known system, opening the door to the discovery of new regulators and regulatory pathways.

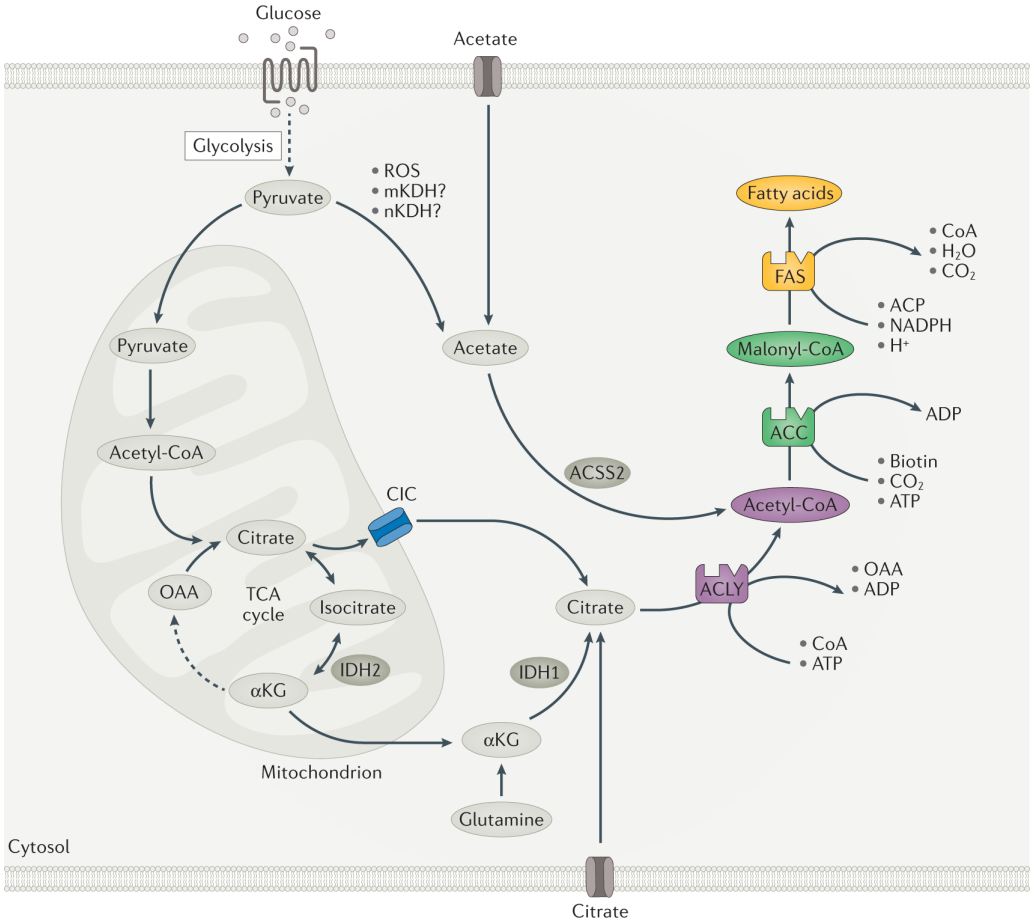

Figure 5. Metabolic pathways involved in *de novo* fatty acid synthesis

Schematic representation of *de novo* FA synthesis or lipogenesis. Depicted in bright colors are the initial steps of lipogenesis, that starts with the conversion of acetyl-CoA to malonyl-CoA, and continues to generate fatty acids of different lengths. Figure obtained from Batchuluun *et al.,* (Batchuluun et al., 2022).

2.5.3 Nuclear acetyl-CoA metabolism

Recent studies have detected acetyl-CoA synthetases in the nuclei that were initially considered purely cytosolic or mitochondrial (Sutendra et al., 2014; Wellen et al., 2009). The detection of a nuclear ACLY showed the possibility that citrate could be converted to acetyl-CoA within the nuclei, which could be used directly by HATs to acetylate core histones (Wellen et al., 2009). A functional PDC was also identified in this organelle in response to diverse extracellular and intracellular stressors (Sutendra et al., 2014). PDC's inhibitor (PDHK1) did not colocalize in this organelle. Thus, pyruvate can generate acetyl-CoA directly in the nuclei but is deprived of PDC's regulator (Sutendra et al., 2014). In cellular contexts with high glycolytic rates and, thereby, high pyruvate production, which functional outcome does a nuclear PDC have? The underlying mechanisms of this finding (e.g., intracellular translocation) are not understood but will expand our knowledge of the noncanonical pathways of the critical metabolite acetyl-CoA.

2.6 Metabolomics

The interplay between metabolism and chromatin regulation has been unraveled as a critical component of healthy and diseased cellular states (Etchegaray & Mostoslavsky, 2016; Nativio et al., 2020; Wong et al., 2017). The emergence and constant improvement of high-throughput "omics" technologies have been fundamental to demonstrate the importance of this association (Blankenburg et al., 2009; Tebani et al., 2016). The combination of chromatography (e.g., HPLC, LC, GC) with mass-spectrometry (MS) techniques has provided the analytical tools required by "omics" technologies to study chemically diverse samples by separating complex mixtures into individual molecules that are subsequently identified and quantified (Alseekh et al., 2021; Coskun, 2016; Zaikin & Borisov, 2021) . Based on this technological foundation, metabolomics and proteomics analysis have enabled the identification of thousands of molecules and the characterization of multiple cellular phenotypes (Alseekh et al., 2021). Next-generation sequencing (NGS) and chromatin-profiling methods (e.g., ChIP-seq, ATAC-seq, CUT&RUN) have allowed the characterization of genomes, transcriptomes, and their functional states (Buenrostro et al., 2015; Dai et al., 2020). Despite being sources of comprehensive information that is very difficult to obtain

using smaller-scale techniques, these “omics” technologies impose multiple technical challenges regarding sample preparation, bioinformatics analysis, and datasets integration. Rather than representing an obstacle, acknowledging these limitations contributes to establishing realistic boundaries to the results derived from “omics”-based research.

Characterizing metabolic pathway activity and abundance is essential to determine metabolic phenotypes (Dai & Locasale, 2017; Jang et al., 2018). Metabolic flux analysis is one of the most common techniques for measuring pathway activity (Buescher et al., 2015; Zamboni et al., 2009). This technique heavily relies on the use of tracing experiments that utilize stable isotopes (e.g., C^{13}, H^{2}, N^{15}, O^{18}) as substrates to target a metabolic network of interest (Buescher et al., 2015; Zamboni et al., 2009). Through this strategy, it is possible to calculate the turnover of the labeled substrate within a myriad of biochemical reactions that can be tested in multiple experimental conditions (e.g., nutrients (scarce/abundant), oxygen tension (high/low), differentiation state (pluripotent/differentiate)) (Buescher et al., 2015; Zamboni et al., 2009). On the contrary, to quantitatively determine metabolic abundances or pool sizes, stable isotopes are not required. The combination of these experimental strategies provides a comprehensive overview of the general metabolic state.

3 RESEARCH AIMS

The crosstalk of metabolism and chromatin is essential for cellular homeostasis and adaptation. On the one hand, metabolism provides the cofactors used by chromatin-modifying enzymes to establish diverse histone PTMs. On the other hand, gene expression regulates metabolism by modulating the transcriptional activity of the enzymatic circuitry. Hypoxia is a low oxygen condition developed when cells are exposed to oxygen levels below their functional range (Kaluz et al., 2008). These hypoxic conditions generate a concomitant metabolic and transcriptional response characterized by increasing glucose metabolism and reducing TCA cycle activity.

In mammals, glucose is considered the main source of acetyl-CoA, the intermediate metabolite used by HATs as cofactor for histone acetylation. Although the cellular response to hypoxia has been extensively characterized, recent studies have revealed a more complex metabolic adaptation to these low oxygen conditions. Furthermore, the link between glucose metabolism and histone acetylation has recently emerged as driven by an intricate circuitry of pathways related to acetyl-CoA metabolism. Thus, the mechanistic background that determines the glucose -> acetyl-CoA -> histone acetylation axis remains to be fully understood. Therefore, this thesis project aims to:

1) Characterize the impact of hypoxia on glucose metabolic flux to acetyl-CoA and histone acetylation.
2) Investigate the role of PDHK1 as a central gatekeeper of glucose-to-acetyl-CoA flux on the observed effects under hypoxia.

4 MATERIALS AND METHODS

4.1 Materials

Table 2. Cell culture lines, reagents, growth media, antibiotics

Name	Supplier	Cat. Number
DMEM (-Phenol Red)	Gibco	A14430
DMEM + Glutamax medium	Gibco	61965
Seahorse XF DMEM medium, pH 7.4	Agilent	103575-100
Dulbecco's modified PBS (DPBS)	Gibco	14190
Fetal Bovine Serum (FBS)	Gibco	10500-064
D-Glucose -$^{13}C_6$	Sigma-Aldrich	389374
L-Glutamine - $^{13}C_5$	Sigma-Aldrich	605166
HEK293T cells	ATCC	
Seahorse XF Glucose Solution (1M)	Agilent	103577
Seahorse XF Glutamine Solution (200 mM)	Agilent	103579
MEM Alpha medium + Glutamax (α-MEM)	Gibco	32561-037
NIH-3T3 cells	DSMZ	ACC 59
Opti-MEM Reduced Serum Media	Gibco	31985
Penicillin/Streptomycin (10.000 U/ml)	Gibco	15140-122
Polybrene	Santa Cruz	sc-134220
Puromycin-Dihydrochlorid (10 mg/mL)	Gibco	A11138
QIAzol Lysis Reagent	Qiagen	79306
Sodium Pyruvate (100 mM)	Gibco	11360
TransIT-X2® Dynamic Delivery System	Mirus	MIR6000

Trypan Blue Solution	Sigma-Aldrich	T8154
0.05% Trypsin-EDTA (1x)	Gibco	25300-054

Table 3. Antibodies used for Western Blot and immunofluorescence

Name	Supplier	Cat. Number	Dilution (WB)
ACC1	ProteinTech	21923-1-AP	1:1000
P-ACC1 (Ser79)	Cell Signaling	3661	1:1000
ACLY, pAb	Proteintech	5421-1 AP	1:1000
AceCS1 (D19C6), mAb	Cell Signaling	3658S	1:1000
β--actin- HRP Conjugate, mAb	Cell Signaling	12262S	1:1000
Alexa-Fluor 488	Thermo Fischer	A11001	--
Alexa-Fluor 594	Thermo Fischer	A11012	--
Histone H3 (1B1B2), mAb	Cell Signaling	14269S	1:10,000
Histone H3K27ac, pAb	Active Motif	39133	1:1000
Histone H3K14ac, pAb	Active Motif	39616	1:1000
Histone H3K27me3, pAb	Active Motif	39155	1:1000
Histone H3K9me3, pAb	Active Motif	39161	1:1000
Histone H3K4me3, pAb	Active Motif	39159	1:1000
Histone H3ac (pan-acetyl), pAb	Active Motif	39139	1:1000
Histone H4K16ac, pAb	Active Motif	39168	1:1000
Histone H4K5ac, pAb	Active Motif	39700	1:1000
Histone H4ac, pAb	Sigma-Aldrich	06-866	1:1000
LDHA / LDHC (C28H7), mAb	Cell Signaling	3558S	1:1000
PDHA	Cell Signaling	2784	1:1000
P-PDHA (Ser 293)	Cell Signaling	31866	1:1000
PDHK1 (C47H1), mAb	Cell Signaling	3820S	1:1000
anti-mouse IgG HRP-linked	Cell Signaling	7076S	1:1000

anti-rabbit IgG HRP-linked	Cell Signaling	7074S	1:1000
TOMM20	Sigma Aldrich	WH0009804M1	1:1000
αTubulin	Cell Signaling	2144	1:1000
Vinculin (E1E9V)	Cell Signaling	13901	1:100

4.1.1 Chemicals

Chemicals used in this study were purchased from the companies Sigma-Aldrich (Steinheim, Germany), ROTH (Karlsruhe, Germany), Roche (Mannheim, Germany), Life Technologies (Darmstadt, Germany) and Thermo Scientific (Waltham, USA). Plastic supplies were ordered from Sarstedt (Nümbrecht, Germany), and VWR International (Darmstadt, Germany).

4.1.2 Commercial kits

- Amersham Hyperfilm ECL (Sigma-Aldrich, GE28-9068-37)
- cOmplete EDTA-free Protease Inhibitor Cocktail (Sigma-Aldrich, 11836170001)
- Direct-zol RNA Miniprep Kit (Zymo Research, R2052)
- 100 bp DNA ladder (Thermo Scientific, 15628019)
- ECL Western Blotting Substrate (Promega, W1001)
- FastStart Essential DNA Green Master (Roche, 06402712001)
- GelGreen® Nucleic Acid Gel Stain, 10,000X in Water (Biotium, 41005)
- GoScript Reverse Transcriptase (Promega, A5003)
- GoTaq Hot Start Polymerase (Promega, M5001)
- NucleoSpin DNA RapidLyse kit (Macherey Nagel, 740100)
- Pierce BCA Protein Assay Kit (Thermo Scientific, 23227)
- PureYield Plasmid Maxiprep System (Promega)
- Random Hexamer Primer (Thermo Scientific, SO142)
- RNA ScreenTape (Agilent, 5067-5576)
- RNA ScreenTape Ladder (Agilent, 5067-5578)
- RNA ScreenTape Sample Buffer (Agilent, 5067-5577)
- Seahorse XF Mito Fuel Flex Test Kit (Agilent, 103260-100)
- Seahorse FluxPaks (Agilent, 102416-100)
- SuperSignal West Femto Substrate (Thermo Scientific, 34095)

- Trans-Blot Turbo Transfer Kit Nitrocellulose (Bio-Rad, 1704270)

4.1.3 Electronic equipment

- Balance (Sartorius, Göttingen, Germany)
- Benchtop pH meter (VWR, Darmstadt, Germany)
- Centrifuge Mega Star 1.6R (VWR, Darmstadt, Germany)
- Centrifuge Pico21 and Fresco21 (Thermo Scientific, Waltham, USA)
- DiaMag Rotator (Diagenode, Liege, Belgium)
- Freezer -80°C (VWR, Darmstadt, Germany)
- Freezer -20°C (Liebheer, Bulle, Germany)
- Fridge 4°C (Liebheer, Bulle, Germany)
- Hypoxia incubator (Binder, Tuttlingen, Germany)
- Ice machine (Scotsman, Mailand, Italy)
- Led Illuminator BL star16 (Biometra, Jena, Germany)
- Microwave (Severin, Sundern, Germany)
- Rocking platform (VWR, Darmstadt, Germany)
- Roller 6 basic (IKA, Königswinter, Germany)
- TC automated cell counter (Bio Rad, Munich, Grermany)
- Thermal cycler T100 (Bio Rad, Munich, Grermany)
- Thermomixer basic (CellMedia, Zeitz, Germany)
- Vortex 2 genie (Scientific Industries, New York, USA)
- Water bath VWB18 (VWR, Darmstadt, Germany)

4.1.4 Instruments

- Agilent 2200 TapeStation (Agilent)
- Chemostar PC ECL and Fluorescer Imager (Instas)
- Gel electrophoresis system (Bio Rad, Munich, Germany)
- Light Cycler 96 System (Roche)
- NanoPhotometer N60/N50 (Implen)
- Seahorse XFe96 Extracellular Flux Analyzer (Agilent)
- Trans-Blot Turbo Transfer System (Bio-Rad, 1704150)

4.2 Methods

4.2.1 Experimental models

4.2.1.1 Cell lines

NIH-3T3 (DSMZ) and HEK293T (ATCC) cells were cultured in Dulbecco's modified eagle medium with high glucose (DMEM Glutamax, 4.5 g/L glucose, Gibco) supplemented with 10% fetal bovine serum (Gibco) and 1% Penicillin/Streptomycin (Gibco). Cells were incubated at 37 °C in a humidified 5% CO_2 incubator and were routinely tested for *Mycoplasma spp.* infection. For hypoxia treatments, cells were maintained at 2% O_2 in a hypoxia incubator (Binder) for 24 h, unless otherwise indicated.

NIH-3T3 cells were used as the main experimental model while HEK293T cells were used only for lentiviral transfection. Therefore, NIH-3T3 are referred as "cells", unless otherwise stated.

4.2.2 Cell culture

4.2.2.1 Cell harvesting and passaging

Cells were passaged when confluency reached 80-100%. Culture medium was removed and cells were washed twice with Dulbecco's modified PBS (DPBS, Gibco). Cells were harvested with 0.05% Trypsin-EDTA (Gibco) during 4 min at 37 °C in a humidified 5% CO_2 incubator. Detached cells were resuspended in pre-warmed (37 °C) culture medium and centrifuged at 300 x g for 5 min. The cell pellet was resuspended twice in DPBS and centrifuged at 300 x g for 5 min. After the second resuspension, 10 µL of cell suspension were used to determine total cell number and percent viability using an automated cell counter (Bio-Rad) and Trypan Blue Exclusion (Sigma-Aldrich), respectively. Then, the cell pellet was resuspended in pre-warmed culture medium and 1.5 x10^6 cells were passaged to a new T-175 (Sarstedt) culture vessel containing fresh culture medium.

4.2.2.2 Cell thawing and freezing

Cells were harvested as described in section 3.2.2.1 and resuspended in freezing medium (DMEM Glutamax, 4.5 g/L glucose, supplemented with 10% FBS and 10% DMSO). From 1 to 2 x10^6 cells were transferred to cryogenic storage vials (Sarstedt), stored in a Cell Camper container (Neolab) at -80 °C for 24 h and transferred to a vapor-phase liquid nitrogen container for long-term storage.

For thawing cryopreserved cells, cryovials were removed from the liquid nitrogen storage container and placed directly into a 37 °C water bath until 20% of ice was left in the vial. Thawed cells were transferred to a 15 mL centrifuge tube (Sarstedt) containing pre-warmed (37 °C) culture medium and centrifuged at 1300 rpm for 5 min. The cell pellet was resuspended in pre-warmed (37 °C) culture medium, total cell number and percent viability was performed as described in section 3.2.2.1. Then, cells were transferred to a new T-75 (Sarstedt) culture vessel containing fresh culture medium.

4.2.3 Biochemistry and molecular biology

4.2.3.1 Mycoplasma PCR detection

Genomic DNA was isolated from cell pellets obtained as described in 4.2.2.1 using the NucleoSpin DNA RapidLyse kit (Macherey Nagel). Then, 75 ng of DNA were PCR-amplified using the GoTaq Hot Start Polymerase (Promega) according to manufacturer's instructions. The *Mycoplasma*-genus specific primer set MGSO (van Kuppeveld et al., 1993) (forward, 5' -TGCACCATCTGTCACTCTGTTAACCTC- 3'; reverse, 5'-GGGAGCAAACAGGATTAGATACCCT -3') targeting the 16S rRNA gene was used for detection. PCR products were separated on 1.5% agarose gels pre-mixed with the fluorescent GelGreen DNA stain (Biotium), compared against 100 bp DNA ladder (Thermo Scientific) as a size marker and, detected using a UV transilluminator.

4.2.3.2 RNA isolation

Total RNA was isolated from an 80-90% confluent well of a 6-well plate using the Direct-zol RNA Miniprep kit (Zymo Research) according to manufacturer's instructions. Briefly, culture medium was removed and cells were washed twice with Dulbecco's modified PBS (DPBS, Gibco). Then, cells were lysed in QIAzol (Qiagen) by pipetting, followed by the addition of an equal amount of 99.8% ethanol to the lysate and, transfer into a spin column with a subsequent washing step. Genomic DNA was removed by using an in-column DNase *I* digestion. After several washing steps, the RNA was eluted in Nuclease-free water and quantified using a Nanophotometer (Implen). RNA was either used directly for downstream applications or stored at -80°C.

4.2.3.3 RT-PCR and qRT-PCR

Total RNA was isolated as described in section 4.2.3.2. Then, 200 ng of RNA were retrotranscribed using the GoScript Reverse Transcriptase kit (Promega) and Random Hexamer Primers (Thermo Scientific) according to manufacturer's instructions. Subsequently, 10 ng of complementary DNA (cDNA) were used as template for qRT-PCR using the FastStart Essential DNA Green Master Mix (Roche). All reactions were performed in triplicate using the LightCycler 96 (Roche) detection system.

Fold change in gene expression was calculated with the ΔCq method using β-Actin as housekeeping gene. Primers were designed to span exons using the Primer-Blast designing tool (NCBI). Primer sequences are provided in Table 4.

Table 4. Primer sequences used for qRT-PCR

Gene	Forward Sequence	Reverse Sequence
Pdk1	TCCCCCGATTCAGGTTCAC	CCCGGTCACTCATCTTCACA
Acss2	ACTTGGCGACAAAGTTGCTTTT	ACCCTTCTGAATGCCCTGTTTA
Acly	GCTAAAACCTCGCCTGGGAC	GAACTCCTCCGCCTGACTGT
β-Actin	GCTGTATTCCCCTCCATCGTG	CACGGTTGGCCTTAGGGTTCAG

cDNA synthesis reaction (RT-PCR)

Experimental RNA (200 ng / reaction)	X µL
Random primer (0.5 µg)	2.5 µL
GoScript Reaction Buffer (5x)	4.0 µL
MgCl2 (3 mM)	2.4 µL
PCR nucleotide mix (0.5 mM)	1.0 µL
GoScript Reverse Transcriptase	1.0 µL
adjusted to 20 µL with Nuclease- free water	

cDNA synthesis program

25 °C for 5 min

42 °C for 1h

70 °C for 15 min

hold at 4 °C, cDNA was stored at -20 °C

qRT-PCR reaction

(Reactions were performed in triplicates)

cDNA (10 ng)	1 µL
Primers F + R (10 µM)	1 µL
FastStart Essential DNA Green Master (2x)	5 µL
Nuclease-free water	3 µL

4.2.3.4 RNA sequencing (RNA-seq)

Total RNA was isolated and quantified as described in section 4.2.3.2. RNA quality was assessed using the Agilent 2200 TapeStation System (Agilent) according to manufacturer's instructions. For non-transfected NIH-3T3 cells, RNA library preparation was performed by M.Sc. Jenniffer Maßen and sequencing was carried out at the Cologne Center for Genomics (CCG). For shRNA-PDHK1 NIH-3T3 cells, 2 µg of total RNA were used to perform paired-end RNA sequencing by using the 2x100-bp protocol and three replicates per condition. Library preparation and sequencing were performed at the CCG.

The RNA-seq analysis of NIH-3T3 cells was performed by M.Sc. Jenniffer Maßen.
The RNA-seq analysis of shPDHK1 cells was performed by M.Sc. Ayesha Iqbal from the Bioinformatics Core Facility of the Max Planck Institute for Biology of Ageing.

4.2.3.5 Western Blot

Whole cell protein extract was isolated either from an 80-90% confluent well of a 6-well plate or from cell pellets obtained as described in section 4.2.2.1. Cells were lysed in RIPA buffer containing proteases and histone deacetylases inhibitors, followed by a 30 min incubation at 4 °C. Then, lysates were centrifuged at 21,000 x g for 20 min at 4 °C to remove cell debris. The supernatant containing the whole cell protein extract was collected and used directly for Western Blotting or stored at -20 °C.

Protein concentration was quantified using the BCA Protein Assay Kit (Thermo Scientific). Laemmli Buffer (LB) and DTT (350 mM) were added to the protein extract and samples were heated to 90 °C for 5 min. 15-30 µg of total protein were separated by SDS-PAGE

electrophoresis performed at 130 V for ~1.5 h using 8% (>120 kDa), 12% (<120 kDa) or 15% (<15 kDa) hand-casted gels. Then, proteins were transferred to a nitrocellulose membrane using the Trans-Blot Turbo Transfer System (Bio-Rad) and the manufacturer's pre-programmed protocols. Membranes were incubated in Ponceau S staining for 5-10 min to confirm protein transfer. Subsequently, membranes were incubated in blocking buffer for 1 h at 4 °C, followed by primary antibody incubation performed overnight at 4 °C. After three washing steps with TBST that lasted 5 min each, membranes were incubated with the appropriate horseradish peroxidase (HRP)-conjugated secondary antibody for 2 h at RT. Followed by another round of three washing steps with TBST for 5 min each, chemiluminescence was performed using the ECL Western Blotting Substrate (Promega) or SuperSignal West Femto Substrate (Thermo Scientific) to detect low concentrated proteins. The chemiluminescent signal was detected either by using the Amersham Hyperfilm ECL (Sigma-Aldrich) or the Chemostar PC ECL Imager System (Instas). The antibodies used and their respective dilutions in blocking buffer are listed in Table 3.

RIPA buffer
150 mM NaCl
5 mM EDTA
50 mM Tris (pH 8.0)
1% NP-40
0.5% Sodium deoxycholate
0.1% SDS
1x cOmplete EDTA-free Protease Inhibitor Cocktail (Sigma-Aldrich)

Blocking buffer
5% non-fat dried milk powder
Tris-buffered saline (TBS) with 0.1% Tween-20 (TBS-T)

4.2.3.6 Histone extraction for western blotting

NIH-3T3 cells were seeded at a density of 8 x10^6 cells on a T-175 flask and cultured in normoxia (21% O_2) and hypoxia (2% O_2) for 24 h as described in 4.2.1.1. Then, cells were harvested and pelleted as described in 4.2.2.1. The cell pellet was used directly for histone extraction or stored at -80 °C.

Histones were purified using acid extraction adapted from (Leidecker et al., 2016). Briefly, pelleted cells were lysed in 0.1 M H_2SO_4 for 2 h at 4 °C with gentle rotation. The lysate was centrifuged at 3500 rpm for 20 min at 4 °C. The supernatant was collected and neutralized with 1 M Tris-HCl (pH 8.0) using the same volume of H_2SO_4. Subsequently, histones were precipitated overnight with 4% $HClO_4$ at 4 °C and centrifuged at 21,000 x g for 45 min at 4 °C. The supernatant was carefully removed by pipetting and the histone pellet was washed twice with 4% $HClO_4$. After each washing step of this protocol, pellets were centrifuged at 21,000 x g for 45 min at 4 °C. The histone pellet was washed twice with 0.2% HCl diluted in acetone and twice with 100% acetone. The pellet was dried for 20 min at RT and resuspended in Nuclease- free water supplemented with 1x cOmplete EDTA-Protease Inhibitors (Sigma-Aldrich). Samples were stored at -80 °C until ready for western blotting, performed as described in 3.2.3.6.

4.2.3.7 shRNA knockdown

Mission shRNA bacterial glycerol stock (Sigma-Aldrich) containing the plasmid pLKO.1-Puromycin-PDK1 or a nontargeting shRNA-containing plasmid were propagated on LB plates with ampicillin. The shRNA sequences are provided in Table 5. Plasmids were extracted using the PureYield Plasmid Maxiprep System (Promega) according to manufacturer's instructions. Lentiviral particles were generated by co-transfection of the shRNA-expressing viral vectors with the lentiviral envelope pMD2.G (Addgene) and packaging psPAX2 (Addgene) plasmids into HEK293T cells. Specifically, 1 $x10^6$ cells were plated in 10 cm plates 24 h prior to transfection to be 70% confluent at plasmid delivery. The next day, a transfection complex containing 2x HBS, 2 M $CaCl_2$, 10 µg pLKO.1-Puromycin-PDK1 / nontargeting shRNA-containing plasmid, 5.2 µg pMD2.G and 5.2 µg psPAX2 was incubated for 30 min at RT and subsequently added to the cells. After 17 h, the transfection medium was removed and fresh culture medium prepared as described in 3.2.1.1 was added to the cells. Then, 72 h post-transfection the virus-containing supernatant was collected and cleared of cellular debris after centrifugation at 500 x g for 5 min and 0.45 µm filtration.

For lentiviral vector transduction, NIH-3T3 cells were plated at 1.5 $x10^5$ cells per well of a 6-well plate 24 h before transduction to reach 50% confluency at virus delivery. Next day, cells were transduced with 1mL of virus suspension diluted in 1 mL culture medium with 4 µg/mL

Polybrene (Santa Cruz). After 18 h, transduction medium was replaced with fresh culture medium. Then, 72 h post-transduction cells were subjected to antibiotic selection with 1.2 µg/mL puromycin until all cells of the uninfected control were eliminated.

Table 5. shRNA sequences used for PDK1 knockdown

shRNA	Target sequence	Supplier	Cat. Number
shRNA-PDK1_1	GCGGCTTTGTGATTTGTATTA	Sigma-Aldrich	TRCN0000078811
shRNA-PDK1_2	CGGCTTTGTGATTTGTATTAT	Sigma-Aldrich	TRCN0000078812

4.2.3.8 ACC inhibition

CP-640186 (Sigma-Aldrich), the inhibitor of ACC1 and ACC2, was diluted (20 µM) in water, and added fresh to shRNA cells followed by 48 h incubation. DMSO-treated cells were used as negative control. ACC1 and ACC2 activity was assessed by Western blot.

4.2.4 Metabolomics and metabolic assays

4.2.4.1 [$^{13}C_6$]-glucose and [$^{13}C_5$]-glutamine tracing

NIH-3T3 cells were seeded at a density of 5 x10^5 cells per well of a 6-well plate in fresh culture medium prepared as described in 3.2.1.1. Five technical replicates seeded in separate plates were used to perform ^{13}C-metabolite measurements in normoxia (21% O_2) and hypoxia (2% O_2). After 24 h, culture medium was removed, followed by two washing steps with DPBS and replaced by tracing media consisting on DMEM without glucose, glutamine and phenol red (Gibco), supplemented with 4.5 mM [$^{13}C_6$]-glucose (Sigma-Aldrich), 2 mM glutamine and, 10% dialyzed FBS (Gibco) prepared on-site. Cells were incubated in tracing media for 1 and 2 h at 37 °C in the culture conditions described in 3.2.1.1. Cells harvested before addition of labeling media were used as tracing negative control. Metabolites were extracted as described in 4.2.4.2.

For experiments using lentiviral transduced NIH-3T3 cells, cells were seeded at a density of 7 x10^5 cells per well of a 6-well plate in fresh culture medium prepared as described in 4.2.1.1. Five technical replicates were used to perform ^{13}C-metabolite measurements in hypoxia (2% O_2). After 24 h, culture medium was replaced with [$^{13}C_6$]-glucose-tracing media as indicated

previously. For [$^{13}C_5$]-glutamine-tracing experiments, media consisted on DMEM without glucose, glutamine and phenol red (Gibco), supplemented with 4.5 mM glucose (Sigma-Aldrich), 2 mM [$^{13}C_5$]-glutamine (Sigma-Aldrich) and, 10% dialyzed FBS (Gibco) prepared on-site. Cells were incubated in tracing media for 1 h, 2 h, and 8 h at 37 °C in the culture conditions described in 3.2.1.1. Cells harvested before addition of labeling media were used as tracing negative control. Metabolites were extracted as described in 4.2.4.2.

4.2.4.2 Extraction of polar metabolites and CoA compounds

Cellular metabolism was quenched after two washing steps using 50 mM Ammonium Carbonate (pH 7.4, adjusted with acetic acid) at RT. Then, cells were placed on ice, followed by the addition of 400 µl of pre-chilled (-20 °C) extraction buffer consisting on 40:40:20 acetonitrile:methanol:water (v/v) and a subsequent incubation step performed at -20 °C for 10 min. After the supernatant was collected and maintained at -20 °C, additional 400 µl of pre-chilled (-20 °C) extraction buffer was added to each well as described previously. After incubation at -20 °C for 10 min, cells were placed on ice and scraped in extraction buffer. The supernatant was collected and pooled with the first obtained extract. Samples were centrifuged at 21,000 x g for 10 min at 4 °C to spin down proteins and cell debris. The supernatant was collected and split in two subsamples used for polar metabolites and CoAs quantification each. Samples were dried in a speed vacuum concentrator and stored at -80 °C. Samples were further processed at the Metabolomics Core Facility of MPI AGE for LC-MS/MS analysis.

Relative metabolite quantification was performed on samples obtained from [$^{13}C_6$]-glucose tracing experiments; hence, no internal standards were added to the extraction buffer. For lentiviral transduced NIH-3T3 cells, absolute metabolite quantification was performed by adding CoA, citric acid, amino acids, and malonyl CoA calibration standards to the extraction buffer. Samples were further processed at the Metabolomics Core Facility of MPI AGE for LC-MS/MS analysis.

4.2.4.3 Phase separation of lipids, metabolites and proteins

Cellular metabolism was quenched after two washing steps using 50 mM Ammonium Carbonate (pH 7.4, adjusted with acetic acid) at RT. Plates were frozen in liquid nitrogen by short (3 s) immersion, and stored at -80 °C until extraction. Exctaction

MTBE extraction of lipids, metabolites and proteins was performed under the hood. For this procedure, 400 µl of pre-chilled (-20 °C) initial extraction buffer were added to each well of the plate. Then, the plate was incubated -20 °C for 10 min. After incubation, plates were placed on ice, scraped and transferred to a 2 mL Eppendorf tube containing 900 µl of pre-chilled (-20 °C) lipid extraction buffer. This solution was maintained at -20 °C. Then, additional 400 µl of pre-chilled (-20 °C) initial extraction buffer were added to each well, followed by an incubation at -20 °C for 10 min. After incubation, plates were scraped and transferred to the first MTBE-containing extracts. Then, samples were incubated in a thermomixer at 4°C for 30 min and 1500 rpm. Samples were centrifuged at 21,000xg for 10 min at 4°C. The supernatant was collected by decantation and mixed with 200 µl of LCMS-grade H_2O. The pellet was stored for proteomic analysis. The supernatant was incubated in a thermomixer at 15°C for 10 min and 1500 rpm. Samples were centrifuged at 16,000xg for 5 min at 15°C. Then, 700 µl of the upper phase (lipids) were collected, dried in a speed vacuum concentrator and stored at -80 °C until analysis. The residual lipid phase was removed by pipetting. Then, the lower phase (polar metabolites) was collected, split in two subsamples used for polar metabolite and malonyl-CoA quantification each. Samples were dried in a speed vacuum concentrator and stored at -80 °C. All samples were further processed at the Metabolomics Core Facility of MPI AGE for LC-MS/MS analysis.

<u>Initial extraction buffer</u>

100 mL of 60% MeOH was prepared using LCMS-Ultra grade wáter. The following standards were added:

10 µl of 2.5 mM U-$^{13}C^{15}N$-amino acids

10 µl of 1 mg/mL $^{13}C_{10}$ ATP

10 µl of 1 mg/mL $^{13}C_{10}{}^{15}N_5$ AMP

10 µl of 1 mg/mL $^{15}N_5$ ADP

20 µl of 100 µg/mL citric acid D4

<u>Lipid extraction buffer</u>

50 mL MTBE

20 µl of EquiSPLASH LIPIDOMIX

4.2.4.4 Oxygen consumption and extracellular acidification rate

The Oxygen Consumption Rate (OCR) and Extracellular Acidification Rate (ECAR) were measured using a Seahorse XFe96 Extracellular Flux Analyzer (Agilent). To maintain sample temperature during the assay, the Seahorse XFe96 analyzer was equilibrated overnight at 37 °C. Next, the Seahorse XFe96 FluxPak cartridge was hydrated in Seahorse XF Calibrant solution, wrapped in plastic and incubated overnight in a 37 °C non-CO_2 incubator. NIH-3T3 cells were plated on XF96 well plates (Agilent) in standard culture medium. Two separate plates were used to perform analysis in normoxia (21% O_2) and hypoxia (2% O_2).

The following day, cells were washed twice with assay medium (Seahorse XF DMEM medium (Agilent) supplemented with 10 mM glucose, 1 mM Sodium Pyruvate, 2 mM L-Glutamine and incubated for 1 h in a 37 °C non-CO_2 incubator. The Seahorse Mito Fuel Flex Test Kit (Agilent) was used to measure metabolic pathway dependency. The test compounds BPTES (3.0 µM) Etomoxir (4.0 µM) and, UK5099 (2.0 µM) were diluted and loaded into the cartridge according to manufacturer's instructions. Injection strategies, OCR and ECAR measurements were recorded using the manufacturer's pre-programmed protocol. After the assay, protein concentration per well was quantified using the BCA Protein Assay Kit (Thermo Scientific) and subsequently used to normalize OCR and ECAR measurements. Seahorse data were collected using Wave Controller 2.6 (Agilent) and analyzed using GraphPad Prism (version 9.5.1).

4.2.5 Proteomics

4.2.5.1 Protein and peptide sample preparation

Protein pellets were obtained from samples prepared for metabolomics studies as described in 4.2.4.1. Pellets were resuspended in Guanidium chloride (GuHCl) lysis buffer and heated at 95°C for 10 min. Then, the lysate was sonicated using a Bioruptor sonicator (Diagenode) (10 cycles, 30s sonication, 30s break, high performance mode). The lysate was centrifuged at 20,000xg for 20 min. The supernatant was kept, and 2 µl were used for 1:10 dilution in 20mM Tris. Protein concentration of the diluted supernatant was assessed with Nanodrop. Then, 300 µg of non-diluted supernatant were diluted 1:10 in 20mM Tris and digested with Trypsin-Gold (Promega) using a 1:200 dilution. Trypsin digestion was performed overnight at 37 °C. On the following day, trypsin digestion was stopped using 1% formic acid (Thermo Fisher Scientific). Peptides were centrifuged at 20,000xg for 10 min, and cleaned with

custom-packed C18-SD STAGE tips (Rappsilber et al., 2003). Peptides were further processed at the Proteomics Core Facility of MPI AGE by Xinping Li and Illian Atanassov.

Guanidium chloride (GuHCl) lysis buffer
6M GuHCl
2.5mM TCEP
10mM CAA
100mM Tris-HCl

4.2.5.2 TMT labeling, Mass Spectrometry (MS) and analysis

The procedure described this section was performed at the Proteomics Core Facility of the Max Planck Institute for Biology of Ageing, particularly by Dr. Xinping Li and Dr. Ilian Atanassov.

Four micrograms of desalted peptides were labeled with tandem mass tags (TMT10plex, Thermo Fisher) using a 1:20 ratio of peptides to TMT reagent. TMT labeling was carried out according to manufacturer's instruction with the following changes: dried peptides were reconstituted in 9µL 0.1M TEAB to which 7µL TMT reagent in acetonitrile (ACN) was added to a final ACN concentration of 43.75%, after 60 min of incubation at room temperature the reaction was quenched with 2µL 5% hydroxylamine. Labeled peptides were pooled, dried, resuspended in 0.1% formic acid (FA), split into two samples, and desalted using home-made C18 STAGE tips (Rappsilber et al., 2003).

One of the two samples was fractionated on a 150mm, 300µm, 2µm C18, AcclaimPepMap (Thermo Fisher) column using a Ultimate3000 (Thermo Fisher). The column was maintained at 30°C. Buffer A was 5% acetonitrile 0.01M ammonium bicarbonate, buffer B was 80% acetonitrile 0.01M ammonium bicarbonate. Separation was performed using a segmented gradient from 1% to 50% buffer B, for 90min and 50% to 95% for 20 min with a flow of 4µL/min. Fractions were collected every 150 sec and combined into nine fractions by pooling every ninth fraction. Pooled fractions were dried in Concentrator plus (Eppendorf), resuspended in 2µL 0.1% FA for mass spectrometric analysis. Peptides were separated on

a 50cm, 75µm Acclaim PepMap column (Thermo Fisher) using a 120min linear, 6% to 31% buffer B; buffer A was 0.1% FA, buffer B was 0.1% FA, 80% ACN. The column was maintained at 50°C. Eluting peptides were analyzed on an Orbitrap Lumos Tribrid mass spectrometer (Thermo Fisher). Synchronous precursor selection based MS3 was used for TMT reporter ion signal measurements. Proteomics data was analysed using MaxQuant version 1.5.2.8 (Cox & Mann, 2008). Differential expression analysis was performed using limma in R (Ritchie et al., 2015).

4.2.6 Imaging

4.2.6.1 Histone PTMs immunofluorescence staining

Cells were seeded in 8-well chamber slides (Ibidi) following the experimental treatment indicated accordingly. Upon treatment completion, cells were fixed in pre-warmed (37°C) fixation buffer for 15 min on a rocking platform. Unless otherwise stated, all imaging preparation steps were performed on a rocking platform. Cells were washed 1x in PBS for 5 min, at room temperature. Then, cells were permeabilized with 0.1% Triton X-100 diluted in PBS for 5 min. Cells were blocked using 5% BSA diluted in 0.1% Triton X-100 diluted in PBS for 45 min at RT. Cells were then incubated with the indicated primary antibodies (Table 3) diluted 1:100 in blocking buffer. Primary antibody incubation was performed overnight at 4°C. Cells were washed 3x in PBS for 5 min at RT. Cells were then incubated with the corresponding fluorescent secondary antibodies diluted 1:500 in blocking buffer. Secondary antibody incubation was performed for 1 h at RT protected from light. The subsequent steps were performed protected from light. Cells were washed 2x with PBS for 5 min. DAPI staining was performed using a 1:1000 dilution in methanol for 5 min. Cells were washed 2x with PBS for 5 min. Then, immersion oil (Ibidi) was added to the slides. Cells were stored at 4°C until imaging.

Fixation buffer

3.7% formaldehyde diluted in MEMα (Thermo Fisher Scientific)

Blocking buffer

1% BSA in PBS

4.2.6.2 Histone PTMs immunofluorescence microscopy

Fluorescent images were obtained using laser scanning confocal microscopy (Leica TCS SP8 DLS), with the integrated Leica Application Suite software. Images were acquired at room temperature using the 63x glycerol immersion objective. Image acquisition was performed using the same settings in all experiments.

4.2.6.3 Histone PTMs immunofluorescence analysis

Images were analyzed using Fiji (Schindelin et al., 2012). Quantification of fluorescent intensities was performed using background subtraction (rolling ball radius: 50) and noise despeckle. Imaging experiments were performed using n=3/4 biologically independent replicates, and 2 technical replicates including 180 cells per condition.

4.2.7 Data and statistical analysis

4.2.7.1 GO enrichment analysis

Metascape was used for GO analysis (Zhou et al., 2019) using *Mus musculus* as input species.

4.2.7.2 Semi-targeted liquid chromatography-high-resolution mass spectrometry-based (LC-HRS-MS) analysis of amine-containing metabolites

The procedure described this section was performed at the Metabolomics Core Facility of the Max Planck Institute for Biology of Ageing.

The LC-HRMS analysis of amine-containing compounds was performed using an adapted benzoylchlorid-based derivatization method (Wong et al., 2016). In brief: The polar fraction of the metabolite extract was re-suspended in 200 µL of LC-MS-grade water (Optima-Grade, Thermo Fisher Scientific) and incubated at 4°C for 15 min on a thermomixer. The re-suspended extract was centrifuged for 5 min at 16.000 x g at 4°C and 50 µL of the cleared supernatant were mixed with 25 µl of 100 mM sodium carbonate (Sigma), followed by the addition of 25 µl 2% [v/v] benzoylchloride (Sigma) in acetonitrile (Optima-Grade, Thermo Fisher Scientific). Samples were vortexed and kept at 20°C until analysis. After a 5 min centrifugation at 16.000 x g at 20°C, the cleared supernatant was transferred to glass autosampler vials with 300 µl glass inserts (Chromatography Accessories Trott, Germany).

For the LC-HRMS analysis, 1 µl of the derivatized sample was injected onto a 100 x 2.1 mm HSS T3 UPLC column (Waters) with 1.8 µm particle size. The flow rate was set to 400 µl/min using a binary buffer system consisting of buffer A (10 mM ammonium formate (Sigma), 0.15% [v/v] formic acid (Sigma) in LC-MS-grade water (Optima-Grade, Thermo Fisher Scientific). Buffer B consisted solely of acetonitrile (Optima-grade, Thermo Fisher-Scientific). The column temperature was set to 40°C, while the LC gradient was: 0% B at 0 min, 0-15% B 0- 4.1min; 15-17% B 4.1 – 4.5 min; 17-55% B 4.5-11 min; 55-70% B 11 – 11.5 min, 70-100% B 11.5 - 13 min; B 100% 13 - 14 min; 100-0% B 14 -14.1 min; 0% B 14.1-19 min; 0% B. The mass spectrometer (Q-Exactive Plus, Thermo Fisher Scientific) was operating in positive ionization mode recording the mass range m/z 100-1000. The heated ESI source settings of the mass spectrometer were: Spray voltage 3.5 kV, capillary temperature 300°C, sheath gas flow 60 AU, aux gas flow 20 AU at a temperature of 330°C and the sweep gas to 2 AU. The RF-lens was set to a value of 60.

Thermo raw data files were converted to mzXML files by MSConvert from Proteowizard (http://proteowizard.sourceforge.net) (Chambers et al., 2012). The semi-targeted LC-MS data analysis was performed using the El Maven software (Version v0.10.0, Elucidata) (Agrawal et al., 2019). Chromatographic peaks were automatically picked and matched to an In-House database (5 ppm, 0.2 min). The identity of each compound was in addition validated by authentic reference compounds, which were measured at the beginning and the end of the sequence.

4.2.7.3 Targeted liquid chromatography triple quad mass spectrometry (LC-TQ-MS) analysis of fatty acyl Coenzyme A species (Acyl-CoAs) metabolites

The procedure described this section was performed at the Metabolomics Core Facility of the Max Planck Institute for Biology of Ageing.

The LC-TQ-MS analysis of Acyl-CoAs was performed using an adapted protocol based (Abrankó et al., 2018). In brief: The polar fraction of the metabolite extract was re-suspended in 50 µL of LC-MS-grade water (Optima-Grade, Thermo Fisher Scientific). After 15 min incubation on a thermomixer at 4°C and a 5 min centrifugation at 16.000 x g at 4°C, the

cleared supernatant was transferred to glass autosampler vials with 300 µl glass inserts (Chromatography Accessories Trott, Germany).

For the LC-TQMS analysis, 4 µl of the sample was injected onto a 100 x 2.1 mm BEH Amide UPLC column (Waters) with 1.7 µm particle size. The flow rate was set to 450 µl/min using a quaternary buffer system consisting of buffer A 5 mM ammonium acetate (Sigma) in LC-MS-grade water (Optima-Grade, Thermo Fisher Scientific). Buffer B consisted of 5 mM ammonium acetate (Sigma) in 95% acetonitrile (Optima-grade, Thermo Fisher-Scientific). Buffer C consisted of 0.1% phosphoric acid (85%, VWR) in 60% acetonitrile (acidic wash) and buffer D of 50% acetonitrile (neutral wash). The column temperature was set to 30°C, while the LC gradient was: 95-20% B 0- 7min; 100% C 7.1 – 17 min, 100% D 17.1 - 22 min; followed by re-equilibration 95% B 22.1 - 30 min. The mass spectrometer (TQs, Waters) was operating in positive ionization mode recording the mass transitions for Coenzyme A as quantifier was used 768 to 261 m/z; for Acetyl CoA as quantifier was used 810 to 303 m/z; for Butyryl-CoA as quantifier was used 838 to 428 m/z; for Malonyl-CoA as quantifier was used 854 to 303 m/z, for Succinyl-CoA as quantifier was used 868 to 428 m/z for $^{13}C_2$-Acetyl CoA as quantifier was used 812 to 305 m/z; for $^{13}C_3$-Malonyl-CoA as quantifier was used 857 to 305 m/z. Identity of all Acyl-CoAs were validated by authentic reference compounds. The heated ESI source settings of the mass spectrometer were: Capillary voltage 1.5 kV, Source temperature 150°C, Desolvation temperature 500°C, Cone gas flow 150 L/HR, Desolvation gas flow 800 L/HR.

Waters raw data files were converted to mzXML files by MSConvert from Proteowizard (http://proteowizard.sourceforge.net) (Chambers et al., 2012). The targeted LC-MS data analysis was performed using the El Maven software (Version v0.12.0, Elucidata (Agrawal et al., 2019). Chromatographic peaks were manually picked and matched to an In-House database. The identity of each compound was validated by authentic reference compounds.

4.2.7.4 Anion-Exchange Chromatography Mass Spectrometry (AEX-MS) for the analysis of anionic metabolites

The procedure described this section was performed at the Metabolomics Core Facility of the Max Planck Institute for Biology of Ageing.

Extracted metabolites were re-suspended in 200 µl of Optima UPLC/MS grade water (Thermo Fisher Scientific). After 15 min incubation on a thermomixer at 4°C and a 5 min centrifugation at 16.000 x g at 4°C, 100 µl of the cleared supernatant were transferred to p*olypropylene* autosampler vials (Chromatography Accessories Trott, Germany). The samples were analysed using a Dionex ionchromatography system (Integrion, Thermo Fisher Scientific) as described previously (Schwaiger et al., 2017). . In brief, 5 µL of polar metabolite extract were injected in full loop mode using an overfill factor of 1, onto a Dionex IonPac AS11-HC column (2 mm × 250 mm, 4 µm particle size, Thermo Fisher Scientific) equipped with a Dionex IonPac AG11-HC guard column (2 mm × 50 mm, 4 µm, Thermo Fisher Scientific). The column temperature was held at 30°C, while the auto sampler was set to 6°C. A potassium hydroxide gradient was generated using a potassium hydroxide cartridge (Eluent Generator, Thermo Scientific), which was supplied with deionized water. The metabolite separation was carried at a flow rate of 380 µL/min, applying the following gradient conditions: 0-3 min, 10 mM KOH; 3-12 min, 10−50 mM KOH; 12-19 min, 50-100 mM KOH, 19-21 min, 100 mM KOH, 21-22 min, 100-10 mM KOH. The column was re-equilibrated at 10 mM for 8 min.

For the analysis of metabolic pool sizes the eluting compounds were detected in negative ion mode using full scan measurements in the mass range m/z 50 – 750 on a Q-Exactive HF high resolution MS (Thermo Fisher Scientific). The heated electrospray ionization (ESI) source settings of the mass spectrometer were: Spray voltage 3.2 kV, capillary temperature was set to 275°C, sheath gas flow 70 AU, aux gas flow 15 AU at a temperature of 350°C and a sweep gas flow of 0 AU. The S-lens was set to a value of 50.

Thermo raw data files were converted to mzXML files by MSConvert from Proteowizard (http://proteowizard.sourceforge.net) (Chambers et al., 2012). The semi-targeted LC-MS data analysis was performed using the El Maven software (Version v0.10.0, Elucidata) (Agrawal et al., 2019). Chromatographic peaks were automatically picked and matched to an In-House database (5 ppm, 0.2 min). The identity of each compound was in addition validated by authentic reference compounds, which were measured at the beginning and the end of the sequence. Isotopomer distribution was corrected for natural abundant isotopes with the IsoCorrectoR package in R (Heinrich et al., 2018).

4.2.7.5 Statistical analysis

Statistical analysis was performed using GraphPad Prism (version 9.5.1). Figure legends indicate the statistical test used for the specified dataset, and obtained p values.

5 RESULTS

To address the interplay of metabolism and chromatin and to assess how differences in metabolite cycling directly impact chromatin modifications, we used alterations in oxygen tensions as a model. We shifted NIH-3T3 from normoxia (21% O_2) to hypoxia (2% O_2) for 24 h. When cells are exposed to lower oxygen conditions, glucose metabolism is enhanced through a higher glucose uptake from the extracellular space and increased glycolytic rate, followed by the redirection of glucose-derived pyruvate towards lactate production instead of entrance into the tricarboxylic acid (TCA) cycle (Eales et al., 2016; Vander Heiden et al., 2009). We first evaluated the formation kinetics of glucose-derived metabolites in the context of central carbon metabolism (CCM) using stable isotope tracing to determine metabolic pathway activity. We pulsed cells with uniformly labeled [$^{13}C_6$]-glucose as the sole source of glucose and harvested metabolites at 1 h after the switch to determine incorporation of the label (Zamboni et al., 2009) (Figure 6A). We aimed to reduce exogenous sources of glucose by adding dialyzed FBS to the media. Using liquid chromatography coupled with high-resolution mass spectrometry (LC-HRMS), we measured the incorporation of ^{13}C isotopes into CCM (Violante et al., 2019) (Figure 6B). We could measure a significant [$^{13}C_6$]-glucose uptake and ^{13}C incorporation into downstream glycolytic intermediates (Figure 6C). At this time point, we noted a similar enrichment in hypoxia compared to normoxia. Consistent with these results, we found comparable enrichment in [$^{13}C_3$]-pyruvate and [$^{13}C_3$]-lactate for both oxygen conditions. In contrast, enrichment in [$^{13}C_3$]-serine and [$^{13}C_3$]-glycine decreased in hypoxia (Figure 6D). As a further evaluation of glucose metabolism, we monitored ^{13}C incorporation into the pentose phosphate pathway (PPP) and observed similar kinetics in hypoxia compared to normoxia (Figure 6E). Together, these findings suggest that glycolytic intermediates and the PPP maintained their glucose-derived carbon flux after cells were exposed to hypoxia for 24h.

Next, we aimed to investigate whether glycolysis-derived [$^{13}C_3$]-pyruvate continued to supply the TCA cycle during hypoxia. In contrast to our observations for glycolysis and the PPP, ^{13}C incorporation into TCA cycle intermediates (Figure 6F), and their derived amino acids (Figure 6G) decreased. Collectively, our results indicate a reduced activity in the TCA cycle, confirming its dependence on oxygen concentration and confirming [$^{13}C_2$]-citrate as a critical reduction step of ^{13}C incorporation in the transition from glycolysis to the TCA cycle.

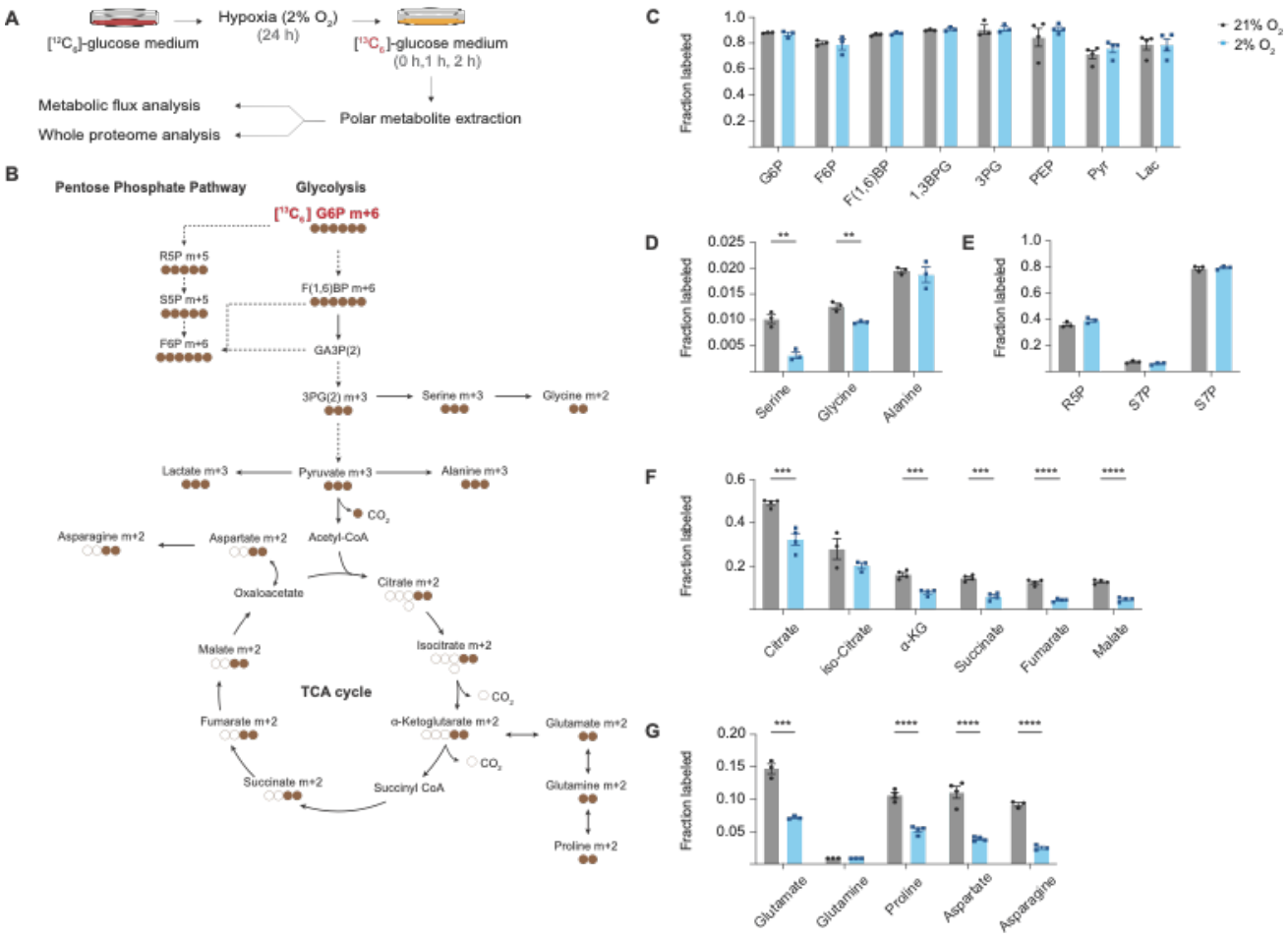

Figure 6. TCA cycle intermediates are downregulated in hypoxic-cultured cells.

(A) Experimental design of [$^{13}C_6$]-glucose tracing assays in NIH-3T3 cells cultured in hypoxia (2% O_2) for 24 h. Cells grown in normoxia (21% O_2) were used as negative control. **(B)** Schematic depicting the ^{13}C-labeling pattern derived from [$^{13}C_6$]-glucose metabolism in glycolysis, pentose phosphate pathway (PPP), and first-turn TCA cycle metabolites. Empty circles represent ^{12}C-atoms, and filled circles represent ^{13}C-atoms. Mass isotopomers are represented as m+. **(C)**^{13}C-incorporation into glycolytic metabolites, **(D)** glycolysis-derived amino acids, **(E)** PPP metabolites, **(F)** TCA cycle metabolites and, **(G)** TCA cycle-derived amino acids. Data is represented as individual values ± S.E.M. Significance was defined as follows: n.s. (not shown abbreviation) > 0.05; *p≤ 0.05; **p≤ 0.01; ***p≤ 0.001; and ****p ≤ 0.001, as assessed by multiple paired t-test. Abbreviations: G6P – Glucose-6-phosphate, F6P – Fructose-6-phosphate, F(1,6)BP – Fructose-1,6-bisphosphate, G3P – Glyceraldehyde-3-phosphate, 3PG – 3-phosphoglycerate, Pyr – Pyruvate, Lac – Lactate, R5P -Ribose-5-phosphate, S7P – Sedoheptulose-7-phosphate, αKG – alpha-ketoglutarate.

5.1 Levels of acetyl-CoA and histone acetylation increase in hypoxia

Intracellular metabolite concentrations can regulate chromatin structure and function as some chromatin-modifying enzymes use metabolites as cofactors to establish a diverse set of histone post-translational modifications (PTMs) (Dai et al., 2020; Li et al., 2018). Histone acetylation is an abundant PTM that alters chromatin structure by neutralizing the positive charge of histone tails and destabilizing the physical contact between histones and DNA (Bannister & Kouzarides, 2011; Zhou et al., 2011). Therefore, histone acetylation increases chromatin accessibility and is fundamental for transcriptional activation and gene expression control.

Acetyl-CoA is the acetyl donor used by histone acetyltransferases (HAT) to acetylate lysine residues on histones (Pietrocola et al., 2015; Sivanand et al., 2018). Nevertheless, a growing catalog of small acyl-CoAs with similar chemical properties to acetyl-CoA has been characterized as cofactors for newly discovered histone PTMs (i.e., butyrylation, malonylation, and succinylation) (Bannister & Kouzarides, 2011; Shvedunova & Akhtar, 2022). Hence, we were prompted to characterize the metabolic pool size of small acyl-CoAs using targeted metabolite analysis. Since the metabolic pool size indicates the absolute or relative amount of a metabolite, it is independent and complementary to the information obtained from stable isotope tracing that measures metabolic turnover rates (Jang et al., 2018). Therefore, for metabolic pool size quantification, isotope labeling is unnecessary. We thus extracted whole-cell level small intracellular acyl-CoAs from normoxia-cultured and hypoxia-cultured cells grown in standard media supplemented with non-dialyzed FBS. Next, we quantified small acyl-CoAs pool size using LC-MS. Acetyl-CoA levels increased during hypoxia, as opposed to the other acyl-CoAs, whose levels remained stable (Figure 7). We were surprised to find that acetyl-CoA levels increased since our findings on [$^{13}C_6$]-glucose tracing revealed lower labeling incorporation into citrate, a metabolite synthesized from acetyl-CoA and oxaloacetate in mitochondria. Acetyl-CoA is distributed into separate mitochondrial and nuclear-cytosolic pools that generate distinctive functional roles (Pietrocola et al., 2015; Sivanand et al., 2018). Since our data showed a higher acetyl-CoA pool size but a lower citrate synthesis, we hypothesized the metabolic fate of acetyl-CoA might enrich the nuclear-cytosolic pool and, potentially, influence histone acetylation.

Taken together, these data indicate a specific increase in whole-cell acetyl-CoA levels upon hypoxia, suggesting that the higher availability of this metabolite might impact histone acetylation in the nuclei.

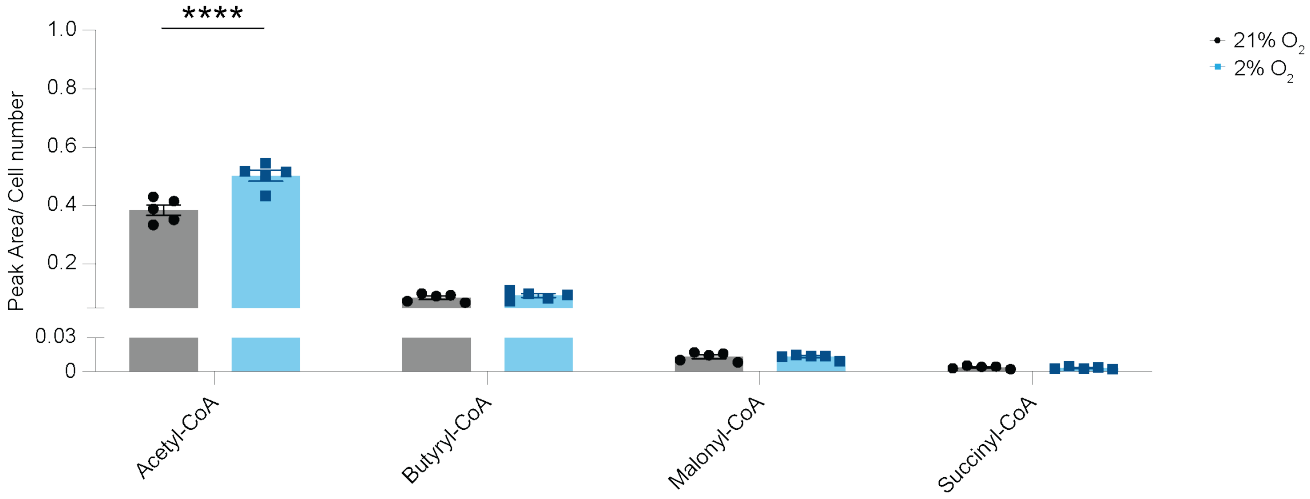

Figure 7. Acetyl-CoA is upregulated in hypoxia.

Acyl-CoA compounds were quantified by liquid chromatography – mass spectrometry (LC-MS) from NIH-3T3 cells cultured in normoxia (21% O_2) and hypoxia (2% O_2) for 24 h. Measurements correspond to MS peak area normalized to cell number. Data is represented as individual values ± S.E.M. Significance was defined as follows: n.s. (not shown abbreviation) > 0.05; and ****p ≤ 0.001, as assessed by multiple paired t-test.

To gain insight into how hypoxia impacts histone PTMs, we first purified histones from NIH-3T3 using acid extraction. We next evaluated the acetylation and methylation enrichment on global and particular lysine residues of histone H3 and histone H4 via immunoblotting (Figure 8A). Interestingly, only H3K27ac was discernibly enriched in hypoxia-cultured cells. We confirmed H3K27ac enrichment by immunofluorescence (Figure 8B). Since H3K27ac is a histone PTM associated with active enhancers and promoters (Zhang et al., 2020), our results suggest that increased chromatin accessibility and potentially higher active transcription might play an important role in the adaptation to hypoxia.

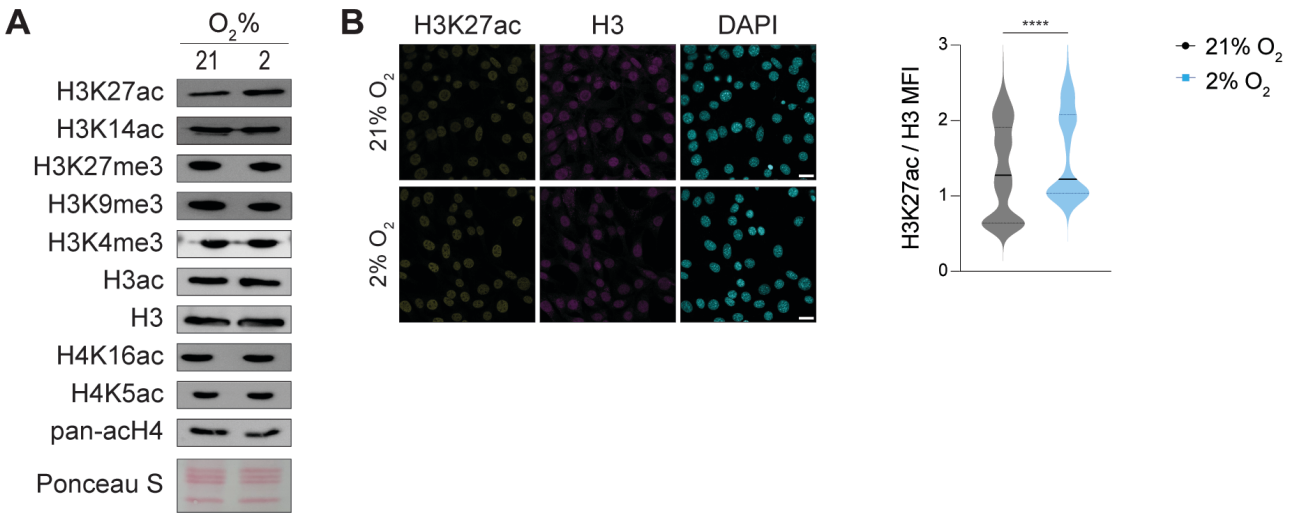

Figure 8. H3K27ac levels are increased upon exposure to hypoxia.

(A) Representative immunoblots for histone PTMs from NIH-3T3 cells cultured in normoxia (21% O_2) and hypoxia (2% O_2) for 24 h. **(B)** Representative immunofluorescence images and quantification of H3K27ac (yellow), H3 (magenta), and nuclear (DAPI, cyan) from normoxia-cultured and hypoxia-cultured NIH-3T3 cells. H3 was used as internal control for H3K27ac signal normalization. Data is represented as individual values ± S.E.M. Significance was defined as follows: ****p ≤ 0.001, as assessed by paired t-test. Scale bar 20 µm.

5.2 Hypoxia remodels the proteome enhancing glycolysis and suppressing the TCA cycle

Harvesting metabolites with a monophasic solvent system (acetonitrile:methanol:water) allowed us to separate proteins from cells incubated in uniformly labeled [$^{13}C_6$]-glucose (Prasannan et al., 2018). To assess quantitative changes in protein concentration during hypoxia, we then examined the extracted proteins by LC-MS using tandem mass tags (TMT). We identified 7573 proteins in total, with 819 proteins upregulated and 744 downregulated in hypoxia versus normoxia (Figure 9A). We then performed a gene ontology (GO) enrichment for biological processes (BP) to allocate functional categories to upregulated and downregulated proteins separately. Analysis of upregulated proteins revealed enrichment in proteins implicated in the generation of precursor metabolites, actin cytoskeleton organization, and glucose catabolic processes (Figure 9B). On the other hand, analysis of downregulated proteins showed enrichment of proteins involved in ribosome biogenesis, DNA metabolic process, and regulation of chromosome organization (Figure 9C).

To further allocate hypoxia-responsive proteins to functional categories, we manually annotated CCM protein enrichment. We identified that the enrichment of glycolytic enzymes

was upregulated, as opposed to our observations on the TCA cycle that showed enzymatic downregulation (Figure 9D). In contrast, PPP enzymes showed comparable enrichment in hypoxia compared to normoxia. Since these data suggested a metabolic rewiring towards upregulation of glycolysis and downregulation of the TCA cycle, we reasoned that enzymes involved in pyruvate metabolism could play fundamental roles in the observed adaptation to hypoxia, as pyruvate directly connects glycolysis to the TCA cycle. To address this question, we analyzed the expression of enzymes related to downstream pathways of pyruvate metabolism, explicitly focusing on lactate and acetyl-CoA metabolism. Interestingly, LDHA, ACSS2, and PDHK1 were upregulated in hypoxia as detected by LC-MS (Figure 9E) and further confirmed by immunoblotting (Figure 9F).

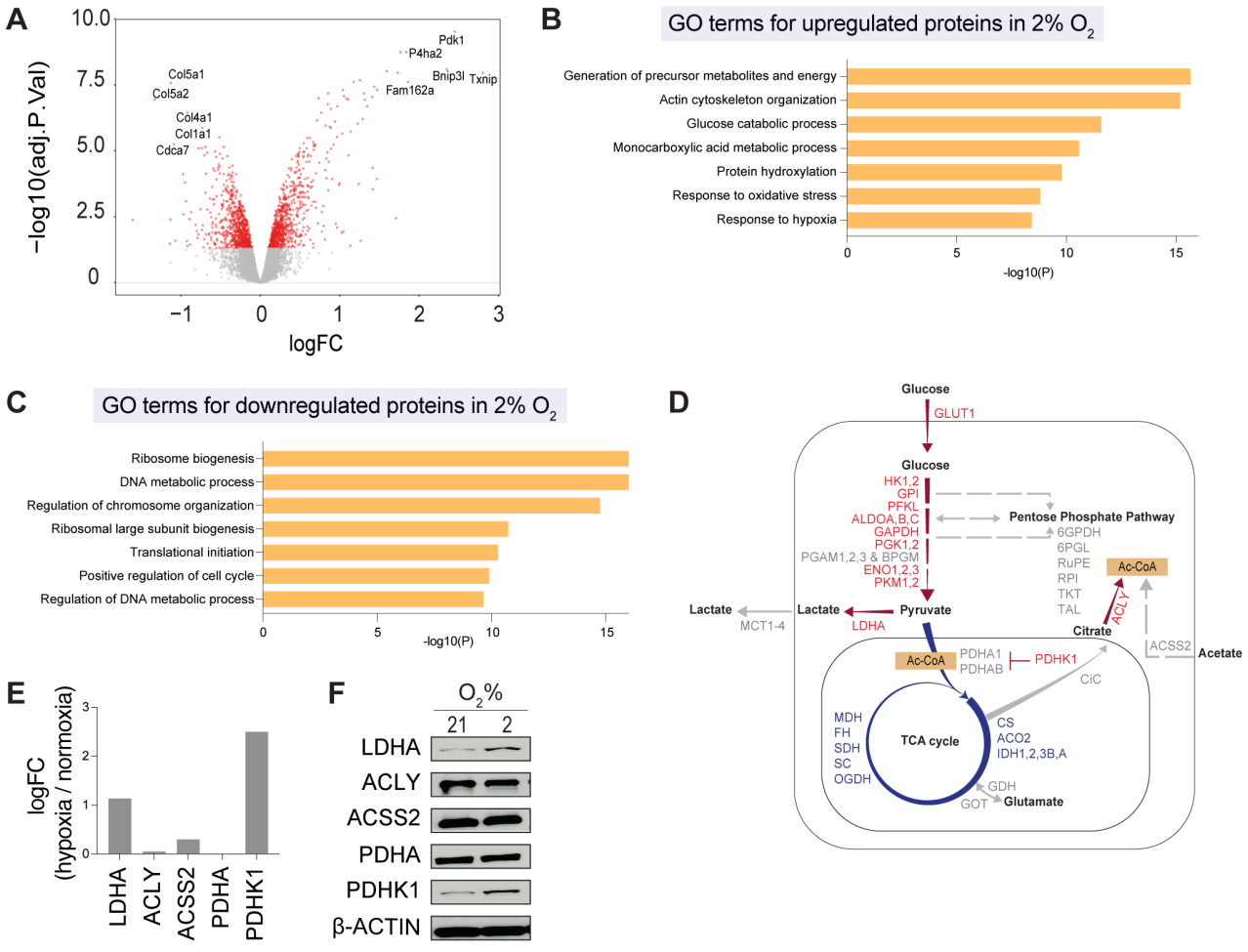

Figure 9. Hypoxia upregulates protein expression of enzymes related to glycolysis and acetyl-CoA metabolism.

(A) Volcano plot of significantly enriched proteins in hypoxia detected by LC-MS. Differentially expressed proteins are colored red. **(B)** Gene Ontology (GO) term analysis for biological processes (BP) of upregulated

proteins, and **(C)** downregulated proteins. **(D)** Schematic of protein enrichment in CCM. Upregulated enzymes and downregulated enzymes are colored red and blue, respectively. Non-differentially enriched enzymes are colored grey. **(E)** Enrichment of enzymes related to downstream pathways of pyruvate metabolism and, **(F)** its representative immunoblotting. β-ACTIN is used as protein loading control.

5.3 Hypoxia activates a glycolytic gene-expression program

To comprehensively determine the molecular mechanisms involved in the hypoxia response, we sought to characterize the transcriptome using RNA-sequencing (RNA-seq). Surprisingly, we only found 146 differentially expressed genes, with 101 genes upregulated and 45 genes downregulated (Figure 10A). GO term analysis for BP of upregulated genes identified genes that play a role in glycolysis, protein hydroxylation, and cellular response to hypoxia as the most enriched BP (Figure 10B). Interestingly, BP involved in downstream pathways of glucose metabolism, such as PPP, fructose, and pyruvate metabolism, were also upregulated. Intriguingly, we detected no clear signature on transcriptome rewiring of TCA cycle genes. Given the relatively small number of downregulated genes, we further analyzed the upregulated transcriptomic dataset. We found that *Pdk1* was one of the most responsive genes to hypoxia (Figure 10C), similarly to our previous observations on the proteome that also detected PDHK1 upregulation. Collectively, our data suggest a moderate transcriptomic response to hypoxia characterized by a substantial enhancement of glucose metabolism without a clear TCA cycle remodeling signature.

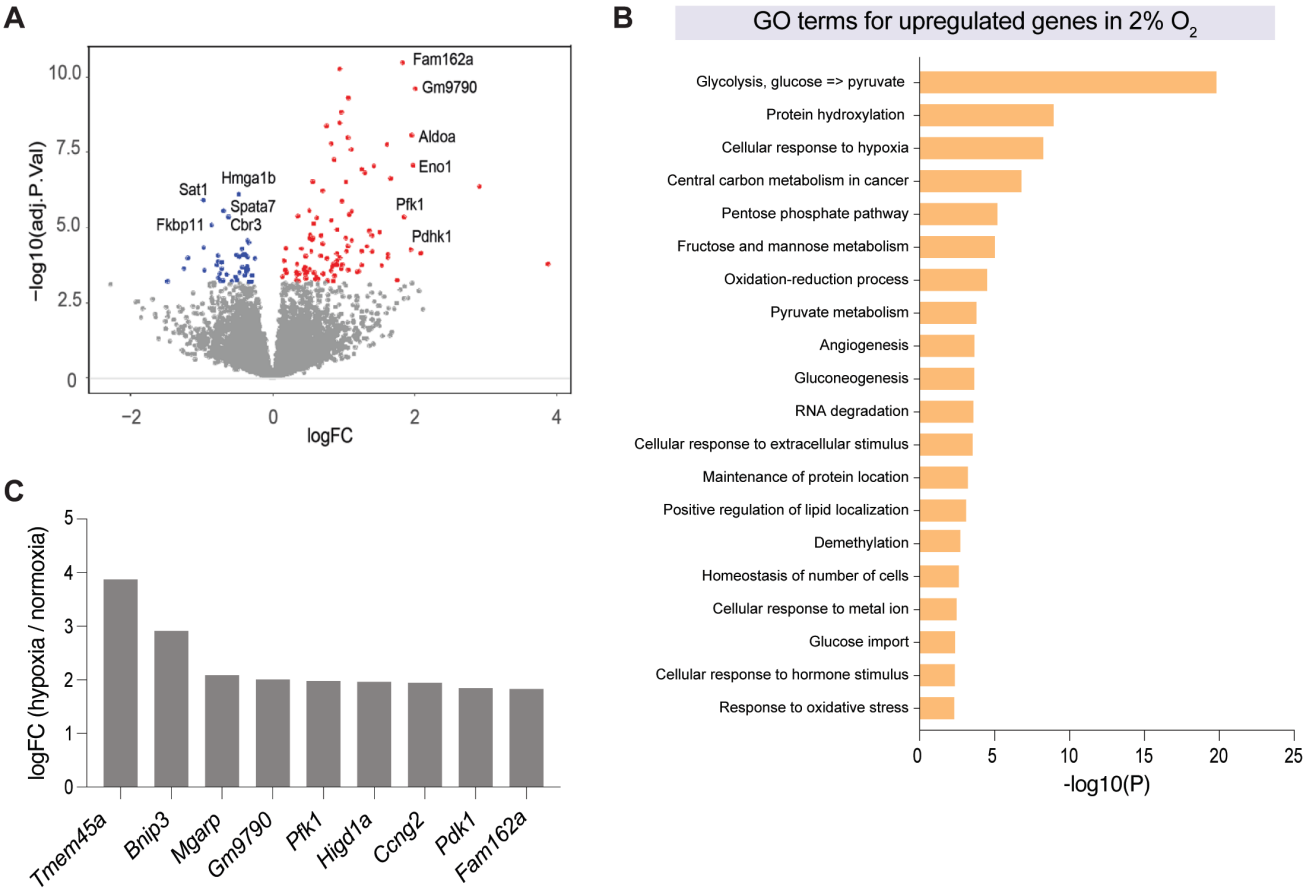

Figure 10. Hypoxia redirects the transcriptome towards glucose metabolism.

(A) Volcano plot of significantly enriched genes in hypoxia (2% O_2) vs normoxia (21% O_2) Upregulated genes and downregulated genes are colored red and blue, respectively (padj< 0.05). **(B)** Gene Ontology (GO) term analysis for biological processes (BP) of upregulated genes. **(C)** Enrichment of the most upregulated genes in hypoxia. logFC of hypoxia was adjusted to logFC in normoxia.

5.4 PDHK1 deficiency maintains proliferation and mitochondrial respiration

PDHK1 is a protein kinase that inhibits the pyruvate dehydrogenase complex (PDC), the multienzyme complex that synthesizes acetyl-CoA from pyruvate in mitochondria (Figure 11A) (Kantor et al., 2001; Rardin et al., 2009). Condensation of acetyl-CoA and oxaloacetate generates citrate and fuels the TCA cycle; thus, PDH inhibition by PDHK1 can decrease acetyl-CoA levels and diminish TCA cycle activity. Interestingly, our observations on PDHK1 upregulation as part of the hypoxia response showed lower TCA cycle activity but higher levels of acetyl-CoA. Thus, we next aimed to dissect how PDHK1 might regulate acetyl-CoA synthesis in hypoxia. To test this, we depleted PDHK1 using stable lentiviral shRNA delivery in hypoxia-cultured NIH-3T3 cells (Figure 11B). Proliferation under PDHK1 depletion remained stable in KD cells compared to the control (Figure 11C).

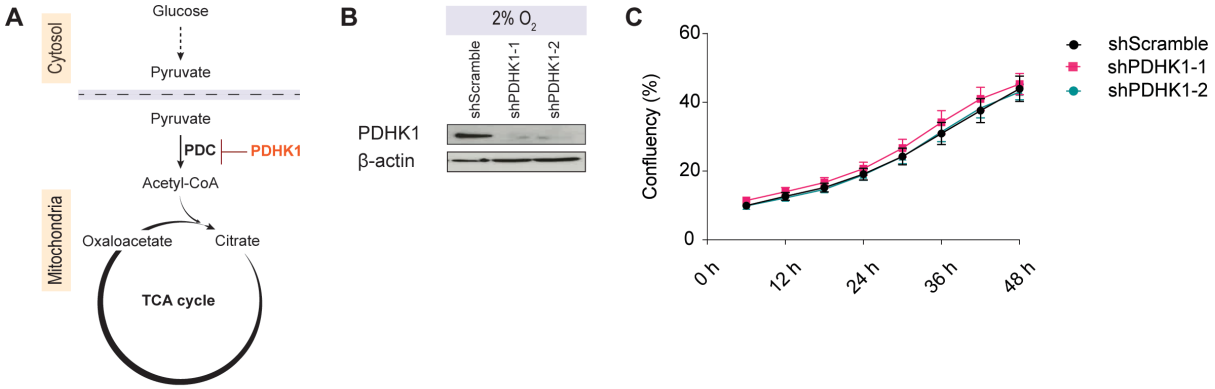

Figure 11. Proliferation remains stable upon PDHK1 deficiency.

(A) Schematic of PDHK1 function in mitochondria. **(B)** Representative immunoblots depicting the endogenous PDHK1 and β-ACTIN protein levels in hypoxia-cultured NIH-3T3 cells expressing short hairpin PDHK1 (shPDHK1 and shPDHK1-2) and scramble RNA (shScramble). **C)** Proliferation curve of PDHK1-depleted cells and control cells cultured in hypoxia. Error bars represent mean ± S.E.M of three independent biological replicates (n=3) run in triplicates.

Mitochondrial-derived acetyl-CoA is mainly synthesized from pyruvate, fatty acid (FA) oxidation and glutamine metabolism (Zhao et al., 2016). To characterize the activity of these pathways under PDHK1 depletion, we conducted Seahorse assays. For this, we inhibited each pathway separately using BPTES (inhibits glutamine to glutamate conversion), etomoxir (inhibits FA cytosolic-to-mitochondrial translocation), and UK5099 (inhibits pyruvate import into the mitochondria) (Figure 12A). Oxygen consumption rate (OCR) and extracellular acidification rate (ECAR) were measured to assess mitochondrial respiration and glycolytic activity, respectively.

We first characterized basal respiration measuring OCR and ECAR values prior to inhibitor injection. While the OCR showed no difference between KD cells compared to the control (Figure S1A), we observed higher ECAR upon PDHK1-KD (Figure 12B), suggesting that PDHK1 depletion does not affect mitochondrial respiration but generates a glycolytic response in basal conditions.

We next examined the metabolic activity of each pathway evaluating the OCR and ECAR profiles after pathway inhibition. We observed a moderately affected OCR in KD cells compared to the control (Fig S1B-D) and higher ECAR upon the inhibition of glutamine, lipid and glucose oxidation in mitochondria (Figure 12C-E). Since we observed similar ECAR values for the inhibitors evaluated, we hypothesize that the effect of PDHK1 depletion

generates an acute glycolytic response that does not depend on the oxidation of the evaluated metabolites under our specific testing conditions.

Taken together, our data indicate that PDHK1 depletion has no significant impact on mitochondrial respiration when glutamine, lipid, or glucose oxidation is blocked. On the contrary, glycolytic activity increased robustly after the utilization of these metabolic sources was impaired. Therefore, given that glycolysis is restricted to the cytosol, we hypothesize PDHK1 depletion might exacerbate a cytosolic rather than mitochondrial response upon fuel oxidation blockage in mitochondria.

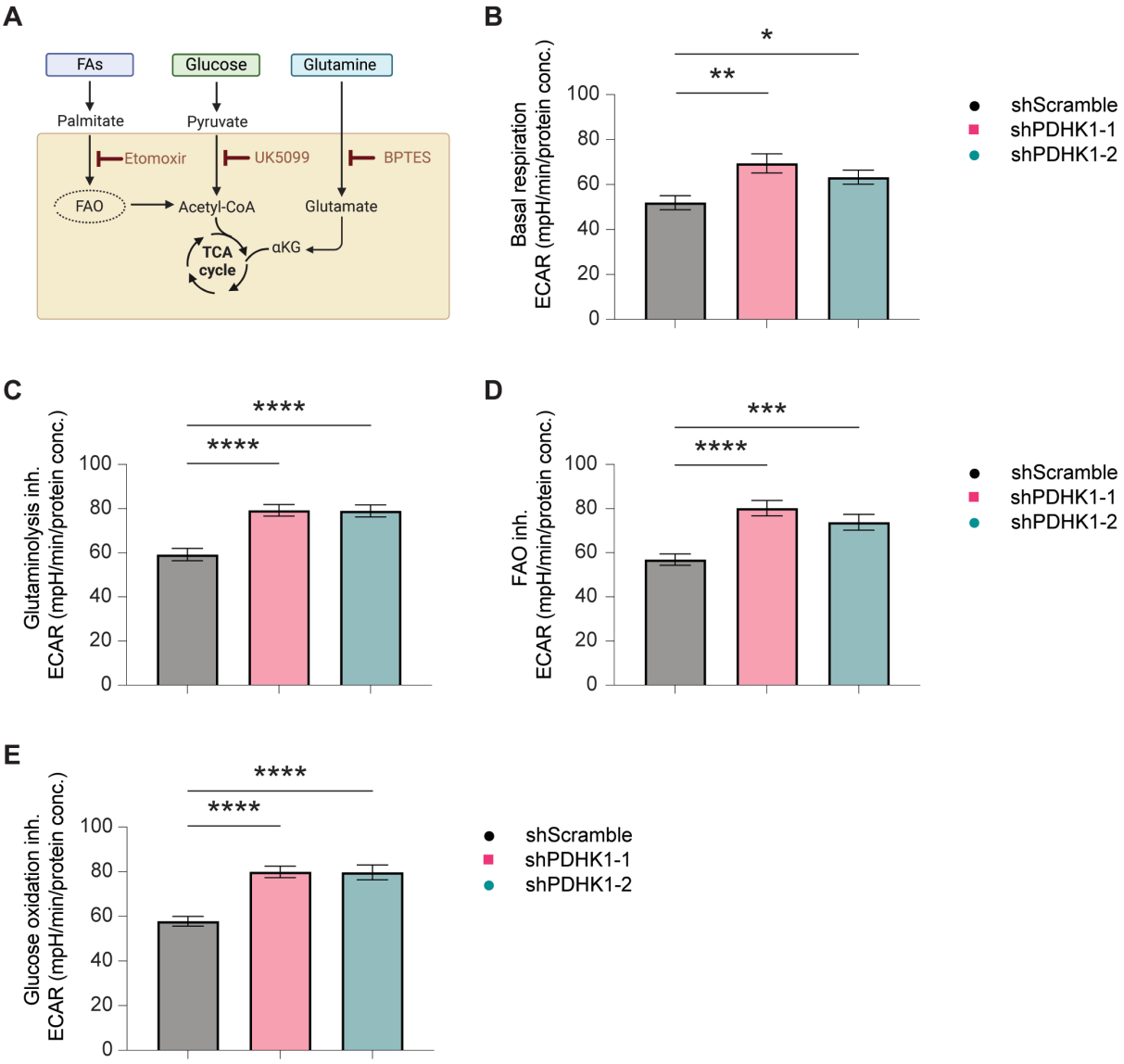

Figure 12. Mitochondrial respiration remains constant upon PDHK1 deficiency.

(A) Schematic of the metabolic pathways and inhibitors used to identify metabolic dependency from Seahorse assays. Mitochondria is depicted in yellow. **(B)** Extracellular acidification rate (ECAR) measured in basal respiration, **(C)** glutaminolysis inhibition, **(D)** FAO inhibition, and **(E)** glucose oxidation inhibition from hypoxia-cultured NIH-3T3 cells expressing short hairpin PDHK1 (shPDHK1 and shPDHK1-2) and scramble RNA (shScramble). Abbreviations: FAO – fatty acid oxidation. Data is represented as individual values ± S.E.M. Significance was defined as follows: *p≤ 0.05; **p≤ 0.01; and ***p≤ 0.001; ****p ≤ 0.001, as assessed by two-way ANOVA.

5.5 Glucose-derived TCA cycle and acetyl-CoA synthesis is restored upon PDHK1 deficiency

Next, we aimed to identify the predominant carbon sources contributing to the acetyl-CoA pool under PDHK1 depletion. Since glucose-derived acetyl-CoA synthesized within mitochondria is considered the predominant source of acetyl-CoA in mammalian cells (Pietrocola et al., 2015), we conducted stable isotope tracing using [$^{13}C_6$]-glucose in PDHK1-KD cells cultured in hypoxia (2% O_2) for 24 h.

We found that [$^{13}C_6$]-glucose uptake and labeling into downstream glycolytic intermediates remained stable or showed minor changes upon PDHK1-KD as compared to control cells (Figure S2A). Glycolysis-derived amino acids showed scarce or undetectable labeling (Figure S2B). Since PDHK1 function is downstream of glycolysis, we reasoned that ^{13}C incorporation into TCA cycle metabolites could be restored upon PDHK1 depletion. In accordance, labeling into most TCA cycle metabolites and derived amino acids was higher in KD cells compared to the control (Figure 13A,B). Similarly, flux into acetyl-CoA increased in PDHK1-depleted cells (Figure 13C). Interestingly, the pool size of acetyl-CoA remained stable upon PDHK1-KD (Figure 13D). We next tested whether PDHK1 depletion affected the pool size of other CoA compounds, and found no differences between KD and control cells (Figure S3A-C). Thus, our data indicate that under PDHK1 depletion, glucose-derived metabolism activates the TCA cycle and its contribution to acetyl-CoA synthesis leaving glycolytic activity and the acetyl-CoA pool size unchanged.

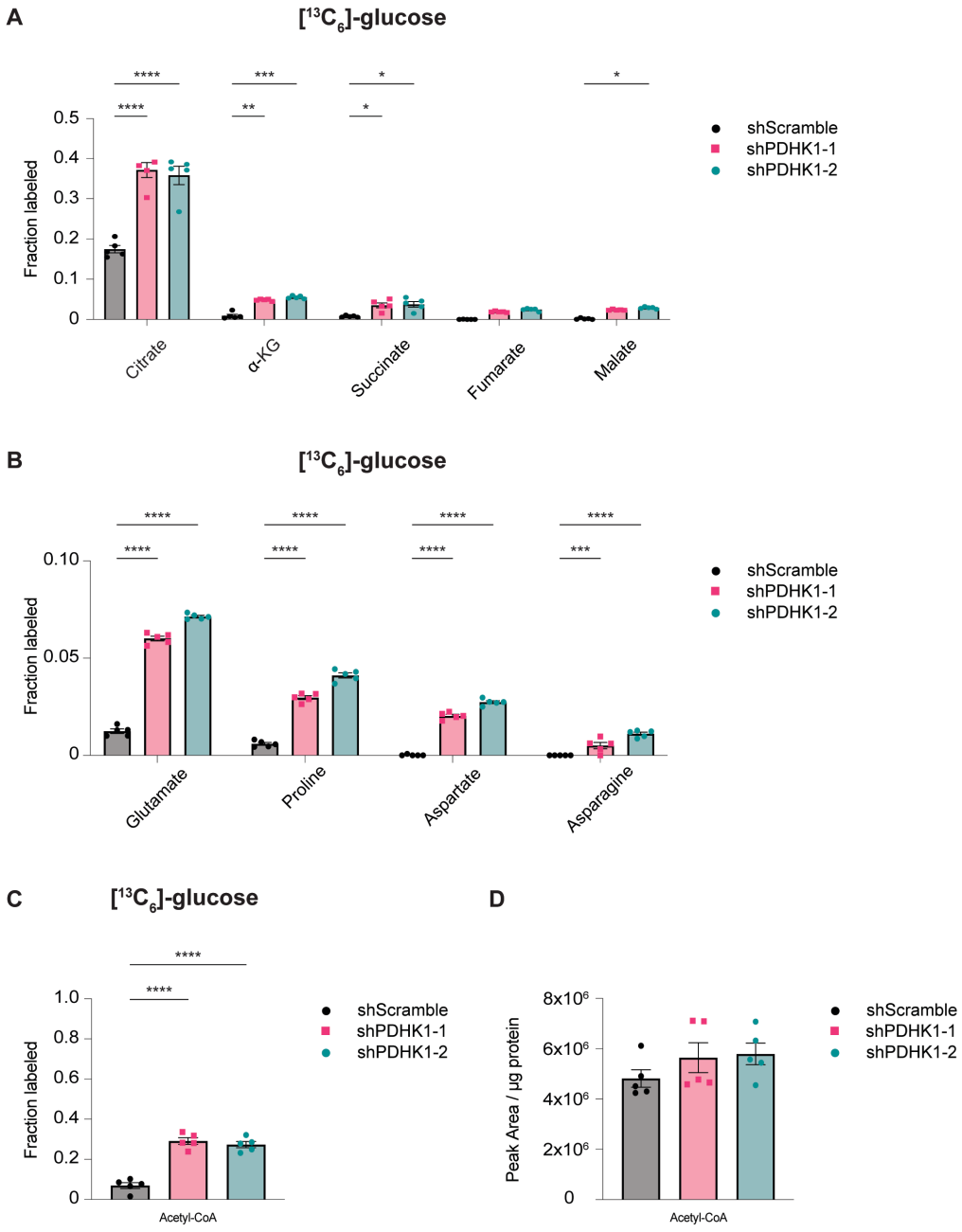

Figure 13. PDHK1 deficiency increases glucose contribution towards TCA cycle and acetyl-CoA synthesis without altering acetyl-CoA pool size.

(A) [$^{13}C_6$]-glucose-derived labeling in TCA cycle metabolites, **(B)** TCA cycle-derived amino acids, and **C)** acetyl-CoA from hypoxia-cultured NIH-3T3 cells expressing short hairpin PDHK1 (shPDHK1 and shPDHK1-2) and scramble RNA (shScramble). **D)** Metabolic pool size of acetyl-CoA. Data is represented as individual values ± S.E.M. Significance was defined as follows: n.s. (not shown abbreviation) > 0.05; *p≤ 0.05; **p≤ 0.01; ***p≤ 0.001; and ****p ≤ 0.001, as assessed by two-way ANOVA. Mass isotopomers represented are: Citrate (m+2), αKG (m+2), Succinate (m+2), Fumarate (m+2), Malate (m+2), Glutamate (m+2), Proline (m+2), Aspartate (m+2), Asparagine (m+2), acetyl-CoA (m+2). (A) Y-max = 0.5; (B) Y-max = 0.10; (C) Y-max = 1.0).

Given that acetyl-CoA can be synthesized from diverse carbon sources other than glucose, we examined the contribution of other metabolites to the acetyl-CoA pool. Since one of the hallmarks of the cellular response to hypoxia is the metabolic rewiring that promotes

glutamine metabolism within mitochondria, we performed metabolite tracing experiments using [$^{13}C_5$]-glutamine (Figure 14).

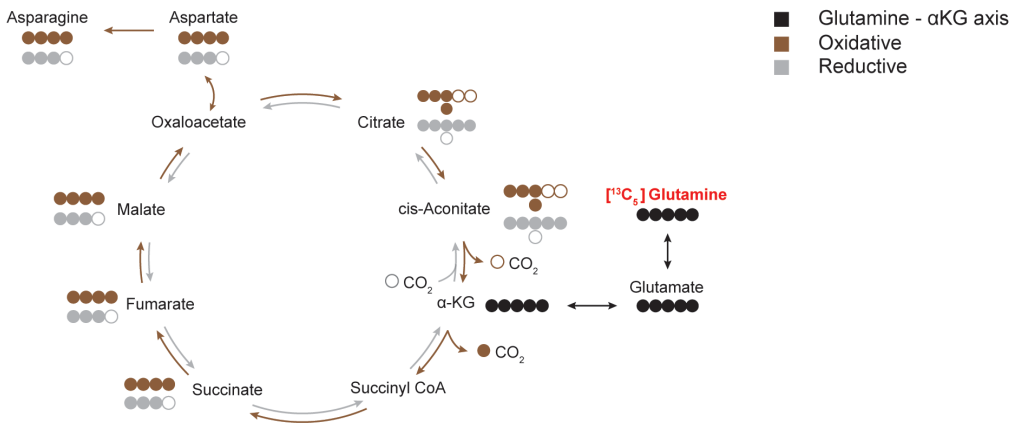

Figure 14. Isotope tracing model of glutamine labeling into the TCA cycle.

Schematic depicting the ^{13}C-labeling pattern derived from [$^{13}C_5$]-glutamine metabolism in the TCA cycle. Empty circles represent ^{12}C-atoms, and filled circles represent ^{13}C-atoms. Black circles represent mass isotopomers produced by the glutamine – αKG axis. Brown circles represent mass isotopomers produced by oxidative metabolism and grey circles represent mass isotopomers produced by reductive metabolism. The ^{13}C-labeling pattern represents one round of the TCA cycle.

We first analyzed the ^{13}C incorporation of [$^{13}C_5$]-glutamine into the glutamine - αKG axis, and observed a similar uptake in KD cells compared to the control (Figure 15). Interestingly, in the following enzymatic steps where glutamine is converted to glutamate and αKG, PDHK1-depleted cells showed lower labeling compared to the control. As αKG represents the entry point of glutamine-derived metabolites into the TCA cycle, our results suggest that glutamine-derived fueling into the TCA cycle diminishes upon PDHK1-KD.

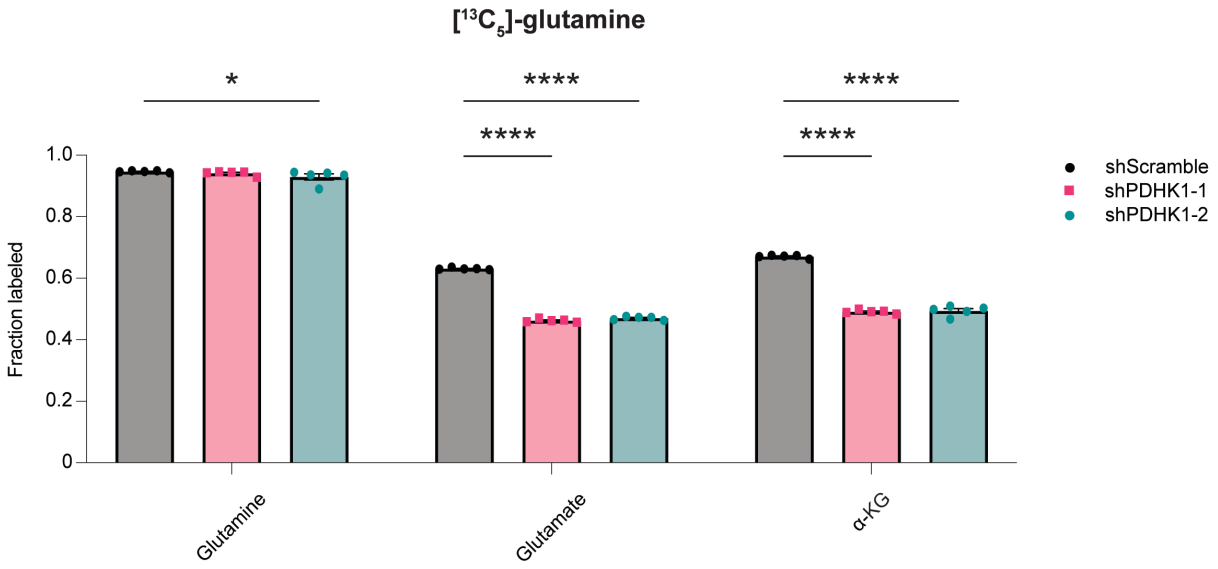

Figure 15. PDHK1 deficiency decreases glutamine conversion into glutamate and αKG.

[$^{13}C_5$]-glutamine-derived labeling in the glutamine - αKG axis from hypoxia-cultured NIH-3T3 cells expressing short hairpin PDHK1 (shPDHK1 and shPDHK1-2) and scramble RNA (shScramble). Data is represented as individual values ± S.E.M. Significance was defined as follows: n.s. (not shown abbreviation) > 0.05; *p≤ 0.05; and ****p ≤ 0.001, as assessed by two-way ANOVA. Mass isotopomers represented are: glutamine (m+5), glutamate (m+5), and αKG (m+5).

αKG fuels the TCA cycle following oxidative glutaminolysis or reductive carboxylation (Sun & Denko, 2014). Since the predominance of either pathway has been shown to be context-specific, we examined the labeling that occurred in both directions. Oxidative metabolism showed lower ^{13}C incorporation into most metabolites and derived amino acids in KD cells compared to the control (Figure 16A,B). On the contrary, labeling into the reductive direction remained stable for most metabolites and amino acids upon PDHK1 depletion (Figure 17A,B). Next, we analyzed the incorporation of glutamine-derived carbons into acetyl-CoA, and observed a lower contribution in PDHK1-depleted cells compared to the control (Figure 17C). Hence, these data indicate that PDHK1 depletion rewires glutamine metabolism by decreasing the carbon supply of the oxidative pathway and acetyl-CoA synthesis, leaving reductive metabolism mostly unaffected.

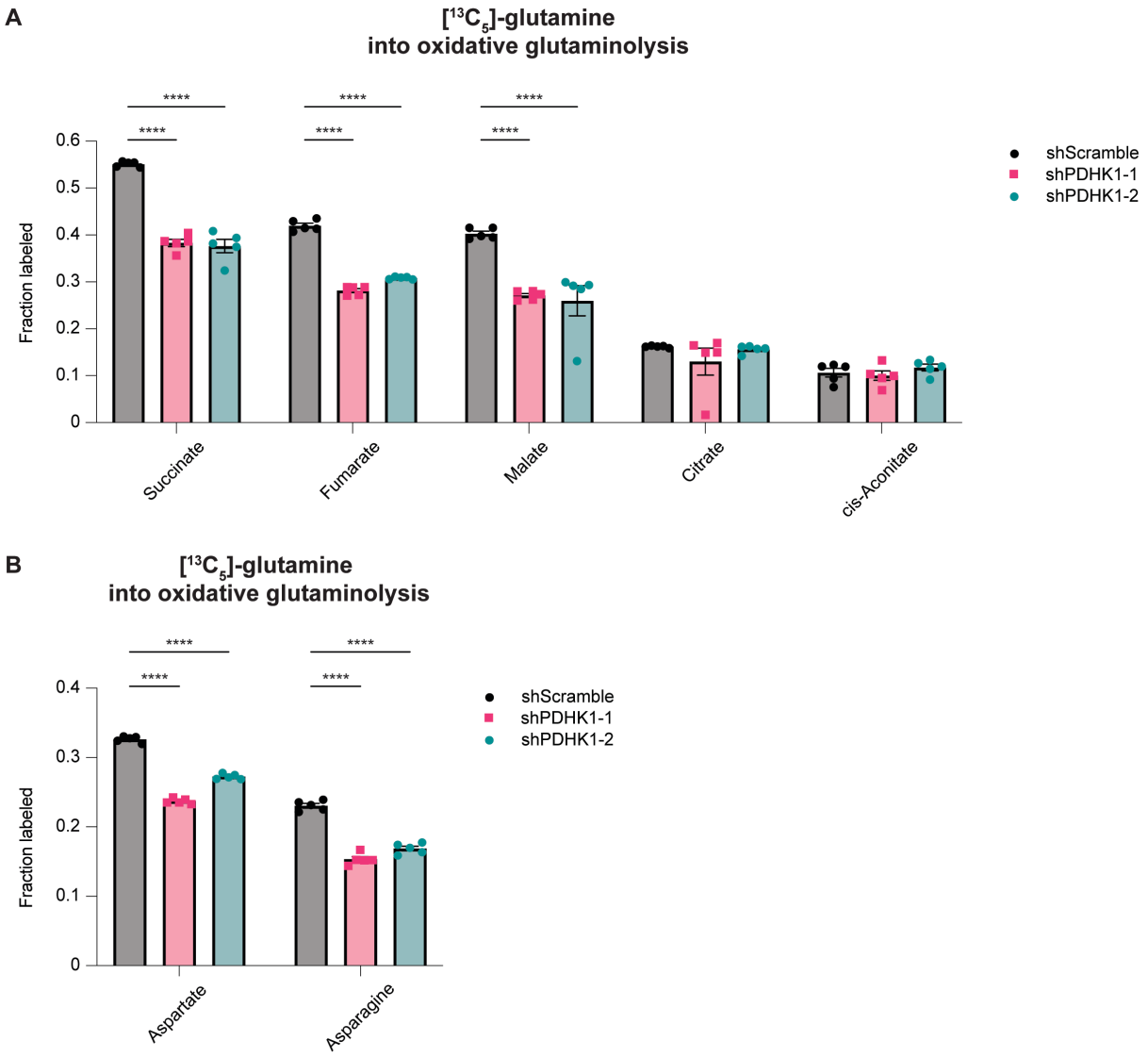

Figure 16. Oxidative glutaminolysis is downregulated upon PDHK1 deficiency.

(A) [$^{13}C_5$]-glutamine-derived labeling in the oxidative glutamine pathway of TCA cycle metabolites and, **(B)** TCA cycle-derived amino acids from hypoxia-cultured NIH-3T3 cells expressing short hairpin PDHK1 (shPDHK1 and shPDHK1-2) and scramble RNA (shScramble). Data is represented as individual values ± S.E.M. Significance was defined as follows: n.s. (not shown abbreviation) > 0.05; and ****p ≤ 0.001, as assessed by two-way ANOVA. Mass isotopomers represented are: succinate (m+4), fumarate (m+4), malate (m+4), citrate (m+4), cis-Aconitate (m+4), aspartic acid (m+4), asparagine (m+4).

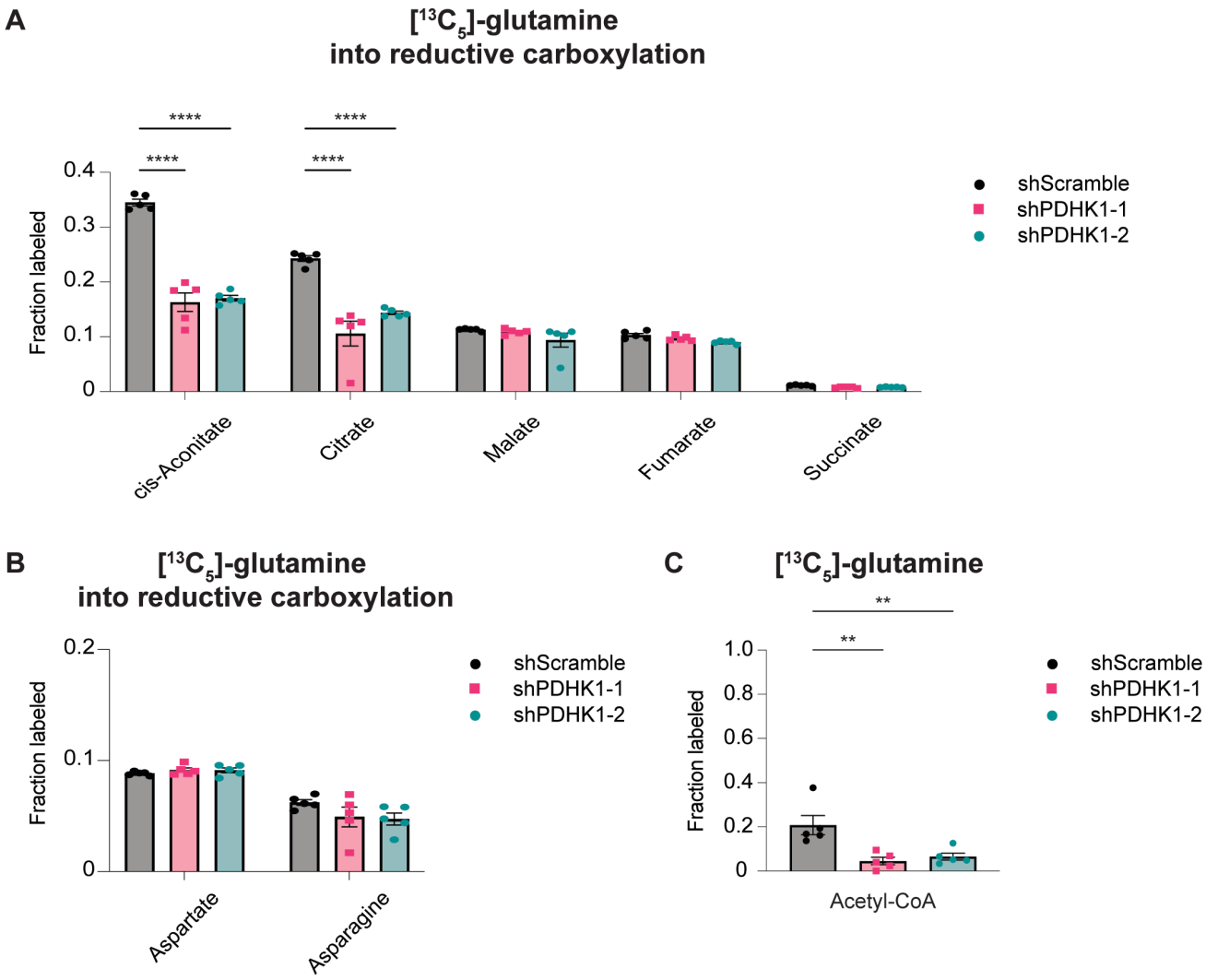

Figure 17. PDHK1 depletion has no impact on glutamine reductive carboxylation but downregulates glutamine contribution to acetyl-CoA synthesis.

(A) [$^{13}C_5$]-glutamine-derived labeling in the reductive glutamine pathway of TCA cycle metabolites, **(B)** TCA cycle-derived amino acids, and **(C)** acetyl-CoA from hypoxia-cultured NIH-3T3 cells expressing short hairpin PDHK1 (shPDHK1 and shPDHK1-2) and scramble RNA (shScramble). Data is represented as individual values ± S.E.M. Significance was defined as follows: n.s. (not shown abbreviation) > 0.05; **p≤ 0.01; and ****p ≤ 0.001, as assessed by two-way ANOVA. Mass isotopomers represented are: cis-Aconitate (m+5), citrate (m+5), malate (m+3), fumarate (m+3), succinate (m+3), aspartate (m+3), asparagine (m+3), acetyl-CoA (m+2).

5.6 PDHK1 depletion decreases H3K27ac levels

Our observations on the metabolic profile of PDHK1-depleted cells indicated that rather than modifying the acetyl-CoA pool size, PDHK1 depletion increased the contribution of glucose as a carbon source for acetyl-CoA synthesis. To investigate whether this metabolic rewiring affected histone acetylation and transcriptional-related histone PTMs, we measured levels of

H3ac and H3K27ac by immunofluorescence (Figure 18A,B). Given that glucose is considered the main carbon source of acetyl-CoA, we hypothesized that H3ac and H3K27ac could be enriched upon PDHK1-KD in hypoxic conditions. Interestingly, levels of H3ac showed minor changes in KD cells compared to control, while H3K27ac enrichment decreased upon PDHK1-KD. Thus, our results suggest that under hypoxic conditions, PDHK1 KD impacts levels of H3K27ac rather than altering the global histone acetylation scale. Hence, PDHK1 depletion might contribute to chromatin compaction and lower transcriptional activity as means of decreased H3K27ac enrichment. In addition, as we observed unchanged levels of H3ac but lower H3K27ac, we hypothesized the surplus of glucose-derived acetyl-CoA might be oriented towards mechanisms other than histone acetylation.

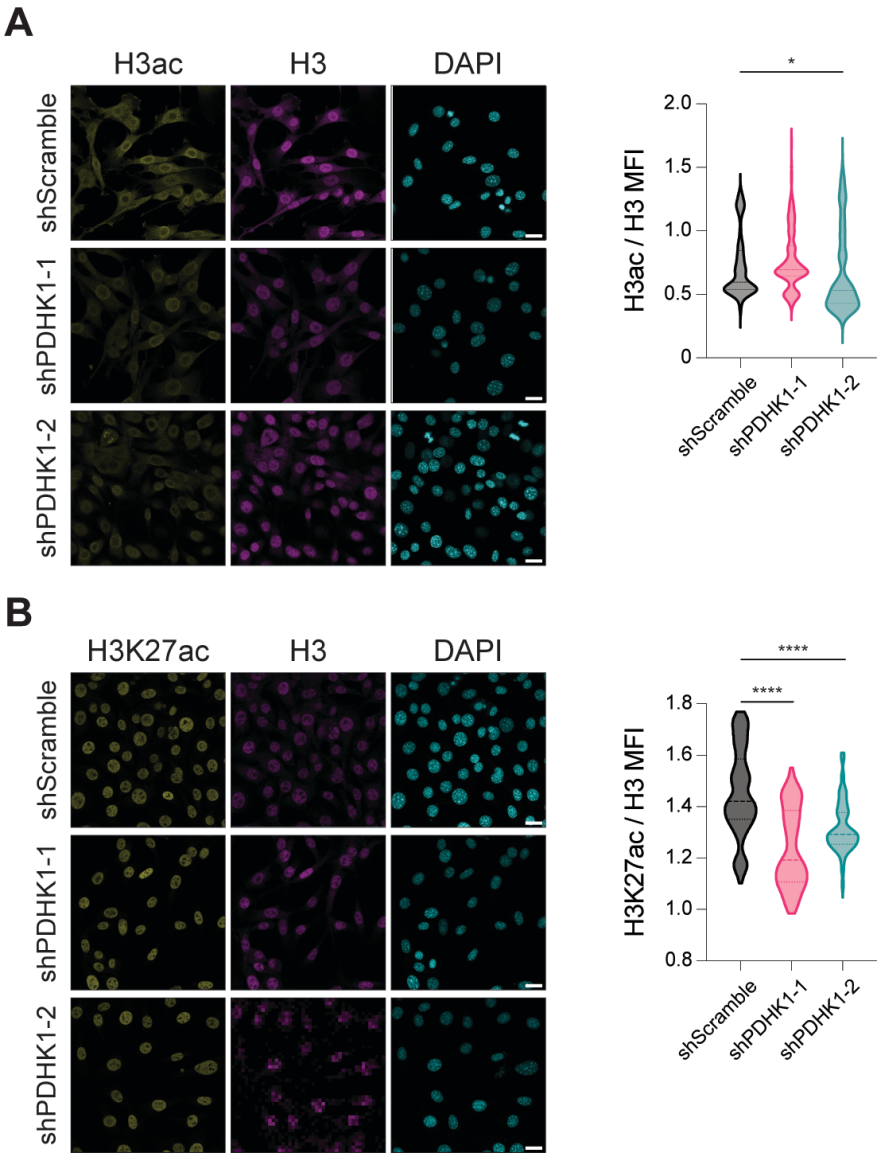

Figure 18. H3K27ac is downregulated in PDHK1-KD cells.

(A) Representative immunofluorescence images and quantification of H3ac (yellow), and **(B)** H3K27ac (yellow), H3 (magenta), and nuclear (DAPI, cyan) from hypoxia-cultured NIH-3T3 cells expressing short hairpin PDHK1 (shPDHK1 and shPDHK1-2) and scramble RNA (shScramble). H3 was used as internal control for H3ac and H3K27ac signal normalization. Data is represented as individual values ± S.E.M. Significance was defined as follows: n.s. (not shown abbreviation) > 0.05; *p≤ 0.05; ****p ≤ 0.001, as assessed by one-way ANOVA. Scale bar 20 µm.

5.7 PDHK1 initiates a fatty-acid synthesis protein program facilitated by malonyl-CoA pool size upregulation

To identify pathways implicated in acetyl-CoA catabolism, we conducted whole-cell protein quantification in hypoxia-cultured PDHK1-KD cells. We identified 268 overlapping DE proteins between KD cells, with 155 proteins commonly upregulated and 113 downregulated compared to the control (Figure 19A). We then conducted a GO analysis on BP to the DE proteins, and found FA metabolism as highly enriched (Figure 19B). Acetyl-CoA is an essential intermediate for *de novo* FA synthesis (Batchuluun et al., 2022). Since *de novo* FA synthesis is a dynamic process that responds to metabolic demands and environmental cues (Batchuluun et al., 2022), we reasoned that acetyl-CoA might be redirected from histones towards FAs upon PDHK1 depletion in hypoxia.

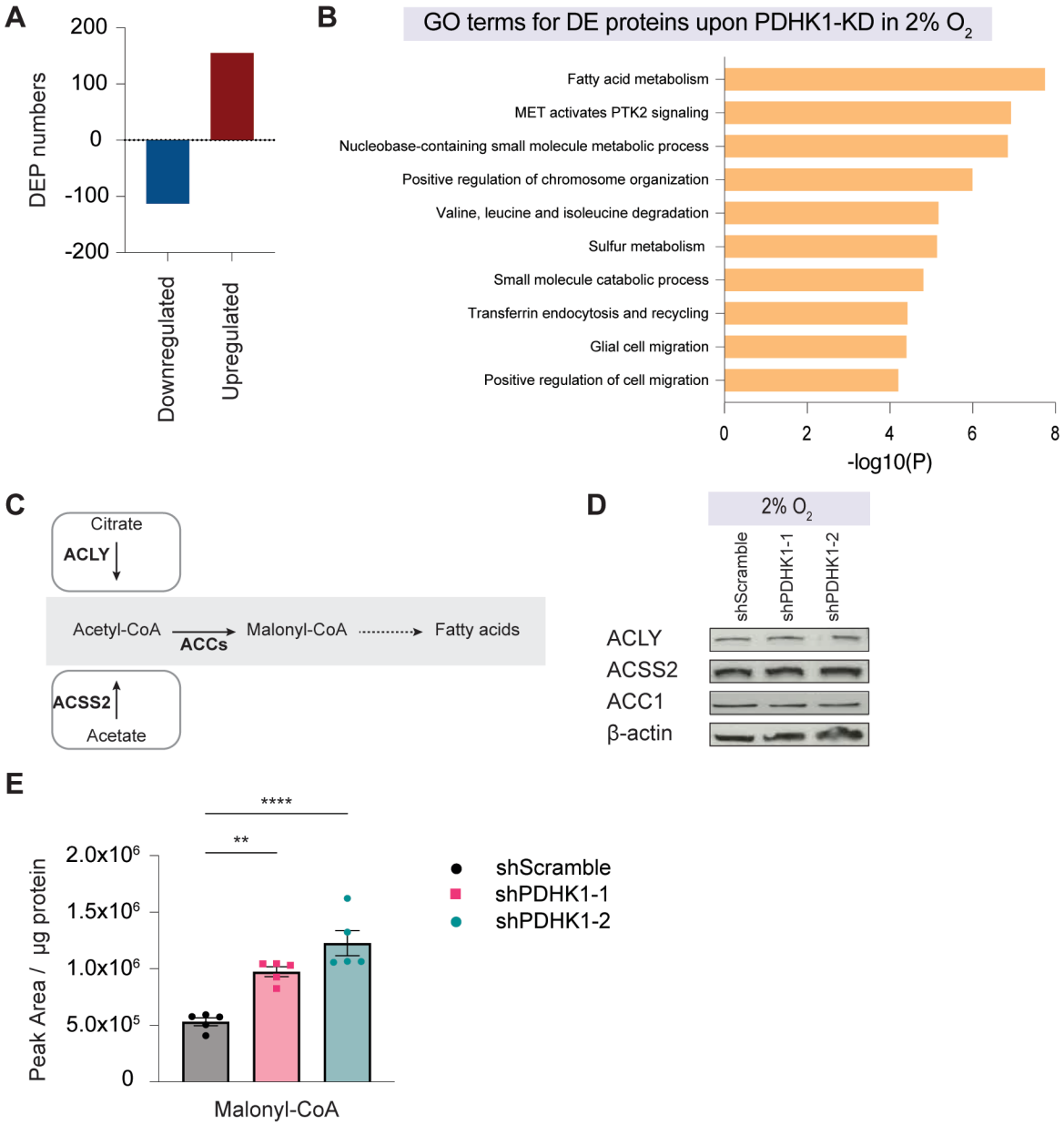

Figure 19. PDHK1 depletion initiates a lipid-specific protein program and increases malonyl-CoA pool size.

(A) Number of differentially expressed proteins (DEP) detected in PDHK1-depleted cells compared to control cells. **(B)** Gene Ontology (GO) term analysis for biological processes (BP) of differentially expressed (DE) proteins in PDHK1-depleted cells. **(C)** Schematic of the initial steps of de novo fatty-acid synthesis, and **(D)** representative immunoblotting of key enzymes. β-ACTIN is used as protein loading control. **(E)** Malonyl-CoA pool size quantification of hypoxia-cultured NIH-3T3 cells expressing short hairpin PDHK1 (shPDHK1 and shPDHK1-2) and scramble RNA (shScramble). Data is represented as individual values ± S.E.M. Significance was defined as follows: **p≤ 0.01; and ****p ≤ 0.001, as assessed by two-way ANOVA.

5.8 Glucose contribution to lipid synthesis increases upon PDHK1 depletion

We next aimed to further investigate the hypothesis that PDHK1 depletion redistributes acetyl-CoA towards FA synthesis. Since the first committed step of lipogenesis involves the conversion of cytosolic acetyl-CoA to malonyl-CoA (Figure 19C), we evaluated levels of cytosolic acetyl-CoA and malonyl-CoA synthetases by immunoblotting (Figure 19D). Interestingly, we observed similar expression levels between KD cells and control. We next measured the metabolic pool size of malonyl-CoA (Figure 19E), and observed higher levels of malonyl-CoA in KD cells compared to the control. Thus, confirming our hypothesis of FA synthesis upregulation upon PDHK1 depletion in hypoxia.

We then tested whether glucose was used to supply the observed lipogenesis. For this, we again used metabolic labeling with [$^{13}C_6$]-glucose in hypoxia-cultured KD cells. We harvested lipids at 8 h after the switch to tracer media, and observed that glucose contribution to PC (34:1), CoQ9, Sm (36:1), and TG (48:0) increased upon PDHK1 depletion compared to the control (Figure 20A,B). Thus, our data indicate that lipid biosynthesis is supported by glucose upon PDHK1 depletion in hypoxia.

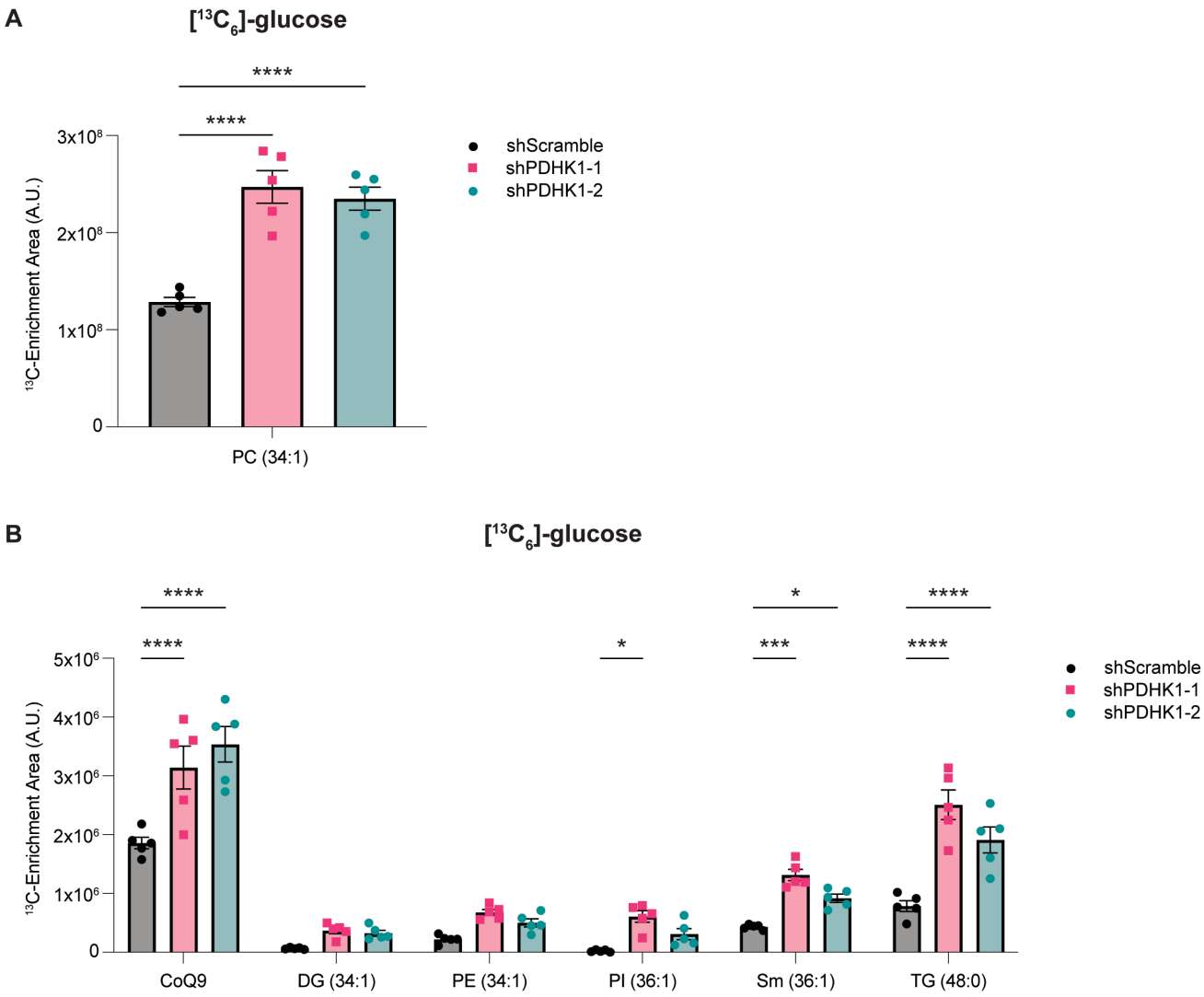

Figure 20. Glucose contribution to lipid synthesis increases upon PDHK1 depletion.

A) [$^{13}C_6$]-glucose-derived labeling in PC, and **(B)** representative lipid species compounds from hypoxia-cultured NIH-3T3 cells expressing short hairpin PDHK1 (shPDHK1 and shPDHK1-2) and scramble RNA (shScramble). Data is represented as individual values ± S.E.M. Significance was defined as follows: n.s. (not shown abbreviation) > 0.05; *p≤ 0.05; ***p≤ 0.001; and ****p ≤ 0.001, as assessed by two-way ANOVA. (A) Y-max = 3x10^8; (B) Y-max = 5x10^6.

Given that FAs can also be synthesized from pathways related to amino acid metabolism, we examined glutamine contribution to lipogenesis using [$^{13}C_5$]-glutamine. In contrast to our observations on glucose carbon supply, we observed minor differences for most lipids species between KD and control cells (Figure 21A,B). Only glutamine flux into CoQ9 decreased upon PDHK1 depletion. Thus, our results showed that glutamine contribution to FA synthesis remained stable upon PDHK1-KD.

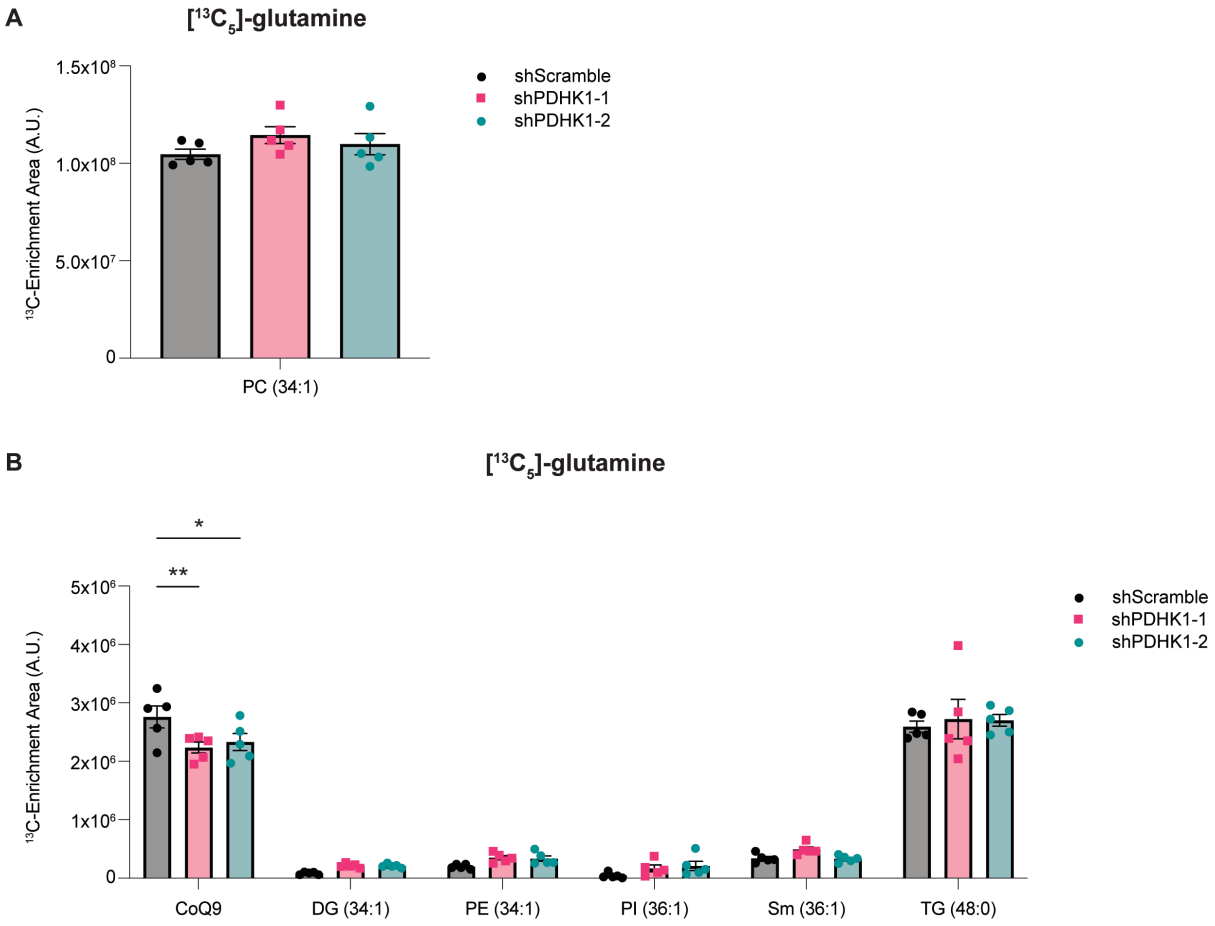

Figure 21. Glutamine contribution to lipid synthesis remains constant upon PDHK1 deficiency.

A) [$^{13}C_5$]-glutamine-derived labeling in PC, and **(B)** representative lipid species compounds from hypoxia-cultured NIH-3T3 cells expressing short hairpin PDHK1 (shPDHK1 and shPDHK1-2) and scramble RNA (shScramble). Data is represented as individual values ± S.E.M. Significance was defined as follows: n.s. (not shown abbreviation) > 0.05; *p≤ 0.05; **p≤ 0.01, as assessed by two-way ANOVA. (A) Y-max = 1.5x10^8; (B) Y-max = 5x10^6.

5.9 ACC1 inhibition restores H3K27ac levels upon PDHK1 deficiency

We further investigated the molecular mechanisms that might account for PDHK1-dependent acetyl-CoA redistribution from histone acetylation towards FA synthesis. For this, we inhibited FA synthesis treating hypoxia-cultured KD cells with CP-640186 hydrochloride for 48 h (Harwood et al., 2003). This pharmacological compound inhibits ACC1 and ACC2, the key enzymes that initiate FA synthesis by generating malonyl-CoA from acetyl-CoA (Figure 22A) (Harwood et al., 2003; Wang et al., 2022). We first characterized the expression of the active, non-phosphorylated, form of ACC1 (Brownsey et al., 2006; Harwood et al., 2003), and noted the CP-treatment selectively increased levels of ACC1 upon PDHK1 depletion (Figure 22B).

We then evaluated levels of phosphorylated (Ser79) ACC1, the inactive form of the enzyme, by immunoblotting (Figure 22B) (Brownsey et al., 2006; Fullerton et al., 2013). Interestingly, we observed the CP-treatment had no impact on phosphorylated ACC1 (P-ACC1) in KD cells compared to control. Taken together, our data suggest that ACC1 inhibition might elicit a positive-feedback loop on ACC1 expression to further upregulate FA synthesis upon PDHK1 depletion.

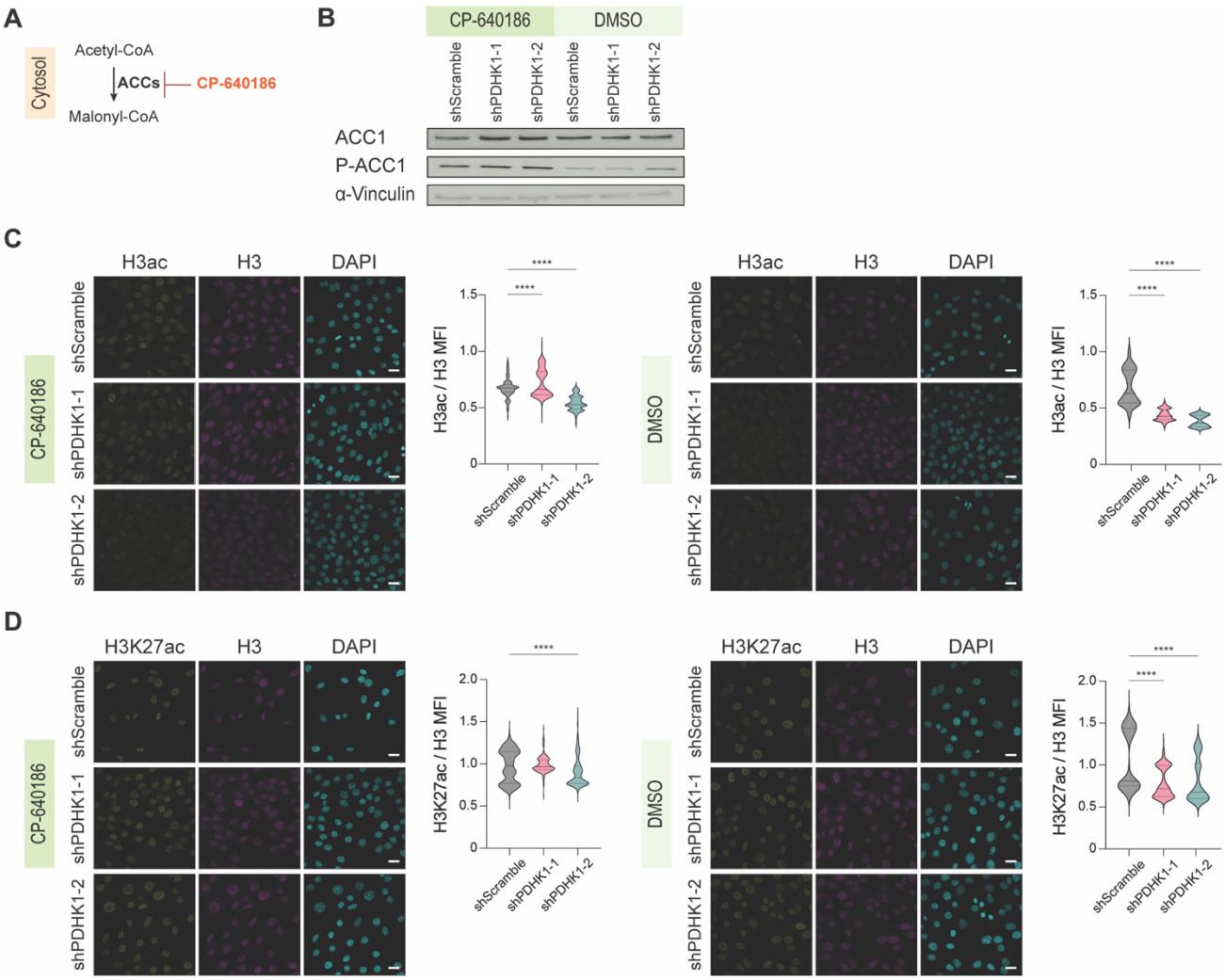

Figure 22. ACC1 inhibition restores H3K27ac levels in PDHK1-KD cells.

(A) Schematic of ACCs inhibition by CP-640186. **(B)** Representative immunoblots depicting the endogenous phospho-ACC1 (P-ACC1), ACC1 and α-Vinculin protein levels in hypoxia-cultured NIH-3T3 cells expressing short hairpin PDHK1 (shPDHK1 and shPDHK1-2) and scramble RNA (shScramble). **(C)** Representative immunofluorescence images and quantification of H3ac (yellow), and **(D)** H3K27ac (yellow), H3 (magenta), and nuclear (DAPI, cyan) from CP-treated hypoxia-cultured NIH-3T3 cells expressing short hairpin PDHK1 (shPDHK1 and shPDHK1-2) and scramble RNA (shScramble). H3 was used as internal control for H3ac and H3K27ac signal normalization. DMSO-cultured cells were used as treatment control. Data is represented as individual values ± S.E.M. Significance was defined as follows: n.s. (not shown abbreviation) > 0.05, and ****p ≤ 0.001, as assessed by one-way ANOVA. Scale bar 20 μm.

To finally test whether FA synthesis and histone acetylation compete for the nuclear-cytosolic acetyl-CoA pool in a PDHK1-dependent manner in hypoxia, we measured H3ac and H3K27ac enrichment in CP-treated cells (Figure 22C,D). On the one hand, we observed the CP-treatment had no impact on H3ac levels in comparison with our control treatment. On the other hand, we found that CP-640186 supplementation increased H3K27ac enrichment in shPDHK1-1 cells compared to the control treatment. Thus, H3K27ac levels are reconstituted upon FA synthesis inhibition in PDHK1 depleted cells, further confirming the role of PDHK1 in acetyl-CoA usage redistribution from histone acetylation to FAs.

Although several studies had shown that FAs can become the major acetyl-CoA depot over histone acetylation, little was known about the role of PDHK1 within this mechanism. Thus, our data provided one of the first lines of evidence that PDHK1 depletion elicits a redistribution response of acetyl-CoA from histone acetylation towards FA synthesis in hypoxia (Figure 23A,B).

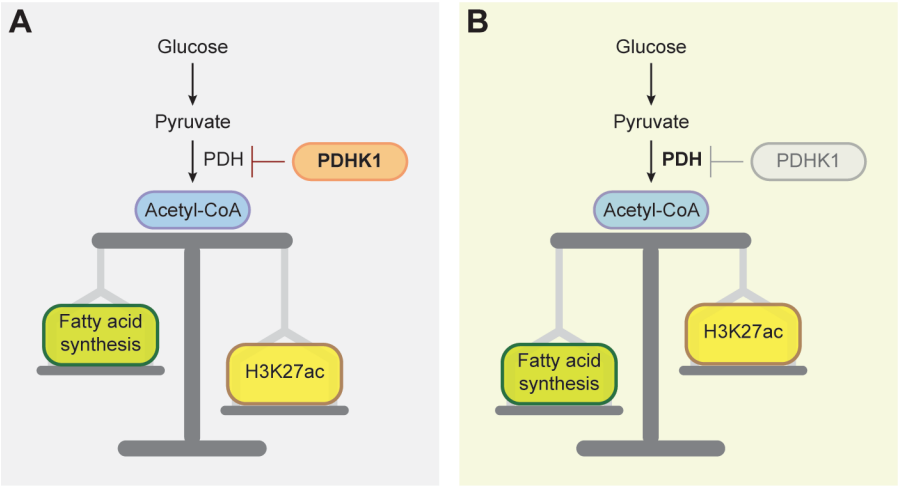

Figure 23. Model for PDHK1-dependent distribution of acetyl-CoA between FAs and H3K27ac

(A) In hypoxia, PDHK1 upregulation inhibits PDH function, thereby hindering pyruvate-derived acetyl-CoA synthesis in mitochondria. In this context, H3K27ac is upregulated and fatty-acid synthesis remains unaffected. **(B)** In hypoxia, PDHK1 depletion permits PDH function, thereby facilitating pyruvate-derived acetyl-CoA synthesis in mitochondria. Upon PDHK1 deficiency, H3K27ac levels are downregulated while fatty-acid synthesis increased.

To assess whether PDHK1 depletion exerted a transcriptomic response, we performed RNA-sequencing in hypoxia-cultured KD cells. Interestingly, we observed a mild transcriptomic response characterized by having a reduced number of upregulated and downregulated

genes (Figure S4). No statistical test nor functional allocation analysis was performed on this small dataset. Thus, our data suggest the transcriptome remained stable upon PDHK1 depletion in hypoxia.

5.10 PDH subcellular location remains stable upon PDHK1 depletion

Recent studies have shown that the PDH complex can be translocated from mitochondria to the nucleus, where acetyl-CoA can be directly synthesized from pyruvate (Sutendra et al., 2014). Since this pathway provides a new route for nuclear acetyl-CoA synthesis that can impact the nuclear-cytosolic acetyl-CoA pool size, we next tested whether PDHK1 depletion impact PDH subcellular location in hypoxia (Figure 24A). We first evaluated active PDH (PDH) expression and noted its presence only in the cytosolic fraction, with similar levels between KD and control cells. Next, we assessed the levels of phosphorylated PDH (P-PDH), the inactive form of PDH. We hypothesized that P-PDH expression would decrease upon PDHK1 depletion. However, our results showed that mitochondrial P-PDH remains stable in KD cells compared to control. Interestingly, we observed that cytosolic P-PDH is upregulated in PDHK1-depleted cells.

Taken together, our data indicate that in hypoxia, PDHK1 depletion impacts cytosolic PDH's function rather than altering its mitochondrial/cytosolic subcellular location. First, in our model, PDH was mainly cytosolic and not mitochondrial for KD and control cells. Given that cytosolic PDH remained stable upon PDHK1 depletion, we consider that PDHK1 KD did not alter PDH's subcellular location. Second, P-PDH was detected in the mitochondria and cytosol of KD and control cells (Figure 24B). However, in contrast to our hypothesis, PDHK1-KD did not alter P-PDH enrichment in mitochondria but in the cytosol. Thus, PDHK1-KD in hypoxia upregulates the inhibition of cytosolic PDH. Different compensatory mechanisms might be accountable for these observations and should be further tested. For instance, functional assays of the other pyruvate dehydrogenase kinases (PDHK2-4) or phosphatases (PDP1-2). Furthermore, since we used a KD rather than a knockout (KO) approach, non-silenced PDHK1 mRNA might still be functional and phosphorylate PDH. Thus, using a PDHK1 KO would contribute to examine further the impact of PDHK1 absence in PDH subcellular location and functional status.

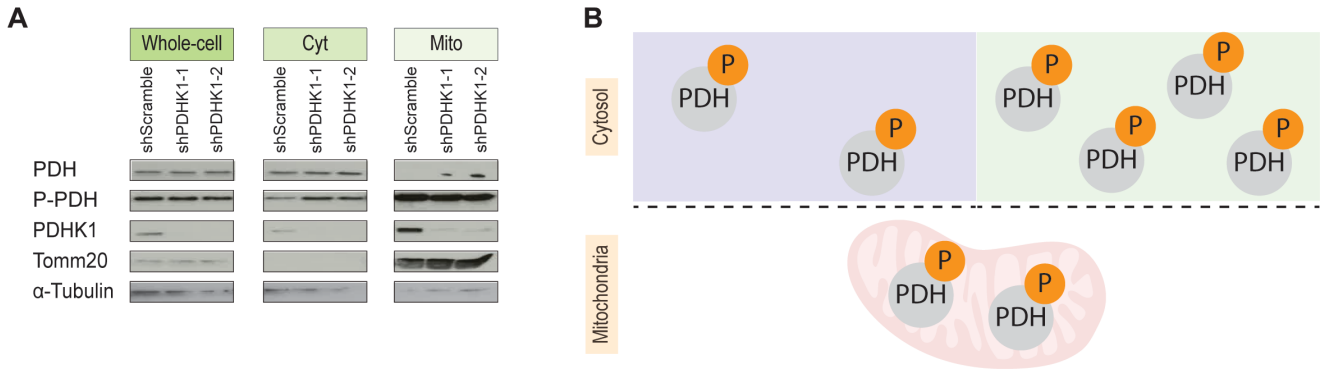

Figure 24. PDH subcellular location remains constant in PDHK1-KD cells.

(A) Representative immunoblots depicting the endogenous phospho-PDH (P-PDH), PDH, PDHK1, Tomm20 and, α-Tubulin from subcellular fractions of hypoxia-cultured NIH-3T3 cells expressing short hairpin PDHK1 (shPDHK1 and shPDHK1-2) and scramble RNA (shScramble). **(B)** Schematic of P-PDH location in mitochondrial and cytosolic fractions of control (purple) and KD cells (green).

6 DISCUSSION

The coordination of chromatin and metabolism plays a central role in cellular homeostasis and the adaptative response to the environment (Lee et al., 2014; Peng et al., 2016). Here we study how hypoxia impact the interplay between chromatin modifications and intracellular metabolite cycling. Using a multi-omics approach, we found that deficiency of the HIF1α-target PDHK1 - a well-known inhibitor of acetyl-CoA synthesis in mitochondria - rewires use of glucose-derived acetyl-CoA to enhance FA synthesis and diminish histone acetylation. This occurs via a coordinated lipid-specific proteomic response deprived of a transcriptomic signature. Taken together, our data identify a new role for PDHK1 in the regulation of acetyl-CoA metabolism and provides further evidence for a close link between histone acetylation and lipid biogenesis.

The development of this research project was conducted in two successive phases that will be discussed accordingly. First, we performed a comprehensive screening of the cellular response to hypoxia that allowed us to understand the impact of low oxygen conditions at metabolic, proteomic, and transcriptomic level in our model and culture conditions. This screening allowed us to observe an unexpected response related to acetyl-CoA metabolism and identify PDHK1 as a potential candidate accountable for this shift. As a result, in the second phase of the project, we analyzed the hypoxia response in the absence of PDHK1, focusing on acetyl-CoA metabolism and its connection to downstream processes.

Characterizing the cellular response to hypoxia using an "omics" approach to identify a metabolic signature and chromatin response.

Several studies have reported the impact of hypoxia in cellular metabolism (Batie et al., 2019; Dengler et al., 2014; Sun & Denko, 2014; Wheaton & Chandel, 2011). With key molecular players of the hypoxia response being continuously identified, the general model of hypoxia metabolism has been vastly refined. Nevertheless, these new findings have also showed the flexibility in the hypoxia response and have opened new perspectives on how metabolic pathways adjust their activities to low oxygen conditions (Kocianova et al., 2022; Vaupel & Multhoff, 2021). For example, the canonical response to hypoxia described as the "Warburg effect", characterized by aerobic glycolysis activation and TCA cycle downregulation, was considered the signature of the adaptation to acute hypoxia (Vander Heiden et al., 2009). However, our isotope tracing data showed a stable glycolysis and lower TCA cycle activity after 24 h exposure to hypoxic conditions. Thus, our results support the idea that aerobic glycolysis activation and TCA cycle downregulation can function as uncoupled mechanisms that respond to hypoxic conditions at a different pace.

A reduced TCA cycle activity is normally associated with decreased levels of acetyl-CoA. However, our data identify lower synthesis of glucose-derived citrate and a higher acetyl-CoA pool size. Different mechanisms associated with acetyl-CoA synthesis could explain these intriguing results. If we consider previous studies on ACLY and ACCS2 expression modulation (Zhao et al., 2016), where the genetic deletion of ACLY elicits the upregulation and enzymatic activity of ACSS2, a plausible explanation for our contradicting observations of low citrate but high acetyl-CoA would be ACLY upregulation. Nevertheless, our results showed no impact on ACLY expression upon exposure to hypoxia. Therefore, another possible explanation pointed towards upregulation of mitochondrial acetyl-CoA metabolism. However, we found stable levels of PDH and upregulated expression of its inhibitor PDHK1. The absence of changes in the expression of the canonical acetyl-CoA synthetases in our observations suggests that other processes could be involved and remained to be elucidated.

Levels of acetyl-CoA are intricately associated with histone acetylation (Dai et al., 2020). Although the metabolic pathways for acetyl-CoA synthesis and downstream processes are diverse (Pietrocola et al., 2015), several studies have shown that levels of acetyl-CoA and

histone acetylation are reciprocal (Cai et al., 2011; Lee et al., 2014). However, emerging evidence suggest otherwise and highlights the impact of downstream acetyl-CoA metabolism (i.e., intracellular transport) in histone acetylation levels (Izzo et al., 2023; Pouikli et al., 2021). For instance, a decline in acetyl-CoA synthesis have been reported to do not impact global histone acetylation in a model of ACLY deficiency (Zhao et al., 2016). Also, an impaired export of citrate from mitochondria to the cytosol caused histone hypoacetylation in a murine mesenchymal stem cell model (Pouikli et al., 2021). Our data shows that hypoxia increases levels of acetyl-CoA and H3K27ac. Thus, in our system and culture conditions acetyl-CoA and H3K27ac respond as coupled mechanisms. Investigating the effect of hypoxia in a larger number of histone acetylation PTMs would contribute to further understand the link between acetyl-CoA and histone acetylation levels.

Overall, the multi-omics data presented here suggest a differential adaptive response to hypoxia at metabolic, proteomic and transcriptome level (Figure 25). On the one hand, the metabolome remained mostly stable and showed most differences in TCA cycle downregulation. The proteome indicated a more comprehensive rewiring characterized by a higher expression of glycolytic-enzymes and lower expression of the TCA-cycle ones. On the other hand, the transcriptome revealed an unexpectedly mild response to hypoxia with a clear reconfiguration towards aerobic glycolysis upregulation and no TCA cycle remodeling signature. Considering that we only observed the canonical “Warburg effect” features at proteomic level, suggests that hypoxia impact these regulatory layers differently, and open new possibilities to identify more than one hypoxic phenotype (Kocianova et al., 2022; Vaupel & Multhoff, 2021). Investigating the mechanisms behind those regulatory differences and asking how can they be interconnected using different cell lines, organismal models and oxygen concentrations would contribute to further elucidate the diversity in the hypoxia response.

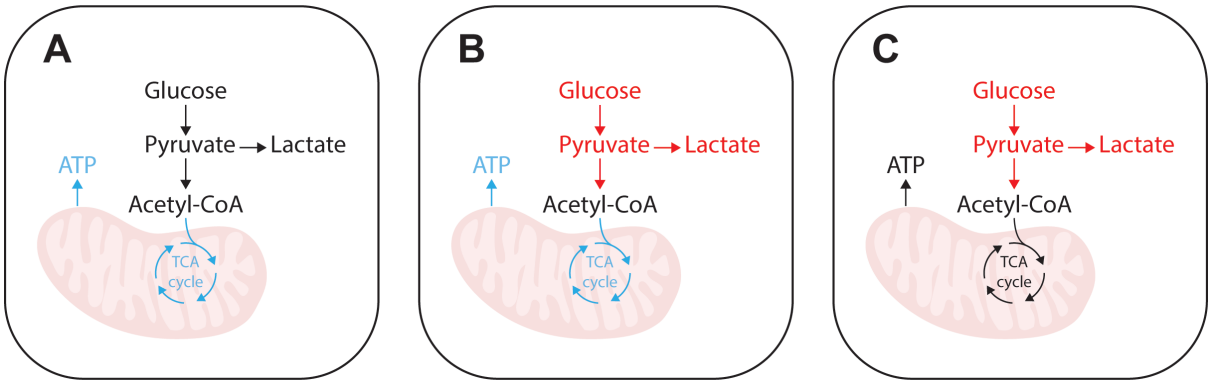

Figure 25. Cellular regulatory layers show a differential response to hypoxia.

(A) Schematic representation of the hypoxia response detected at metabolic, **(B)** proteomic, and (**C)** transcriptomic level. Upregulated and downregulated metabolites are colored red and blue, respectively. Metabolites with no change in hypoxia are colored black.

Investigating the hypoxic cellular response upon PDHK1 depletion as a potential link of chromatin and metabolism.

Regulation of the metabolic transition from glycolysis to the TCA cycle has been reported to determine physiological processes involved in cancer metabolism and cellular differentiation (Kishnani & Chen, 2013). In line with these findings, we observed the larger remodeling signatures of the hypoxia response corresponded to the glycolysis-to-TCA cycle axis, and were associated to a concomitant upregulation of acetyl-CoA and histone acetylation. Our data also revealed the upregulation of PDHK1, a highly recognized HIF1α-target that hinders acetyl-CoA synthesis in mitochondria. Although PDHK1 upregulation is part of the canonical hypoxic response model (Kaluz et al., 2008; Kim et al., 2006; Wenger et al., 2005)., we tested the possibility that PDHK1 might be mediating the interplay between acetyl-CoA and histone acetylation levels. Could PDHK1 have a role integrating chromatin and metabolism?

PDHK1 depletion using chemical inhibition has been reported to decrease cell survival in normal and cancer cell line models due to a remarkable loss on mitochondrial membrane polarization (Chatterjee et al., 2019). In contrast to these findings, our data suggest no effect on cellular proliferation upon lentiviral PDHK1 depletion, and no significant impact on mitochondrial metabolism that would point towards a membrane depolarization process. These contrasting results indicate that more work is needed to further understand the effects of PDHK1 depletion on cellular physiology. Furthermore, acknowledging the potential off-target effects of different inhibitory techniques would contribute to restrain technical artifacts from the analysis and delineate the underlying biological mechanisms.

Prior studies have shown that changes in metabolic phenotypes can derive from a rewiring of the contribution of the precursor metabolites that fuel a metabolite pool rather than a change in the metabolic pool size (Forny et al., 2023). Indeed, our findings show no change in acetyl-CoA pool size but a rewiring of its precursor metabolites instead. Using isotope

tracing, we observed that glucose contribution to the acetyl-CoA pool increases in the absence of PDHK1 whereas glutamine-carbon supply shortens under these conditions. Our data highlight the role of metabolic supply reprogramming as part of the functional metabolic adaptations that shape the hypoxia response in the absence of PDHK1. Future studies will contribute to elucidate the impact of metabolic supply reprogramming for multiple metabolic phenotypes.

Acetyl-CoA is a metabolic hub that connects multiple pathways and contributes to chromatin regulation through histone acetylation (Martínez-Reyes & Chandel, 2018; Takahashi et al., 2006; Wellen et al., 2009). Interestingly, when we measured the impact of PHDK1 depletion on this histone PTM, we observed a differential response at global and local scales since H3ac remains constant while H3K27ac decreases. The loss on H3K27ac represents a specific response on chromatin derived from PDHK1 depletion. Investigating whether H3K27ac location within chromatin is also rearranged in the absence of PDHK1 would contribute to further dissect the direct effect of this genetic depletion.

An observation that we found challenging to reconcile is the increase in glucose-derived acetyl-CoA and the coincident H3K27ac downregulation. Which pathways could be using the higher glucose-derived acetyl-CoA? Some of the most recognized vias for acetyl-CoA catabolism involve processes related to non-histone protein acetylation, fatty-acid synthesis, and the mevalonate pathway (Guertin & Wellen, 2023). The relative importance of each of these pathways is dynamic as it usually responds to context-specific cellular requirements. Our results pointed towards the initiation of a fatty-acid synthesis program, since we observe a higher malonyl-CoA pool size and a clear proteomic response into that direction. In line with this idea, our lipidomic analysis using isotope tracing showed a higher contribution of glucose toward newly synthesized fatty-acids.

These results suggest PDHK1 depletion changes the balance of acetyl-CoA usage to enhance fatty-acid synthesis and inhibit H3K27ac. These findings would support the idea that fatty-acids and histone acetylation compete for the same acetyl-CoA pool (Galdieri & Vancura, 2012). Prior findings have reported this metabolic crosstalk; however, an active role for PDHK1 within this balance mechanism was scarcely explored. We found that levels of H3K27ac were partially restored upon ACC1 inhibition, demonstrating a PDHK1-dependent modulation of acetyl-CoA distribution between fatty-acids and H3K27ac. Testing

this mechanism using a higher concentration (20 µM) of CP-640186 would help to exacerbate the fatty-acid and histone acetylation imbalance and definitively determine PDHK1 role within it.

In sum, our data reveals PDHK1 as a modulator of chromatin and metabolism in hypoxia. In specific, our work supports a model where PDHK1 depletion redistributes glucose-derived acetyl-CoA use from H3K27ac to fatty-acid synthesis. Future studies would further dissect the impact of PDHK1 depletion in hypoxia and would contribute to refine our understanding on the dynamic interplay between chromatin and metabolism.

7 CONCLUSION AND PERSPECTIVES

Dissecting the activity of individual metabolic pathways is essential to characterize the metabolic phenotypes of healthy and disease states. However, this is a technically challenging endeavor due to the subcellular compartmentalization of diverse metabolites, their differential abundance in whole-cell or compartmentalized extracts, and their distinct stability upon extraction (Andresen et al., 2022; Lee et al., 2019).

Studying acetyl-CoA metabolism using a subcellular compartment resolution permits the estimation of the mitochondrial and nuclear-cytosolic pool sizes or pathways activities accountable as separate entities (Trefely et al., 2022). Nowadays, the most common approaches to dissect metabolic pathway activity in general and acetyl-CoA metabolism in particular, rely on stable isotope labeling to perform metabolic flux measurements (Zamboni et al., 2009; Zamboni et al., 2015). The flux analysis's power is enhanced by continuously optimized techniques that allow a fast metabolic quenching at the subcellular compartment level and the subsequent separation of the targeted organelles (Chen et al., 2017; Dietz, 2017; Lee et al., 2019). Although these approaches have been at the forefront of metabolic studies, new techniques have emerged aiming to diminish the challenges imposed by current subcellular fractionation techniques (e.g., fraction purity, inter-organellar metabolic leakage) (Trefely et al., 2022). One of the most remarkable approaches is named SILEC-SF, a labeling method that cultures mammalian cells using the stable isotope of $^{15}N_1{}^{13}C_3$ -pantothenate, the precursor of CoA, to generate endogenous internal standards of acyl-CoA compounds (Trefely et al., 2022). SILEC cells are generated to match an experimental cell line (e.g., SILEC-NIH-3T3 and NIH-3T3) that will share similar experimental conditions (Trefely et al.,

2022). Once the experiment is completed, SILEC cells and experimental cells are mixed, forming a solution that is subsequently lysed, fractionated, and analyzed by LC-MS (Trefely et al., 2022). While this approach is financial and time-consuming regarding the generation of the SILEC cells and continuous comparison with the experimental cell line, to whom SILEC cells should match the most, it is particularly useful for *in vitro* studies focused on acyl-CoA metabolism (Trefely et al., 2022). Further investigation implementing SILEC-SF would contribute to refine our understanding of the metabolic rewiring of acyl-CoAs at subcellular compartment level.

The stability of short acyl-CoAs compounds (e.g., acetyl-CoA and malonyl-CoA) in solution is a considerable restriction that hinders its accurate identification and quantification by LC-MS (Liu et al., 2015; Tan et al., 2023). In addition, the differential abundance of acetyl-CoA and malonyl-CoA impedes their extraction from the same sample source. For instance, the samples prepared for the metabolic measurements of this thesis required an extra set whenever malonyl-CoA aimed was measured, which means that several preparation steps had to be included to quantify this metabolite. Recent studies have aimed to decrease these technical disadvantages by adding stabilizing compounds (e.g., butylated hydroxytoluene, caffeine) to the extraction solvent (Tan et al., 2023) or using different chromatography techniques (e.g., reversed-phase chromatography) that allow the simultaneous detection of multiple acyl-CoAs (Yang et al., 2017). Testing these innovative approaches would facilitate the high-throughput extraction of metabolites, reduce compound degradation, and improve data analysis and interpretation.

Assessing chromatin accessibility is essential to identify differentially regulated chromatin regions and characterize their associated transcriptional products (Henikoff et al., 2020). Many techniques are currently available for different experimental conditions, sample availability, and financial situations (Kaya-Okur et al., 2019). For instance, ChIP-seq and CUT&Tag methods target protein-chromatin associations (Kaya-Okur et al., 2019). However, CUT&Tag requires fewer cells and lower sequencing depth than ChIP-Seq, diminishing sequencing-associated costs (Kaya-Okur et al., 2019). Since CUT&Tag accurately detects histone PTMs (e.g., H3K27ac), this technique would allow targeting different histone PTMs to get a comprehensive overview of chromatin's functional status.

Given the importance of the glycolysis to TCA cycle transition controlled by PDC and PDHK1, several studies have associated their deregulation with pathological conditions related to cancer, neurological and muscular disorders, and cardiovascular diseases (Kishnani & Chen, 2013). For instance, PDC deficiency is associated with lactic acidemia, so under these circumstances, glycolytic tissues like the brain accumulate large amounts of lactic acid that can severely damage the nervous system (Bhagavan, 2002; Meirleir, 2013). Pharmacological treatments for PDC deficiency are scarce, so most therapeutical interventions to treat this disorder use ketogenic diets or thiamine (vitamin B1) supplementation to increase PDC activity and thereby reduce lactic acidosis (DeBrosse & Kerr, 2016; Meirleir, 2013; Singer et al., 2016). Ongoing research studies using dichloroacetate (DCA), a PDHK1 chemical inhibitor, to address PDC deficiency caused by PDHK1 upregulation (DeBrosse & Kerr, 2016; Meirleir, 2013). PDHK1 is upregulated in diverse cancers, in some cases associated with poor prognosis (e.g., breast cancer, gastric and colon carcinoma) or chemoresistant (e.g., bladder carcinoma) outcomes (Atas et al., 2020; Golias et al., 2019; He et al., 2018; Lu et al., 2011; Peng et al., 2018; Stacpoole, 2017; Woolbright et al., 2018). Thus, PDHK1 is considered a potential target for cancer treatment. Small molecule-based approaches targeting the binding sites for pyruvate, nucleotides, lipoamide, and allosteric regulation are currently under investigation (Saunier et al., 2016; Stacpoole, 2017).

The development of diverse “omics” technologies has enabled the high-throughput study of multiple cellular regulatory layers (e.g., metabolomics, proteomics, transcriptomics, genomics) (Athieniti & Spyrou, 2023; Cao & Gao, 2022). In most cases, these large datasets are generated and analyzed separately, due to the complex experimental setup intrinsic to each “omic” technology, their structurally different databases and distinct computational methods required to analyze them (Athieniti & Spyrou, 2023; Cao & Gao, 2022). However, integrating the results of different “omics” technologies opens the possibility to unveil far-reaching regulatory networks that can closely depict a comprehensive cellular functional state (Athieniti & Spyrou, 2023; Cao & Gao, 2022; Fraunhoffer et al., 2022). In addition, multi-omics data integration allows model developing, which contributes to generating mechanistic predictions on specific cellular processes that can be used for different purposes such as medical prognosis and therapeutics (Fraunhoffer et al., 2022). Therefore, integrating diverse “omics” technologies could improve our understanding on multiple cellular processes in healthy and disease states, to potentially design better therapeutic strategies.

8 REFERENCES

Abrankó, L., Williamson, G., Gardner, S., & Kerimi, A. (2018). Comprehensive quantitative analysis of fatty-acyl-Coenzyme A species in biological samples by ultra-high performance liquid chromatography-tandem mass spectrometry harmonizing hydrophilic interaction and reversed phase chromatography. *J Chromatogr A*, *1534*, 111-122. https://doi.org/10.1016/j.chroma.2017.12.052

Adkins, M. W., Howar, S. R., & Tyler, J. K. (2004). Chromatin Disassembly Mediated by the Histone Chaperone Asf1 Is Essential for Transcriptional Activation of the Yeast PHO5 and PHO8 Genes. *Molecular Cell*, *14*(5), 657-666. https://doi.org/https://doi.org/10.1016/j.molcel.2004.05.016

Agrawal, S., Kumar, S., Sehgal, R., George, S., Gupta, R., Poddar, S., Jha, A., & Pathak, S. (2019). El-MAVEN: A Fast, Robust, and User-Friendly Mass Spectrometry Data Processing Engine for Metabolomics. *Methods Mol Biol*, *1978*, 301-321. https://doi.org/10.1007/978-1-4939-9236-2_19

Alam, S., Gu, Y., Reichert, P., Bähler, J., & Oliferenko, S. (2023). Optimization of energy production and central carbon metabolism in a non-respiring eukaryote. *Current Biology*, *33*(11), 2175-2186.e2175. https://doi.org/https://doi.org/10.1016/j.cub.2023.04.046

Albenberg, L., Esipova, T. V., Judge, C. P., Bittinger, K., Chen, J., Laughlin, A., Grunberg, S., Baldassano, R. N., Lewis, J. D., Li, H., Thom, S. R., Bushman, F. D., Vinogradov, S. A., & Wu, G. D. (2014). Correlation between intraluminal oxygen gradient and radial partitioning of intestinal microbiota. *Gastroenterology*, *147*(5), 1055-1063.e1058. https://doi.org/10.1053/j.gastro.2014.07.020

Ali, I., Conrad, R. J., Verdin, E., & Ott, M. (2018). Lysine Acetylation Goes Global: From Epigenetics to Metabolism and Therapeutics. *Chem Rev*, *118*(3), 1216-1252. https://doi.org/10.1021/acs.chemrev.7b00181

Alseekh, S., Aharoni, A., Brotman, Y., Contrepois, K., D'Auria, J., Ewald, J., C. Ewald, J., Fraser, P. D., Giavalisco, P., Hall, R. D., Heinemann, M., Link, H., Luo, J., Neumann, S., Nielsen, J., Perez de Souza, L., Saito, K., Sauer, U., Schroeder, F. C., . . . Fernie, A. R. (2021). Mass spectrometry-based metabolomics: a guide for annotation, quantification and best reporting practices. *Nature Methods*, *18*(7), 747-756. https://doi.org/10.1038/s41592-021-01197-1

Andonegui-Elguera, M. A., Cáceres-Gutiérrez, R. E., López-Saavedra, A., Cisneros-Soberanis, F., Justo-Garrido, M., Díaz-Chávez, J., & Herrera, L. A. (2022). The Roles of Histone Post-Translational Modifications in the Formation and Function of a Mitotic Chromosome. *Int J Mol Sci*, *23*(15). https://doi.org/10.3390/ijms23158704

Andresen, C., Boch, T., Gegner, H. M., Mechtel, N., Narr, A., Birgin, E., Rasbach, E., Rahbari, N., Trumpp, A., Poschet, G., & Hübschmann, D. (2022). Comparison of extraction methods for intracellular metabolomics of human tissues [Original Research]. *Frontiers in Molecular Biosciences*, *9*. https://www.frontiersin.org/articles/10.3389/fmolb.2022.932261

Atas, E., Oberhuber, M., & Kenner, L. (2020). The Implications of PDK1-4 on Tumor Energy Metabolism, Aggressiveness and Therapy Resistance. *Front Oncol*, *10*, 583217. https://doi.org/10.3389/fonc.2020.583217

Athieniti, E., & Spyrou, G. M. (2023). A guide to multi-omics data collection and integration for translational medicine. *Computational and Structural Biotechnology Journal*, *21*, 134-149. https://doi.org/https://doi.org/10.1016/j.csbj.2022.11.050

Baldi, S., Korber, P., & Becker, P. B. (2020). Beads on a string—nucleosome array arrangements and folding of the chromatin fiber. *Nature Structural & Molecular Biology*, *27*(2), 109-118. https://doi.org/10.1038/s41594-019-0368-x

Bannister, A. J., & Kouzarides, T. (2011). Regulation of chromatin by histone modifications. *Cell Res*, *21*(3), 381-395. https://doi.org/10.1038/cr.2011.22

Batchuluun, B., Pinkosky, S. L., & Steinberg, G. R. (2022). Lipogenesis inhibitors: therapeutic opportunities and challenges. *Nature Reviews Drug Discovery*, *21*(4), 283-305. https://doi.org/10.1038/s41573-021-00367-2

Batie, M., Frost, J., Frost, M., Wilson, J. W., Schofield, P., & Rocha, S. (2019). Hypoxia induces rapid changes to histone methylation and reprograms chromatin. *Science*, *363*(6432), 1222-1226. https://doi.org/10.1126/science.aau5870

Bhagavan, N. V. (2002). CHAPTER 13 - Carbohydrate Metabolism I: Glycolysis and TCA Cycle. In N. V. Bhagavan (Ed.), *Medical Biochemistry (Fourth Edition)* (pp. 225-246). Academic Press. https://doi.org/https://doi.org/10.1016/B978-012095440-7/50015-9

Blankenburg, M., Haberland, L., Elvers, H. D., Tannert, C., & Jandrig, B. (2009). High-Throughput Omics Technologies: Potential Tools for the Investigation of Influences of EMF on Biological Systems. *Curr Genomics*, *10*(2), 86-92. https://doi.org/10.2174/138920209787847050

Brownsey, R. W., Boone, A. N., Elliott, J. E., Kulpa, J. E., & Lee, W. M. (2006). Regulation of acetyl-CoA carboxylase. *Biochem Soc Trans*, *34*(Pt 2), 223-227. https://doi.org/10.1042/bst20060223

Buenrostro, J. D., Wu, B., Chang, H. Y., & Greenleaf, W. J. (2015). ATAC-seq: A Method for Assaying Chromatin Accessibility Genome-Wide. *Curr Protoc Mol Biol*, *109*, 21.29.21-21.29.29. https://doi.org/10.1002/0471142727.mb2129s109

Buescher, J. M., Antoniewicz, M. R., Boros, L. G., Burgess, S. C., Brunengraber, H., Clish, C. B., DeBerardinis, R. J., Feron, O., Frezza, C., Ghesquiere, B., Gottlieb, E., Hiller, K., Jones, R. G., Kamphorst, J. J., Kibbey, R. G., Kimmelman, A. C., Locasale, J. W., Lunt, S. Y., Maddocks, O. D., . . . Fendt, S. M. (2015). A roadmap for interpreting (13)C metabolite labeling patterns from cells. *Curr Opin Biotechnol*, *34*, 189-201. https://doi.org/10.1016/j.copbio.2015.02.003

Byron, O., & Lindsay, J. G. (2017). The Pyruvate Dehydrogenase Complex and Related Assemblies in Health and Disease. *Subcell Biochem*, *83*, 523-550. https://doi.org/10.1007/978-3-319-46503-6_19

Cai, L., Sutter, B. M., Li, B., & Tu, B. P. (2011). Acetyl-CoA induces cell growth and proliferation by promoting the acetylation of histones at growth genes. *Mol Cell*, *42*(4), 426-437. https://doi.org/10.1016/j.molcel.2011.05.004

Calder, P. C. (2016). Fatty Acids: Metabolism. In B. Caballero, P. M. Finglas, & F. Toldrá (Eds.), *Encyclopedia of Food and Health* (pp. 632-644). Academic Press. https://doi.org/https://doi.org/10.1016/B978-0-12-384947-2.00276-2

Cao, Z.-J., & Gao, G. (2022). Multi-omics single-cell data integration and regulatory inference with graph-linked embedding. *Nature Biotechnology*, *40*(10), 1458-1466. https://doi.org/10.1038/s41587-022-01284-4

Carreau, A., Hafny-Rahbi, B. E., Matejuk, A., Grillon, C., & Kieda, C. (2011). Why is the partial oxygen pressure of human tissues a crucial parameter? Small molecules and hypoxia. *Journal of Cellular and Molecular Medicine*, *15*(6), 1239-1253. https://doi.org/https://doi.org/10.1111/j.1582-4934.2011.01258.x

Chakravarthy, S., Park, Y.-J., Chodaparambil, J., Edayathumangalam, R. S., & Luger, K. (2005). Structure and dynamic properties of nucleosome core particles. *FEBS Letters*, *579*(4), 895-898. https://doi.org/https://doi.org/10.1016/j.febslet.2004.11.030

Chambers, M. C., Maclean, B., Burke, R., Amodei, D., Ruderman, D. L., Neumann, S., Gatto, L., Fischer, B., Pratt, B., Egertson, J., Hoff, K., Kessner, D., Tasman, N., Shulman, N., Frewen, B., Baker, T. A., Brusniak, M. Y., Paulse, C., Creasy, D., . . . Mallick, P. (2012). A cross-platform toolkit for mass spectrometry and proteomics. *Nat Biotechnol*, *30*(10), 918-920. https://doi.org/10.1038/nbt.2377

Chatterjee, N., Pazarentzos, E., Mayekar, M. K., Gui, P., Allegakoen, D. V., Hrustanovic, G., Olivas, V., Lin, L., Verschueren, E., Johnson, J. R., Hofree, M., Yan, J. J., Newton, B. W., Dollen, J. V., Earnshaw, C. H., Flanagan, J., Chan, E., Asthana, S., Ideker, T., . . . Bivona, T. G. (2019). Synthetic Essentiality of Metabolic Regulator PDHK1 in PTEN-Deficient Cells and Cancers. *Cell Reports*, *28*(9), 2317-2330.e2318. https://doi.org/https://doi.org/10.1016/j.celrep.2019.07.063

Chen, W. W., Freinkman, E., & Sabatini, D. M. (2017). Rapid immunopurification of mitochondria for metabolite profiling and absolute quantification of matrix metabolites. *Nature Protocols*, *12*(10), 2215-2231. https://doi.org/10.1038/nprot.2017.104

Chow, J. D., Lawrence, R. T., Healy, M. E., Dominy, J. E., Liao, J. A., Breen, D. S., Byrne, F. L., Kenwood, B. M., Lackner, C., Okutsu, S., Mas, V. R., Caldwell, S. H., Tomsig, J. L., Cooney, G. J., Puigserver, P. B., Turner, N., James, D. E., Villén, J., & Hoehn, K. L. (2014). Genetic inhibition of hepatic acetyl-CoA carboxylase activity increases liver fat and alters global protein acetylation. *Mol Metab*, *3*(4), 419-431. https://doi.org/10.1016/j.molmet.2014.02.004

Collins, J. A., Rudenski, A., Gibson, J., Howard, L., & O'Driscoll, R. (2015). Relating oxygen partial pressure, saturation and content: the haemoglobin-oxygen dissociation curve. *Breathe (Sheff)*, *11*(3), 194-201. https://doi.org/10.1183/20734735.001415

Coskun, O. (2016). Separation techniques: Chromatography. *North Clin Istanb*, *3*(2), 156-160. https://doi.org/10.14744/nci.2016.32757

Cox, J., & Mann, M. (2008). MaxQuant enables high peptide identification rates, individualized p.p.b.-range mass accuracies and proteome-wide protein quantification. *Nature Biotechnology*, *26*(12), 1367-1372. https://doi.org/10.1038/nbt.1511

Creyghton, M. P., Cheng, A. W., Welstead, G. G., Kooistra, T., Carey, B. W., Steine, E. J., Hanna, J., Lodato, M. A., Frampton, G. M., Sharp, P. A., Boyer, L. A., Young, R. A., & Jaenisch, R. (2010). Histone H3K27ac separates active from poised enhancers and predicts developmental state. *Proceedings of the National Academy of Sciences*, *107*(50), 21931-21936. https://doi.org/10.1073/pnas.1016071107

Dai, Z., & Locasale, J. W. (2017). Understanding metabolism with flux analysis: From theory to application. *Metab Eng*, *43*(Pt B), 94-102. https://doi.org/10.1016/j.ymben.2016.09.005

Dai, Z., Ramesh, V., & Locasale, J. W. (2020). The evolving metabolic landscape of chromatin biology and epigenetics. *Nat Rev Genet*, *21*(12), 737-753. https://doi.org/10.1038/s41576-020-0270-8

DeBrosse, S. D., & Kerr, D. S. (2016). Chapter 12 - Pyruvate Dehydrogenase Complex Deficiency. In R. P. Saneto, S. Parikh, & B. H. Cohen (Eds.), *Mitochondrial Case Studies* (pp. 93-101). Academic Press. https://doi.org/https://doi.org/10.1016/B978-0-12-800877-5.00012-7

Dengler, V. L., Galbraith, M., & Espinosa, J. M. (2014). Transcriptional regulation by hypoxia inducible factors. *Crit Rev Biochem Mol Biol*, *49*(1), 1-15. https://doi.org/10.3109/10409238.2013.838205

Desvergne, B., Michalik, L., & Wahli, W. (2006). Transcriptional Regulation of Metabolism. *Physiological Reviews*, *86*(2), 465-514. https://doi.org/10.1152/physrev.00025.2005

Di Gennaro, E., Bruzzese, F., Caraglia, M., Abruzzese, A., & Budillon, A. (2004). Acetylation of proteins as novel target for antitumor therapy: Review article. *Amino Acids*, *26*(4), 435-441. https://doi.org/10.1007/s00726-004-0087-3

Dietz, K. J. (2017). Subcellular metabolomics: the choice of method depends on the aim of the study. *J Exp Bot*, *68*(21-22), 5695-5698. https://doi.org/10.1093/jxb/erx406

Dombrowski, M., Engeholm, M., Dienemann, C., Dodonova, S., & Cramer, P. (2022). Histone H1 binding to nucleosome arrays depends on linker DNA length and trajectory. *Nature Structural & Molecular Biology*, *29*(5), 493-501. https://doi.org/10.1038/s41594-022-00768-w

Eales, K. L., Hollinshead, K. E. R., & Tennant, D. A. (2016). Hypoxia and metabolic adaptation of cancer cells. *Oncogenesis*, *5*(1), e190-e190. https://doi.org/10.1038/oncsis.2015.50

Etchegaray, J.-P., & Mostoslavsky, R. (2016). Interplay between Metabolism and Epigenetics: A Nuclear Adaptation to Environmental Changes. *Molecular Cell*, *62*(5), 695-711. https://doi.org/https://doi.org/10.1016/j.molcel.2016.05.029

Everts, A. G., Zee, B. M., Dimaggio, P. A., Gonzales-Cope, M., Coller, H. A., & Garcia, B. A. (2013). Quantitative dynamics of the link between cellular metabolism and histone acetylation. *J Biol Chem*, *288*(17), 12142-12151. https://doi.org/10.1074/jbc.M112.428318

Forny, P., Bonilla, X., Lamparter, D., Shao, W., Plessl, T., Frei, C., Bingisser, A., Goetze, S., van Drogen, A., Harshman, K., Pedrioli, P. G. A., Howald, C., Poms, M., Traversi, F., Bürer, C., Cherkaoui, S., Morscher, R. J., Simmons, L., Forny, M., . . . Froese, D. S. (2023). Integrated multi-omics reveals anaplerotic rewiring in methylmalonyl-CoA mutase deficiency. *Nature Metabolism*, *5*(1), 80-95. https://doi.org/10.1038/s42255-022-00720-8

Forsberg, B. O., Aibara, S., Howard, R. J., Mortezaei, N., & Lindahl, E. (2020). Arrangement and symmetry of the fungal E3BP-containing core of the pyruvate dehydrogenase complex. *Nature Communications*, *11*(1), 4667. https://doi.org/10.1038/s41467-020-18401-z

Fraunhoffer, N. A., Abuelafia, A. M., Bigonnet, M., Gayet, O., Roques, J., Nicolle, R., Lomberk, G., Urrutia, R., Dusetti, N., & Iovanna, J. (2022). Multi-omics data integration and modeling unravels new mechanisms for pancreatic cancer and improves prognostic prediction. *npj Precision Oncology*, *6*(1), 57. https://doi.org/10.1038/s41698-022-00299-z

Fullerton, M. D., Galic, S., Marcinko, K., Sikkema, S., Pulinilkunnil, T., Chen, Z. P., O'Neill, H. M., Ford, R. J., Palanivel, R., O'Brien, M., Hardie, D. G., Macaulay, S. L., Schertzer, J. D., Dyck, J. R., van Denderen, B. J., Kemp, B. E., & Steinberg, G. R. (2013). Single phosphorylation sites in Acc1 and Acc2 regulate lipid homeostasis and the insulin-sensitizing effects of metformin. *Nat Med*, *19*(12), 1649-1654. https://doi.org/10.1038/nm.3372

Galdieri, L., & Vancura, A. (2012). Acetyl-CoA Carboxylase Regulates Global Histone Acetylation*♦. *Journal of Biological Chemistry*, *287*(28), 23865-23876. https://doi.org/https://doi.org/10.1074/jbc.M112.380519

Galic, S., Loh, K., Murray-Segal, L., Steinberg, G. R., Andrews, Z. B., & Kemp, B. E. (2018). AMPK signaling to acetyl-CoA carboxylase is required for fasting- and cold-induced appetite but not thermogenesis. *Elife*, *7*. https://doi.org/10.7554/eLife.32656

Gerlt, J. A. (1999). 5.02 - Stabilization of Reactive Intermediates and Transition States in Enzyme Active Sites by Hydrogen Bonding. In S. D. Barton, K. Nakanishi, & O. Meth-Cohn (Eds.), *Comprehensive Natural Products Chemistry* (pp. 5-29). Pergamon. https://doi.org/https://doi.org/10.1016/B978-0-08-091283-7.00131-4

Golias, T., Kery, M., Radenkovic, S., & Papandreou, I. (2019). Microenvironmental control of glucose metabolism in tumors by regulation of pyruvate dehydrogenase. *Int J Cancer*, *144*(4), 674-686. https://doi.org/10.1002/ijc.31812

Gray, L. R., Tompkins, S. C., & Taylor, E. B. (2014). Regulation of pyruvate metabolism and human disease. *Cell Mol Life Sci*, *71*(14), 2577-2604. https://doi.org/10.1007/s00018-013-1539-2

Green, T., Grigorian, A., Klyuyeva, A., Tuganova, A., Luo, M., & Popov, K. M. (2008). Structural and functional insights into the molecular mechanisms responsible for the regulation of pyruvate dehydrogenase kinase 2. *J Biol Chem*, *283*(23), 15789-15798. https://doi.org/10.1074/jbc.M800311200

Grunstein, M. (1997). Histone acetylation in chromatin structure and transcription. *Nature*, *389*(6649), 349-352. https://doi.org/10.1038/38664

Guertin, D. A., & Wellen, K. E. (2023). Acetyl-CoA metabolism in cancer. *Nature Reviews Cancer*, *23*(3), 156-172. https://doi.org/10.1038/s41568-022-00543-5

Harwood, H. J., Jr., Petras, S. F., Shelly, L. D., Zaccaro, L. M., Perry, D. A., Makowski, M. R., Hargrove, D. M., Martin, K. A., Tracey, W. R., Chapman, J. G., Magee, W. P., Dalvie, D. K., Soliman, V. F., Martin, W. H., Mularski, C. J., & Eisenbeis, S. A. (2003). Isozyme-nonselective N-substituted bipiperidylcarboxamide acetyl-CoA carboxylase inhibitors reduce tissue malonyl-CoA concentrations, inhibit fatty acid synthesis, and increase fatty acid oxidation in cultured cells and in experimental animals. *J Biol Chem*, *278*(39), 37099-37111. https://doi.org/10.1074/jbc.M304481200

He, Z., Li, Z., Zhang, X., Yin, K., Wang, W., Xu, Z., Li, B., Zhang, L., Xu, J., Sun, G., Wang, L., Li, Q., Huang, X., Zhang, L., Zhang, D., Xu, H., & Xu, Z. (2018). MiR-422a regulates cellular metabolism and malignancy by targeting pyruvate dehydrogenase kinase 2 in gastric cancer. *Cell Death Dis*, *9*(5), 505. https://doi.org/10.1038/s41419-018-0564-3

Heinrich, P., Kohler, C., Ellmann, L., Kuerner, P., Spang, R., Oefner, P. J., & Dettmer, K. (2018). Correcting for natural isotope abundance and tracer impurity in MS-, MS/MS- and high-resolution-multiple-tracer-data from stable isotope labeling experiments with IsoCorrectoR. *Scientific Reports*, *8*(1), 17910. https://doi.org/10.1038/s41598-018-36293-4

Henikoff, S., Henikoff, J. G., Kaya-Okur, H. S., & Ahmad, K. (2020). Efficient chromatin accessibility mapping in situ by nucleosome-tethered tagmentation. *Elife*, *9*, e63274. https://doi.org/10.7554/eLife.63274

Hnisz, D., Abraham, Brian J., Lee, Tong I., Lau, A., Saint-André, V., Sigova, Alla A., Hoke, Heather A., & Young, Richard A. (2013). Super-Enhancers in the Control of Cell Identity and Disease. *Cell*, *155*(4), 934-947. https://doi.org/https://doi.org/10.1016/j.cell.2013.09.053

Huether, R., Dong, L., Chen, X., Wu, G., Parker, M., Wei, L., Ma, J., Edmonson, M. N., Hedlund, E. K., Rusch, M. C., Shurtleff, S. A., Mulder, H. L., Boggs, K., Vadordaria, B., Cheng, J., Yergeau, D., Song, G., Becksfort, J., Lemmon, G., . . . Downing, J. R. (2014). The landscape of somatic mutations in epigenetic regulators across 1,000 paediatric cancer genomes. *Nat Commun*, *5*, 3630. https://doi.org/10.1038/ncomms4630

Hynes, M. J., & Murray, S. L. (2010). ATP-citrate lyase is required for production of cytosolic acetyl coenzyme A and development in Aspergillus nidulans. *Eukaryot Cell*, *9*(7), 1039-1048. https://doi.org/10.1128/ec.00080-10

Izzo, L. T., Trefely, S., Demetriadou, C., Drummond, J. M., Mizukami, T., Kuprasertkul, N., Farria, A. T., Nguyen, P. T. T., Murali, N., Reich, L., Kantner, D. S., Shaffer, J., Affronti, H., Carrer, A., Andrews, A., Capell, B. C., Snyder, N. W., & Wellen, K. E. (2023).

Acetylcarnitine shuttling links mitochondrial metabolism to histone acetylation and lipogenesis. *Sci Adv*, *9*(18), eadf0115. https://doi.org/10.1126/sciadv.adf0115

Jang, C., Chen, L., & Rabinowitz, J. D. (2018). Metabolomics and Isotope Tracing. *Cell*, *173*(4), 822-837. https://doi.org/10.1016/j.cell.2018.03.055

Jewell, U. R., Kvietikova, I., Scheid, A., Bauer, C., Wenger, R. H., & Gassmann, M. (2001). Induction of HIF–1α in response to hypoxia is instantaneous. *The FASEB Journal*, *15*(7), 1312-1314. https://doi.org/https://doi.org/10.1096/fj.00-0732fje

Johnson, X., & Alric, J. (2013). Central carbon metabolism and electron transport in Chlamydomonas reinhardtii: metabolic constraints for carbon partitioning between oil and starch. *Eukaryot Cell*, *12*(6), 776-793. https://doi.org/10.1128/ec.00318-12

Kaelin, W. G., Jr., & Ratcliffe, P. J. (2008). Oxygen sensing by metazoans: the central role of the HIF hydroxylase pathway. *Mol Cell*, *30*(4), 393-402. https://doi.org/10.1016/j.molcel.2008.04.009

Kaluz, S., Kaluzová, M., & Stanbridge, E. J. (2008). Regulation of gene expression by hypoxia: integration of the HIF-transduced hypoxic signal at the hypoxia-responsive element. *Clin Chim Acta*, *395*(1-2), 6-13. https://doi.org/10.1016/j.cca.2008.05.002

Kantor, P. F., Lopaschuk, G. D., & Opie, L. H. (2001). CHAPTER 32 - Myocardial Energy Metabolism. In N. Sperelakis, Y. Kurachi, A. Terzic, & M. V. Cohen (Eds.), *Heart Physiology and Pathophysiology (Fourth Edition)* (pp. 543-569). Academic Press. https://doi.org/https://doi.org/10.1016/B978-012656975-9/50034-1

Kaya-Okur, H. S., Wu, S. J., Codomo, C. A., Pledger, E. S., Bryson, T. D., Henikoff, J. G., Ahmad, K., & Henikoff, S. (2019). CUT&Tag for efficient epigenomic profiling of small samples and single cells. *Nature Communications*, *10*(1), 1930. https://doi.org/10.1038/s41467-019-09982-5

Kerner, J., Minkler, P. E., Lesnefsky, E. J., & Hoppel, C. L. (2014). Fatty acid chain elongation in palmitate-perfused working rat heart: mitochondrial acetyl-CoA is the source of two-carbon units for chain elongation. *J Biol Chem*, *289*(14), 10223-10234. https://doi.org/10.1074/jbc.M113.524314

Kim, J. W., Tchernyshyov, I., Semenza, G. L., & Dang, C. V. (2006). HIF-1-mediated expression of pyruvate dehydrogenase kinase: a metabolic switch required for cellular adaptation to hypoxia. *Cell Metab*, *3*(3), 177-185. https://doi.org/10.1016/j.cmet.2006.02.002

Kishnani, P. S., & Chen, Y.-T. (2013). Chapter 93 - Disorders of Carbohydrate Metabolism. In D. Rimoin, R. Pyeritz, & B. Korf (Eds.), *Emery and Rimoin's Principles and Practice of Medical Genetics (Sixth Edition)* (pp. 1-36). Academic Press. https://doi.org/https://doi.org/10.1016/B978-0-12-383834-6.00097-5

Kloska, A., Węsierska, M., Malinowska, M., Gabig-Cimińska, M., & Jakóbkiewicz-Banecka, J. (2020). Lipophagy and Lipolysis Status in Lipid Storage and Lipid Metabolism Diseases. *International Journal of Molecular Sciences*, *21*(17).

Kocianova, E., Piatrikova, V., & Golias, T. (2022). Revisiting the Warburg Effect with Focus on Lactate. *Cancers*, *14*(24).

Koltai, T., Reshkin, S. J., & Harguindey, S. (2020). Chapter 16 - Pharmacological interventions part IV: Metabolic modifiers. In T. Koltai, S. J. Reshkin, & S. Harguindey (Eds.), *An Innovative Approach to Understanding and Treating Cancer: Targeting pH* (pp. 361-416). Academic Press. https://doi.org/https://doi.org/10.1016/B978-0-12-819059-3.00016-2

Korolev, N., Vorontsova, O. V., & Nordenskiöld, L. (2007). Physicochemical analysis of electrostatic foundation for DNA–protein interactions in chromatin transformations. *Progress in Biophysics and Molecular Biology*, *95*(1), 23-49. https://doi.org/https://doi.org/10.1016/j.pbiomolbio.2006.11.003

Kuna, R. S., Kumar, A., Wessendorf-Rodriguez, K. A., Galvez, H., Green, C. R., McGregor, G. H., Cordes, T., Shaw, R. J., Svensson, R. U., & Metallo, C. M. Inter-organelle cross-talk supports acetyl-coenzyme A homeostasis and lipogenesis under metabolic stress. *Science Advances*, *9*(18), eadf0138. https://doi.org/10.1126/sciadv.adf0138

Kuntz, M. J., & Harris, R. A. (2018). Pyruvate Dehydrogenase Kinase. In S. Choi (Ed.), *Encyclopedia of Signaling Molecules* (pp. 1-9). Springer New York. https://doi.org/10.1007/978-1-4614-6438-9_101636-2

Kurdistani, S. K., Tavazoie, S., & Grunstein, M. (2004). Mapping global histone acetylation patterns to gene expression. *Cell*, *117*(6), 721-733. https://doi.org/10.1016/j.cell.2004.05.023

Lee, J. V., Carrer, A., Shah, S., Snyder, N. W., Wei, S., Venneti, S., Worth, A. J., Yuan, Z. F., Lim, H. W., Liu, S., Jackson, E., Aiello, N. M., Haas, N. B., Rebbeck, T. R., Judkins, A., Won, K. J., Chodosh, L. A., Garcia, B. A., Stanger, B. Z., . . . Wellen, K. E. (2014). Akt-dependent metabolic reprogramming regulates tumor cell histone acetylation. *Cell Metab*, *20*(2), 306-319. https://doi.org/10.1016/j.cmet.2014.06.004

Lee, W. D., Mukha, D., Aizenshtein, E., & Shlomi, T. (2019). Spatial-fluxomics provides a subcellular-compartmentalized view of reductive glutamine metabolism in cancer cells. *Nat Commun*, *10*(1), 1351. https://doi.org/10.1038/s41467-019-09352-1

Leidecker, O., Bonfiglio, J. J., Colby, T., Zhang, Q., Atanassov, I., Zaja, R., Palazzo, L., Stockum, A., Ahel, I., & Matic, I. (2016). Serine is a new target residue for endogenous ADP-ribosylation on histones. *Nature Chemical Biology*, *12*(12), 998-1000. https://doi.org/10.1038/nchembio.2180

Li, X., Egervari, G., Wang, Y., Berger, S. L., & Lu, Z. (2018). Regulation of chromatin and gene expression by metabolic enzymes and metabolites. *Nat Rev Mol Cell Biol*, *19*(9), 563-578. https://doi.org/10.1038/s41580-018-0029-7

Li, X., Yang, Y., Zhang, B., Lin, X., Fu, X., An, Y., Zou, Y., Wang, J. X., Wang, Z., & Yu, T. (2022). Lactate metabolism in human health and disease. *Signal Transduct Target Ther*, *7*(1), 305. https://doi.org/10.1038/s41392-022-01151-3

Ling, R., Chen, G., Tang, X., Liu, N., Zhou, Y., & Chen, D. (2022). Acetyl-CoA synthetase 2(ACSS2): a review with a focus on metabolism and tumor development. *Discov Oncol*, *13*(1), 58. https://doi.org/10.1007/s12672-022-00521-1

Liu, X., Cooper, D. E., Cluntun, A. A., Warmoes, M. O., Zhao, S., Reid, M. A., Liu, J., Lund, P. J., Lopes, M., Garcia, B. A., Wellen, K. E., Kirsch, D. G., & Locasale, J. W. (2018). Acetate Production from Glucose and Coupling to Mitochondrial Metabolism in Mammals. *Cell*, *175*(2), 502-513.e513. https://doi.org/10.1016/j.cell.2018.08.040

Liu, X., Sadhukhan, S., Sun, S., Wagner, G. R., Hirschey, M. D., Qi, L., Lin, H., & Locasale, J. W. (2015). High-Resolution Metabolomics with Acyl-CoA Profiling Reveals Widespread Remodeling in Response to Diet. *Molecular & cellular proteomics : MCP*, *14*(6), 1489-1500. https://doi.org/10.1074/mcp.M114.044859

Liu, X., Wang, L., Zhao, K., Thompson, P. R., Hwang, Y., Marmorstein, R., & Cole, P. A. (2008). The structural basis of protein acetylation by the p300/CBP transcriptional coactivator. *Nature*, *451*(7180), 846-850. https://doi.org/10.1038/nature06546

Locasale, J. W. (2013). Serine, glycine and one-carbon units: cancer metabolism in full circle. *Nature Reviews Cancer*, *13*(8), 572-583. https://doi.org/10.1038/nrc3557

Lombardi, O., Li, R., Halim, S., Choudhry, H., Ratcliffe, P. J., & Mole, D. R. (2022). Pan-cancer analysis of tissue and single-cell HIF-pathway activation using a conserved gene signature. *Cell Rep*, *41*(7), 111652. https://doi.org/10.1016/j.celrep.2022.111652

Lu, C., & Thompson, Craig B. (2012). Metabolic Regulation of Epigenetics. *Cell Metabolism*, *16*(1), 9-17. https://doi.org/https://doi.org/10.1016/j.cmet.2012.06.001

Lu, C., Ward, P. S., Kapoor, G. S., Rohle, D., Turcan, S., Abdel-Wahab, O., Edwards, C. R., Khanin, R., Figueroa, M. E., Melnick, A., Wellen, K. E., O'Rourke, D. M., Berger, S. L., Chan, T. A., Levine, R. L., Mellinghoff, I. K., & Thompson, C. B. (2012). IDH mutation impairs histone demethylation and results in a block to cell differentiation. *Nature*, *483*(7390), 474-478. https://doi.org/10.1038/nature10860

Lu, C. W., Lin, S. C., Chien, C. W., Lin, S. C., Lee, C. T., Lin, B. W., Lee, J. C., & Tsai, S. J. (2011). Overexpression of pyruvate dehydrogenase kinase 3 increases drug resistance and early recurrence in colon cancer. *Am J Pathol*, *179*(3), 1405-1414. https://doi.org/10.1016/j.ajpath.2011.05.050

Lundsgaard, A.-M., Fritzen, A. M., & Kiens, B. (2018). Molecular Regulation of Fatty Acid Oxidation in Skeletal Muscle during Aerobic Exercise. *Trends in Endocrinology & Metabolism*, *29*(1), 18-30. https://doi.org/https://doi.org/10.1016/j.tem.2017.10.011

Luster, A. D., Alon, R., & von Andrian, U. H. (2005). Immune cell migration in inflammation: present and future therapeutic targets. *Nature Immunology*, *6*(12), 1182-1190. https://doi.org/10.1038/ni1275

Martínez-Reyes, I., & Chandel, N. S. (2018). Acetyl-CoA-directed gene transcription in cancer cells. *Genes Dev*, *32*(7-8), 463-465. https://doi.org/10.1101/gad.315168.118

McDonnell, E., Crown, S. B., Fox, D. B., Kitir, B., Ilkayeva, O. R., Olsen, C. A., Grimsrud, P. A., & Hirschey, M. D. (2016). Lipids Reprogram Metabolism to Become a Major Carbon Source for Histone Acetylation. *Cell Reports*, *17*(6), 1463-1472. https://doi.org/https://doi.org/10.1016/j.celrep.2016.10.012

McGinty, R. K., & Tan, S. (2015). Nucleosome structure and function. *Chem Rev*, *115*(6), 2255-2273. https://doi.org/10.1021/cr500373h

McKeown, S. R. (2014). Defining normoxia, physoxia and hypoxia in tumours-implications for treatment response. *Br J Radiol*, *87*(1035), 20130676. https://doi.org/10.1259/bjr.20130676

Meirleir, L. D. (2013). Chapter 169 - Disorders of pyruvate metabolism. In O. Dulac, M. Lassonde, & H. B. Sarnat (Eds.), *Handbook of Clinical Neurology* (Vol. 113, pp. 1667-1673). Elsevier. https://doi.org/https://doi.org/10.1016/B978-0-444-59565-2.00034-4

Melvin, A., & Rocha, S. (2012). Chromatin as an oxygen sensor and active player in the hypoxia response. *Cellular Signalling*, *24*(1), 35-43. https://doi.org/https://doi.org/10.1016/j.cellsig.2011.08.019

Milne, J. L. S. (2013). Structure and Regulation of Pyruvate Dehydrogenases. In W. J. Lennarz & M. D. Lane (Eds.), *Encyclopedia of Biological Chemistry (Second Edition)* (pp. 321-328). Academic Press. https://doi.org/https://doi.org/10.1016/B978-0-12-378630-2.00079-7

Nativio, R., Lan, Y., Donahue, G., Sidoli, S., Berson, A., Srinivasan, A. R., Shcherbakova, O., Amlie-Wolf, A., Nie, J., Cui, X., He, C., Wang, L.-S., Garcia, B. A., Trojanowski, J. Q., Bonini, N. M., & Berger, S. L. (2020). An integrated multi-omics approach identifies epigenetic alterations associated with Alzheimer's disease. *Nature Genetics*, *52*(10), 1024-1035. https://doi.org/10.1038/s41588-020-0696-0

Noor, E., Eden, E., Milo, R., & Alon, U. (2010). Central Carbon Metabolism as a Minimal Biochemical Walk between Precursors for Biomass and Energy. *Molecular Cell*, *39*(5), 809-820. https://doi.org/10.1016/j.molcel.2010.08.031

Park, S.-Y., & Kim, J.-S. (2020). A short guide to histone deacetylases including recent progress on class II enzymes. *Experimental & Molecular Medicine*, *52*(2), 204-212. https://doi.org/10.1038/s12276-020-0382-4

Patel, M. S., Nemeria, N. S., Furey, W., & Jordan, F. (2014). The pyruvate dehydrogenase complexes: structure-based function and regulation. *J Biol Chem*, *289*(24), 16615-16623. https://doi.org/10.1074/jbc.R114.563148

Peng, F., Wang, J. H., Fan, W. J., Meng, Y. T., Li, M. M., Li, T. T., Cui, B., Wang, H. F., Zhao, Y., An, F., Guo, T., Liu, X. F., Zhang, L., Lv, L., Lv, D. K., Xu, L. Z., Xie, J. J., Lin, W. X., Lam, E. W. F., . . . Liu, Q. (2018). Glycolysis gatekeeper PDK1 reprograms breast cancer stem cells under hypoxia. *Oncogene*, *37*(8), 1062-1074. https://doi.org/10.1038/onc.2017.368

Peng, M., Yin, N., Chhangawala, S., Xu, K., Leslie, C. S., & Li, M. O. (2016). Aerobic glycolysis promotes T helper 1 cell differentiation through an epigenetic mechanism. *Science*, *354*(6311), 481-484. https://doi.org/10.1126/science.aaf6284

Pietrocola, F., Galluzzi, L., Bravo-San Pedro, José M., Madeo, F., & Kroemer, G. (2015). Acetyl Coenzyme A: A Central Metabolite and Second Messenger. *Cell Metabolism*, *21*(6), 805-821. https://doi.org/https://doi.org/10.1016/j.cmet.2015.05.014

Place, T. L., Domann, F. E., & Case, A. J. (2017). Limitations of oxygen delivery to cells in culture: An underappreciated problem in basic and translational research. *Free Radical Biology and Medicine*, *113*, 311-322. https://doi.org/https://doi.org/10.1016/j.freeradbiomed.2017.10.003

Pouikli, A., Parekh, S., Maleszewska, M., Nikopoulou, C., Baghdadi, M., Tripodi, I., Folz-Donahue, K., Hinze, Y., Mesaros, A., Hoey, D., Giavalisco, P., Dowell, R., Partridge, L., & Tessarz, P. (2021). Chromatin remodeling due to degradation of citrate carrier impairs osteogenesis of aged mesenchymal stem cells. *Nat Aging*, *1*(9), 810-825. https://doi.org/10.1038/s43587-021-00105-8

Pouikli, A., & Tessarz, P. (2021). Metabolism and chromatin: A dynamic duo that regulates development and ageing. *BioEssays*, *43*(5), 2000273. https://doi.org/https://doi.org/10.1002/bies.202000273

Prasannan, C. B., Jaiswal, D., Davis, R., & Wangikar, P. P. (2018). An improved method for extraction of polar and charged metabolites from cyanobacteria. *PLoS One*, *13*(10), e0204273. https://doi.org/10.1371/journal.pone.0204273

Rada-Iglesias, A., Bajpai, R., Swigut, T., Brugmann, S. A., Flynn, R. A., & Wysocka, J. (2011). A unique chromatin signature uncovers early developmental enhancers in humans. *Nature*, *470*(7333), 279-283. https://doi.org/10.1038/nature09692

Ramazi, S., Allahverdi, A., & Zahiri, J. (2020). Evaluation of post-translational modifications in histone proteins: A review on histone modification defects in developmental and neurological disorders. *J Biosci*, *45*.

Randle, P. J., & Denton, R. M. (1976, 1976//). Regulation of Pyruvate Dehydrogenase by End Product Inhibition and by Phosphorylation. Metabolic Interconversion of Enzymes 1975, Berlin, Heidelberg.

Rappsilber, J., Ishihama, Y., & Mann, M. (2003). Stop and go extraction tips for matrix-assisted laser desorption/ionization, nanoelectrospray, and LC/MS sample pretreatment in proteomics. *Anal Chem*, *75*(3), 663-670. https://doi.org/10.1021/ac026117i

Rardin, M. J., Wiley, S. E., Naviaux, R. K., Murphy, A. N., & Dixon, J. E. (2009). Monitoring phosphorylation of the pyruvate dehydrogenase complex. *Anal Biochem*, *389*(2), 157-164. https://doi.org/10.1016/j.ab.2009.03.040

Reed, L. J. (2001). A Trail of Research from Lipoic Acid to α-Keto Acid Dehydrogenase Complexes. *Journal of Biological Chemistry*, *276*(42), 38329-38336. https://doi.org/https://doi.org/10.1074/jbc.R100026200

Reid, M. A., Dai, Z., & Locasale, J. W. (2017). The impact of cellular metabolism on chromatin dynamics and epigenetics. *Nature Cell Biology*, *19*(11), 1298-1306. https://doi.org/10.1038/ncb3629

Ritchie, M. E., Phipson, B., Wu, D., Hu, Y., Law, C. W., Shi, W., & Smyth, G. K. (2015). limma powers differential expression analyses for RNA-sequencing and microarray studies. *Nucleic Acids Res*, *43*(7), e47. https://doi.org/10.1093/nar/gkv007

Rowles, J., Scherer, S. W., Xi, T., Majer, M., Nickle, D. C., Rommens, J. M., Popov, K. M., Harris, R. A., Riebow, N. L., Xia, J., Tsui, L. C., Bogardus, C., & Prochazka, M. (1996). Cloning and characterization of PDK4 on 7q21.3 encoding a fourth pyruvate dehydrogenase kinase isoenzyme in human. *J Biol Chem*, *271*(37), 22376-22382. https://doi.org/10.1074/jbc.271.37.22376

Rye, P. T., Frick, L. E., Ozbal, C. C., & Lamarr, W. A. (2011). Advances in Label-Free Screening Approaches for Studying Histone Acetyltransferases. *SLAS Discovery*, *16*(10), 1186-1195. https://doi.org/https://doi.org/10.1177/1087057111418653

Saunier, E., Benelli, C., & Bortoli, S. (2016). The pyruvate dehydrogenase complex in cancer: An old metabolic gatekeeper regulated by new pathways and pharmacological agents. *International Journal of Cancer*, *138*(4), 809-817. https://doi.org/https://doi.org/10.1002/ijc.29564

Schiliro, C., & Firestein, B. L. (2021). Mechanisms of Metabolic Reprogramming in Cancer Cells Supporting Enhanced Growth and Proliferation. *Cells*, *10*(5). https://doi.org/10.3390/cells10051056

Schindelin, J., Arganda-Carreras, I., Frise, E., Kaynig, V., Longair, M., Pietzsch, T., Preibisch, S., Rueden, C., Saalfeld, S., Schmid, B., Tinevez, J.-Y., White, D. J., Hartenstein, V., Eliceiri, K., Tomancak, P., & Cardona, A. (2012). Fiji: an open-source platform for biological-image analysis. *Nature Methods*, *9*(7), 676-682. https://doi.org/10.1038/nmeth.2019

Schwaiger, M., Rampler, E., Hermann, G., Miklos, W., Berger, W., & Koellensperger, G. (2017). Anion-Exchange Chromatography Coupled to High-Resolution Mass Spectrometry: A Powerful Tool for Merging Targeted and Non-targeted Metabolomics. *Anal Chem*, *89*(14), 7667-7674. https://doi.org/10.1021/acs.analchem.7b01624

Shi, L., & Tu, B. P. (2015). Acetyl-CoA and the regulation of metabolism: mechanisms and consequences. *Curr Opin Cell Biol*, *33*, 125-131. https://doi.org/10.1016/j.ceb.2015.02.003

Shvedunova, M., & Akhtar, A. (2022). Modulation of cellular processes by histone and non-histone protein acetylation. *Nature Reviews Molecular Cell Biology*, *23*(5), 329-349. https://doi.org/10.1038/s41580-021-00441-y

Singer, H. S., Mink, J. W., Gilbert, D. L., & Jankovic, J. (2016). Chapter 17 - Inherited Metabolic Disorders with Associated Movement Abnormalities. In H. S. Singer, J. W. Mink, D. L. Gilbert, & J. Jankovic (Eds.), *Movement Disorders in Childhood (Second Edition)* (pp. 337-407). Academic Press. https://doi.org/https://doi.org/10.1016/B978-0-12-411573-6.00017-6

Sivanand, S., Viney, I., & Wellen, K. E. (2018). Spatiotemporal Control of Acetyl-CoA Metabolism in Chromatin Regulation. *Trends Biochem Sci*, *43*(1), 61-74. https://doi.org/10.1016/j.tibs.2017.11.004

Škerlová, J., Berndtsson, J., Nolte, H., Ott, M., & Stenmark, P. (2021). Structure of the native pyruvate dehydrogenase complex reveals the mechanism of substrate insertion. *Nature Communications*, *12*(1), 5277. https://doi.org/10.1038/s41467-021-25570-y

Stacpoole, P. W. (2017). Therapeutic Targeting of the Pyruvate Dehydrogenase Complex/Pyruvate Dehydrogenase Kinase (PDC/PDK) Axis in Cancer. *JNCI: Journal of the National Cancer Institute*, *109*(11), djx071. https://doi.org/10.1093/jnci/djx071

Sudarsan, S., Dethlefsen, S., Blank, L. M., Siemann-Herzberg, M., & Schmid, A. (2014). The functional structure of central carbon metabolism in Pseudomonas putida KT2440. *Appl Environ Microbiol*, *80*(17), 5292-5303. https://doi.org/10.1128/aem.01643-14

Sumegi, B., Liposits, Z., Inman, L., Paull, W. K., & Srere, P. A. (1987). Electron microscopic study on the size of pyruvate dehydrogenase complex in situ. *European Journal of Biochemistry*, *169*(1), 223-230. https://doi.org/https://doi.org/10.1111/j.1432-1033.1987.tb13601.x

Sun, R. C., & Denko, N. C. (2014). Hypoxic regulation of glutamine metabolism through HIF1 and SIAH2 supports lipid synthesis that is necessary for tumor growth. *Cell Metab*, *19*(2), 285-292. https://doi.org/10.1016/j.cmet.2013.11.022

Sun, X. J., Man, N., Tan, Y., Nimer, S. D., & Wang, L. (2015). The Role of Histone Acetyltransferases in Normal and Malignant Hematopoiesis. *Front Oncol*, *5*, 108. https://doi.org/10.3389/fonc.2015.00108

Sutendra, G., Kinnaird, A., Dromparis, P., Paulin, R., Stenson, Trevor H., Haromy, A., Hashimoto, K., Zhang, N., Flaim, E., & Michelakis, Evangelos D. (2014). A Nuclear Pyruvate Dehydrogenase Complex Is Important for the Generation of Acetyl-CoA and Histone Acetylation. *Cell*, *158*(1), 84-97. https://doi.org/https://doi.org/10.1016/j.cell.2014.04.046

Takahashi, H., McCaffery, J. M., Irizarry, R. A., & Boeke, J. D. (2006). Nucleocytosolic acetyl-coenzyme a synthetase is required for histone acetylation and global transcription. *Mol Cell*, *23*(2), 207-217. https://doi.org/10.1016/j.molcel.2006.05.040

Tan, L., Martinez, S. A., Lorenzi, P. L., & Karlstaedt, A. (2023). Quantitative Analysis of Acetyl-CoA, Malonyl-CoA, and Succinyl-CoA in Myocytes. *J Am Soc Mass Spectrom*. https://doi.org/10.1021/jasms.3c00278

Tan, M., Mosaoa, R., Graham, G. T., Kasprzyk-Pawelec, A., Gadre, S., Parasido, E., Catalina-Rodriguez, O., Foley, P., Giaccone, G., Cheema, A., Kallakury, B., Albanese, C., Yi, C., & Avantaggiati, M. L. (2020). Inhibition of the mitochondrial citrate carrier, Slc25a1, reverts steatosis, glucose intolerance, and inflammation in preclinical models of NAFLD/NASH. *Cell Death & Differentiation*, *27*(7), 2143-2157. https://doi.org/10.1038/s41418-020-0491-6

Tanner, L. B., Goglia, A. G., Wei, M. H., Sehgal, T., Parsons, L. R., Park, J. O., White, E., Toettcher, J. E., & Rabinowitz, J. D. (2018). Four Key Steps Control Glycolytic Flux in Mammalian Cells. *Cell Systems*, *7*(1), 49-62.e48. https://doi.org/10.1016/j.cels.2018.06.003

Tebani, A., Afonso, C., Marret, S., & Bekri, S. (2016). Omics-Based Strategies in Precision Medicine: Toward a Paradigm Shift in Inborn Errors of Metabolism Investigations. *Int J Mol Sci*, *17*(9). https://doi.org/10.3390/ijms17091555

Tessarz, P., & Kouzarides, T. (2014). Histone core modifications regulating nucleosome structure and dynamics. *Nature Reviews Molecular Cell Biology*, *15*(11), 703-708. https://doi.org/10.1038/nrm3890

Trefely, S., Huber, K., Liu, J., Noji, M., Stransky, S., Singh, J., Doan, M. T., Lovell, C. D., von Krusenstiern, E., Jiang, H., Bostwick, A., Pepper, H. L., Izzo, L., Zhao, S., Xu, J. P., Bedi, K. C., Rame, J. E., Bogner-Strauss, J. G., Mesaros, C., . . . Snyder, N. W. (2022). Quantitative subcellular acyl-CoA analysis reveals distinct nuclear metabolism and isoleucine-dependent histone propionylation. *Molecular Cell*, *82*(2), 447-462.e446. https://doi.org/https://doi.org/10.1016/j.molcel.2021.11.006

Van der Kamp, M. W. (2013). Citrate Synthase – Computational Studies. In G. C. K. Roberts (Ed.), *Encyclopedia of Biophysics* (pp. 318-320). Springer Berlin Heidelberg. https://doi.org/10.1007/978-3-642-16712-6_229

van Kuppeveld, F. J., van der Logt, J. T., Angulo, A. F., van Zoest, M. J., Quint, W. G., Niesters, H. G., Galama, J. M., & Melchers, W. J. (1993). Genus- and species-specific identification of mycoplasmas by 16S rRNA amplification. *Appl Environ Microbiol*, *59*(2), 655. https://doi.org/10.1128/aem.59.2.655-.1993

van Roermund, C. W., Elgersma, Y., Singh, N., Wanders, R. J., & Tabak, H. F. (1995). The membrane of peroxisomes in Saccharomyces cerevisiae is impermeable to NAD(H) and acetyl-CoA under in vivo conditions. *Embo j*, *14*(14), 3480-3486. https://doi.org/10.1002/j.1460-2075.1995.tb07354.x

Vander Heiden, M. G., Cantley, L. C., & Thompson, C. B. (2009). Understanding the Warburg effect: the metabolic requirements of cell proliferation. *Science*, *324*(5930), 1029-1033. https://doi.org/10.1126/science.1160809

Vanderhaeghen, T., Vandewalle, J., & Libert, C. (2020). Hypoxia-inducible factors in metabolic reprogramming during sepsis. *Febs j*, *287*(8), 1478-1495. https://doi.org/10.1111/febs.15222

Vaupel, P., & Multhoff, G. (2021). Revisiting the Warburg effect: historical dogma versus current understanding. *The Journal of Physiology*, *599*(6), 1745-1757. https://doi.org/https://doi.org/10.1113/JP278810

Violante, S., Berisa, M., Thomas, T. H., & Cross, J. R. (2019). Stable Isotope Tracers for Metabolic Pathway Analysis. In A. D'Alessandro (Ed.), *High-Throughput Metabolomics: Methods and Protocols* (pp. 269-283). Springer New York. https://doi.org/10.1007/978-1-4939-9236-2_17

Wagner, B. A., Venkataraman, S., & Buettner, G. R. (2011). The rate of oxygen utilization by cells. *Free Radic Biol Med*, *51*(3), 700-712. https://doi.org/10.1016/j.freeradbiomed.2011.05.024

Wang, Y., Yang, H., Geerts, C., Furtos, A., Waters, P., Cyr, D., Wang, S., & Mitchell, G. A. (2023). The multiple facets of acetyl-CoA metabolism: Energetics, biosynthesis, regulation, acylation and inborn errors. *Mol Genet Metab*, *138*(1), 106966. https://doi.org/10.1016/j.ymgme.2022.106966

Wang, Y., Yu, W., Li, S., Guo, D., He, J., & Wang, Y. (2022). Acetyl-CoA Carboxylases and Diseases. *Front Oncol*, *12*, 836058. https://doi.org/10.3389/fonc.2022.836058

Weidemann, A., & Johnson, R. S. (2008). Biology of HIF-1α. *Cell Death & Differentiation*, *15*(4), 621-627. https://doi.org/10.1038/cdd.2008.12

Wellen, K. E., Hatzivassiliou, G., Sachdeva, U. M., Bui, T. V., Cross, J. R., & Thompson, C. B. (2009). ATP-citrate lyase links cellular metabolism to histone acetylation. *Science*, *324*(5930), 1076-1080. https://doi.org/10.1126/science.1164097

Wenger, R. H., Stiehl, D. P., & Camenisch, G. (2005). Integration of Oxygen Signaling at the Consensus HRE. *Science's STKE*, *2005*(306), re12-re12. https://doi.org/10.1126/stke.3062005re12

Wheaton, W. W., & Chandel, N. S. (2011). Hypoxia. 2. Hypoxia regulates cellular metabolism. *Am J Physiol Cell Physiol*, *300*(3), C385-393. https://doi.org/10.1152/ajpcell.00485.2010

Wong, C. C., Qian, Y., & Yu, J. (2017). Interplay between epigenetics and metabolism in oncogenesis: mechanisms and therapeutic approaches. *Oncogene*, *36*(24), 3359-3374. https://doi.org/10.1038/onc.2016.485

Wong, J. M., Malec, P. A., Mabrouk, O. S., Ro, J., Dus, M., & Kennedy, R. T. (2016). Benzoyl chloride derivatization with liquid chromatography-mass spectrometry for targeted metabolomics of neurochemicals in biological samples. *J Chromatogr A*, *1446*, 78-90. https://doi.org/10.1016/j.chroma.2016.04.006

Woolbright, B. L., Choudhary, D., Mikhalyuk, A., Trammel, C., Shanmugam, S., Abbott, E., Pilbeam, C. C., & Taylor, J. A., 3rd. (2018). The Role of Pyruvate Dehydrogenase Kinase-4 (PDK4) in Bladder Cancer and Chemoresistance. *Mol Cancer Ther*, *17*(9), 2004-2012. https://doi.org/10.1158/1535-7163.Mct-18-0063

Wu, Z., Liang, X., Li, M., Ma, M., Zheng, Q., Li, D., An, T., & Wang, G. (2023). Advances in the optimization of central carbon metabolism in metabolic engineering. *Microb Cell Fact*, *22*(1), 76. https://doi.org/10.1186/s12934-023-02090-6

Yang, X., Ma, Y., Li, N., Cai, H., & Bartlett, M. G. (2017). Development of a Method for the Determination of Acyl-CoA Compounds by Liquid Chromatography Mass Spectrometry to Probe the Metabolism of Fatty Acids. *Anal Chem*, *89*(1), 813-821. https://doi.org/10.1021/acs.analchem.6b03623

Zaidi, N., Swinnen, J. V., & Smans, K. (2012). ATP-citrate lyase: a key player in cancer metabolism. *Cancer Res*, *72*(15), 3709-3714. https://doi.org/10.1158/0008-5472.Can-11-4112

Zaikin, V. G., & Borisov, R. S. (2021). Mass Spectrometry as a Crucial Analytical Basis for Omics Sciences. *Journal of Analytical Chemistry*, *76*(14), 1567-1587. https://doi.org/10.1134/S1061934821140094

Zamboni, N., Fendt, S.-M., Rühl, M., & Sauer, U. (2009). 13C-based metabolic flux analysis. *Nature Protocols*, *4*(6), 878-892. https://doi.org/10.1038/nprot.2009.58

Zamboni, N., Saghatelian, A., & Patti, G. J. (2015). Defining the metabolome: size, flux, and regulation. *Mol Cell*, *58*(4), 699-706. https://doi.org/10.1016/j.molcel.2015.04.021

Zenewicz, L. A. (2017). Oxygen Levels and Immunological Studies. *Front Immunol*, *8*, 324. https://doi.org/10.3389/fimmu.2017.00324

Zhang, T., Cooper, S., & Brockdorff, N. (2015). The interplay of histone modifications - writers that read. *EMBO Rep*, *16*(11), 1467-1481. https://doi.org/10.15252/embr.201540945

Zhang, T., Zhang, Z., Dong, Q., Xiong, J., & Zhu, B. (2020). Histone H3K27 acetylation is dispensable for enhancer activity in mouse embryonic stem cells. *Genome Biology*, *21*(1), 45. https://doi.org/10.1186/s13059-020-01957-w

Zhao, S., Torres, A., Henry, R. A., Trefely, S., Wallace, M., Lee, J. V., Carrer, A., Sengupta, A., Campbell, S. L., Kuo, Y. M., Frey, A. J., Meurs, N., Viola, J. M., Blair, I. A., Weljie, A. M., Metallo, C. M., Snyder, N. W., Andrews, A. J., & Wellen, K. E. (2016). ATP-Citrate Lyase Controls a Glucose-to-Acetate Metabolic Switch. *Cell Rep*, *17*(4), 1037-1052. https://doi.org/10.1016/j.celrep.2016.09.069

Zhou, V. W., Goren, A., & Bernstein, B. E. (2011). Charting histone modifications and the functional organization of mammalian genomes. *Nature Reviews Genetics*, *12*(1), 7-18. https://doi.org/10.1038/nrg2905

Zhou, Y., Zhou, B., Pache, L., Chang, M., Khodabakhshi, A. H., Tanaseichuk, O., Benner, C., & Chanda, S. K. (2019). Metascape provides a biologist-oriented resource for the analysis of systems-level datasets. *Nature Communications*, *10*(1), 1523. https://doi.org/10.1038/s41467-019-09234-6

9 SUPPLEMENTARY MATERIAL

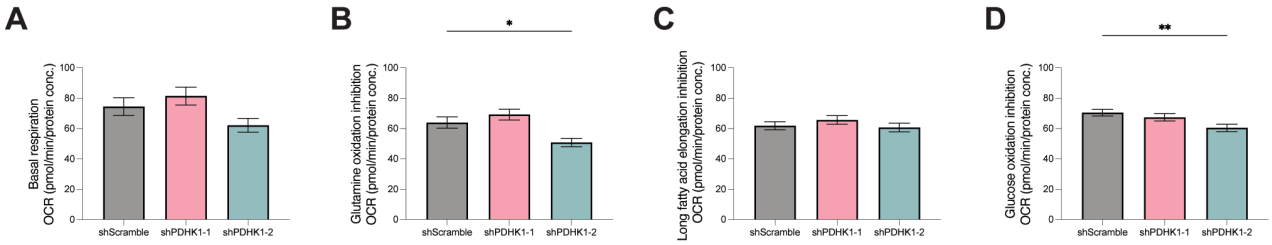

Figure S1. The oxygen consumption rate (OCR) remains constant in PDHK1-KD cells.

(A) OCR measured in basal respiration, **(B)** glutaminolysis inhibition, **(C)** FAO inhibition, and (E) glucose oxidation inhibition from hypoxia-cultured NIH-3T3 cells expressing short hairpin PDHK1 (shPDHK1 and shPDHK1-2) and scramble RNA (shScramble). Data is represented as individual values ± S.E.M. Significance was defined as follows: n.s. (not shown abbreviation) > 0.05; *p≤ 0.05, and **p≤ 0.01, as assessed by two-way ANOVA.

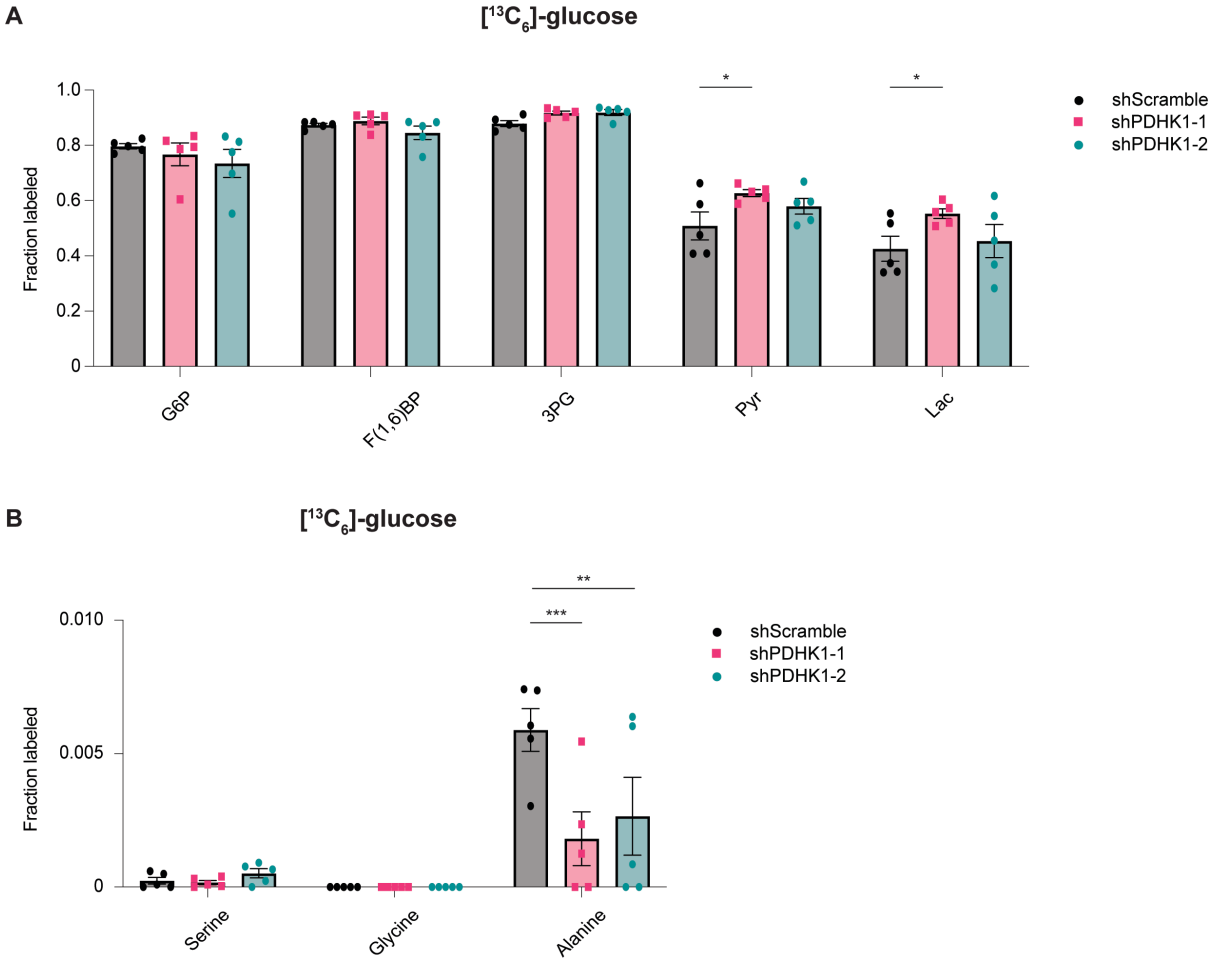

Figure S2. PDHK1 deficiency has no impact on glycolytic-metabolites synthesis.

(A) [$^{13}C_6$]-glucose-derived labeling in glycolytic intermediates and, **(B)** glycolysis-derived amino acids from hypoxia-cultured NIH-3T3 cells expressing short hairpin PDHK1 (shPDHK1 and shPDHK1-2) and scramble RNA (shScramble). Data is represented as individual values ± S.E.M. Significance was defined as follows: n.s. (not shown abbreviation) > 0.05; *p≤ 0.05; **p≤ 0.01; and ***p≤ 0.001, as assessed by two-way ANOVA. Abbreviations: G6P – Glucose-6-phosphate, F(1,6)BP – Fructose-1,6-bisphosphate, 3PG – 3-phosphoglycerate, Pyr – Pyruvate, Lac – Lactate. Mass isotopomers represented are: G6P(m+6), F(1,6)BP (m+6), 3PG (m+3), Pyr (m+3), Lac (m+3), Serine (m+3), Glycine (m+2), Alanine (m+2). (A) Y-max = 1.0; (B) Y-max = 0.010.

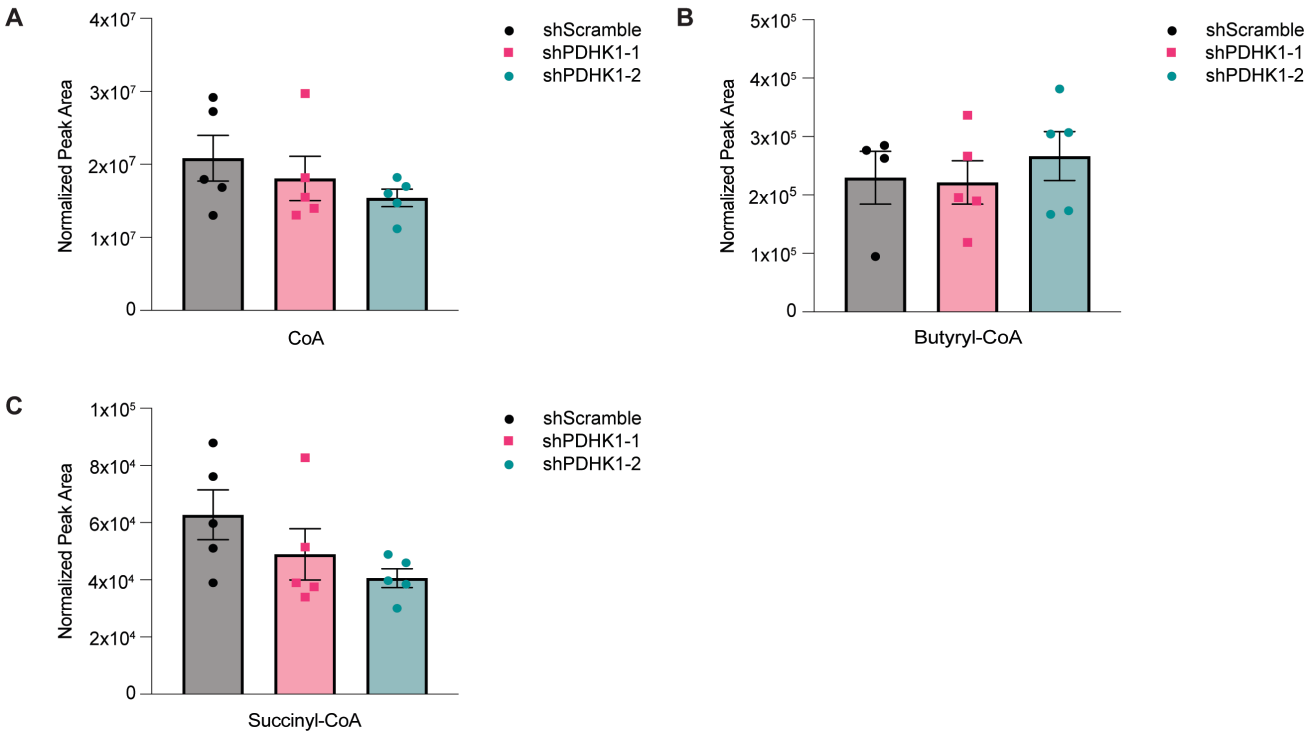

Figure S3. PDHK1 depletion has no impact on small CoA compounds pool size.

(A) Metabolic pool size of CoA, **(B)** butyryl-CoA, and **(C)** succinyl-CoA from hypoxia-cultured NIH-3T3 cells expressing short hairpin PDHK1 (shPDHK1 and shPDHK1-2) and scramble RNA (shScramble). Data is represented as individual values ± S.E.M. Significance was defined as follows: n.s. (not shown abbreviation) > 0.05, as assessed by two-way ANOVA.

Figure S4. The transcriptome is not affected upon PDHK1 depletion.

(A) XXX. **(B)** XXX

9.1 List of Tables

9.2 List of Figures

9.3 List of Abbreviations

General

acetyl-CoA	acetyl-coenzyme A
αKG	alpha-ketoglutarate
BP	biological processes
CCM	central carbon metabolism
CoA	coenzyme A
CoQ9	coenzyme Q9
DCA	dichloroacetate
DG	diacylglycerol
E1	pyruvate dehydrogenase subunit
E2	dihydrolipoamide S-acetyltransferase subunit
E3	dihydrolipoamide dehydrogenase subunit
F6P	fructose-6-phosphate
F(1,6)BP	fructose-1,6-bisphosphate
GO	gene ontology
G3P	glyceraldehyde-3-phosphate
G6P	glucose-6-phosphate
HRE	hypoxia responsive element
K_D	dissociation constant
Lac	lactate
mRNA	messenger RNA
OXPHOS	oxidative phosphorylation
PC	Phosphatidylcholine
3PG	3-phosphoglycerate
PPP	pentose phosphate pathway
PTM	post-translational modification
Pyr	pyruvate
R5P	ribose-5-phosphate
S7P	sedoheptulose-7-phosphate
TCA cycle	tricarboxylic acid cycle

Reagents and methods

ATAC-Seq	transposase-accessible chromatin with sequencing

ChIP-Seq	Chromatin Immunoprecipitation Sequencing
ECAR	extracellular acidification rate
FBS	fetal bovine serum
FCCP	carbonyl cyanide-p-trifuoromethoxyphenyl-hydrazone
GC	gas-chromatography
HPLC	high-performance liquid chromatography
KD	knockdown
KO	knockout
OCR	oxygen consumption rate
LC-MS	liquid chromatography – mass spectrometry
MS	mass - spectrometry
NGS	next-generation sequencing
qRT-PCR	real-time quantitative reverse transcription-PCR
RNAi	RNA interference
RNA-seq	RNA-sequencing
S.E.M.	standard error of the mean
SILEC-SF	stable isotope labeling of essential nutrients in cell culture-subcellular fractionation
TMT	tandem mass tag

Gene and protein names

ACC1	acetyl-CoA carboxylase 1
ACC2	acetyl-CoA carboxylase 2
P-ACC1	phosphorylated (Ser79) acetyl-CoA carboxylase 1
P-ACC2	phosphorylated (Ser212) acetyl-CoA carboxylase 2
ACLY	ATP citrate lyase
ACSS2	acetyl-CoA synthetase short-chain family member 2
AMPK	AMP-activated protein kinase
E3BP	E3-binding protein
FASN	fatty acid synthase
HATs	histone acetyltransferases
HDACs	histone deacetylases
HIF1α	hypoxia-inducible factor 1-alpha
HIF1β	hypoxia-inducible factor 1-beta

HMTs	histone methyltransferases
LDHA	lactate dehydrogenase A
PHDs	prolyl-hydroxylases
PDH	pyruvate dehydrogenase
PDHK1	pyruvate dehydrogenase kinase 1
Pdk1	*pyruvate dehydrogenase kinase 1*
PDP	pyruvate dehydrogenase phosphatase
SLC25A1	tricarboxylate transport protein
pVHL	von Hippel Lindau protein

10 ERKLÄRUNG

Erklärung zur Dissertation
gemäß der Promotionsordnung vom 12. März 2020

Diese Erklärung muss in der Dissertation enthalten sein.
(This version must be included in the doctoral thesis)

„Hiermit versichere ich an Eides statt, dass ich die vorliegende Dissertation selbstständig und ohne die Benutzung anderer als der angegebenen Hilfsmittel und Literatur angefertigt habe. Alle Stellen, die wörtlich oder sinngemäß aus veröffentlichten und nicht veröffentlichten Werken dem Wortlaut oder dem Sinn nach entnommen wurden, sind als solche kenntlich gemacht. Ich versichere an Eides statt, dass diese Dissertation noch keiner anderen Fakultät oder Universität zur Prüfung vorgelegen hat; dass sie - abgesehen von unten angegebenen Teilpublikationen und eingebundenen Artikeln und Manuskripten - noch nicht veröffentlicht worden ist sowie, dass ich eine Veröffentlichung der Dissertation vor Abschluss der Promotion nicht ohne Genehmigung des Promotionsausschusses vornehmen werde. Die Bestimmungen dieser Ordnung sind mir bekannt. Darüber hinaus erkläre ich hiermit, dass ich die Ordnung zur Sicherung guter wissenschaftlicher Praxis und zum Umgang mit wissenschaftlichem Fehlverhalten der Universität zu Köln gelesen und sie bei der Durchführung der Dissertation zugrundeliegenden Arbeiten und der schriftlich verfassten Dissertation beachtet habe und verpflichte mich hiermit, die dort genannten Vorgaben bei allen wissenschaftlichen Tätigkeiten zu beachten und umzusetzen. Ich versichere, dass die eingereichte elektronische Fassung der eingereichten Druckfassung vollständig entspricht."

Teilpublikationen:

05/06/23

Datum, Name und Unterschrift

11 Curriculum vitae

Claudia Tonantzi Sandoval Silva

Date of birth: May 3rd, 1989
Country of birth: Mexico
Nationality: Mexican

Max Planck Institute for Biology of Ageing
Department of Chromatin and Ageing
Joseph-Stelzmann-Str. 9b
50931 Cologne, Germany
csilva@age.mpg.de
+49 (0) 221 37970 686

UNIVERSITY EDUCATION

Feb 2018 – Present	**University of Cologne (UoC)** Ph.D. in Molecular Biology and Genetics	Cologne, Germany
Sep 2015 – Oct 2017	**Radboud University (RU)** M.Sc. in Molecular Life Sciences	Nijmegen, The Netherlands
Aug 2009 – Aug 2014	**National Autonomous University of Mexico (UNAM)** B.Sc. in Biology	Mexico City, Mexico

RESEARCH EXPERIENCE

2018 – Present — **Max Planck Institute for Biology of Ageing**
Department of Chromatin and Ageing
Graduate Researcher: "Catch me if you can: understanding the role of metabolism in chromatin dynamics"
Advisor: Dr. Peter Tessarz

2017 — **Max Planck Institute for Biology of Ageing**
Department of Chromatin and Ageing
Intern Researcher (Master): "RNA-mediated regulation of the histone chaperone FACT".
Advisor: Dr. Peter Tessarz

2016 — **Radboud University Nijmegen**
Radboud Institute of Molecular Life Sciences
Intern Researcher (Master): "Molecular characterization of CFBb-MYH11 and MLL-AF9 using human iPSCs".
Advisor: Dr. Joost Martens

2012 - 2015 — **Institute of Biology, UNAM**
Department of Ecological Restoration
Undergraduate Researcher: "Reproductive analysis of *Oreochromis niloticus* in Xochimilco Wetland System".
Advisor: Dr. Luis Zambrano González

2013 — **Institute of Biology, UNAM**
Department of Ecology and Natural Resources
Undergraduate Researcher: "The adaptive meaning of superfoetation in viviparous fishes of the Poeciliidae Family".
Advisor: Prof. Dr. Jaime Zúñiga Vega

2011 — **Institute of Marine Sciences and Limnology, UNAM**
Department of Environmental Chemistry
Intern Researcher (Bachelor): "Life cycle generalities and morphological features of *Streptomyces sp.*".
Advisor: Prof. Dr. Luis Maldonado Manjarréz

PUBLICATIONS

- Pouikli A., Maleszewska M., Parekh S., Nikopoulou C., Bonfiglio J., Mylonas C., **Sandoval T.,** Schumacher A-L, Hinze Y., Matic I. and Tessarz P. **Hypoxia promotes osteogenesis via regulation of the mito-nuclear communication.** *EMBO J,* 2022.

- Nikopoulou C., Kleinenkuhnen N., Parekh S., **Sandoval T.,** Schneider F., Giavalisco P., Bozukova M., Vesting A-J., Altmueller J., Wunderlich T., Kondylis V., Tresch T., and Tessarz P. **Single-cell resolution unravels spatial alterations in metabolism, transcriptome and epigenome of ageing liver.** *Nature Aging,* (in press).

HONORS AND AWARDS

2022	Minerva Travel Grant – Workshop on Metabolism and Ageing Minerva Ageing Research Center
2016 - 2017	Master Research Program Fellowship – Foreign Research Fellowship Science Council of Mexico, CONACYT
2015 – 2017	Master Research Program Fellowship – Orange Tulip Scholarship Netherlands Education Support Office
2017	Radboud Max-Planck Grant Radboud University and Max Planck Society
2017	Erasmus+ Traineeships Erasmus+ Programme
2015	Bruce Stewart Travel Award – Annual Meeting of the Southwestern Association of Naturalists Southwestern Association of Naturalists
2014	Academic Scholarship – VI National Congress of Limnology Institute of Marine Sciences and Limnology, UNAM

SCIENTIFIC MEETINGS

Oral	Minerva and ISF Workshop on Metabolism and Ageing Minerva Research Center, Tel-Aviv, Israel (Nov 2022)
	62th Annual Meeting of the Southwestern Association of Naturalists San Diego State University, California, USA (April 2015)
	II International Congress of Aquaculture Veterinary Medicine School, UNAM, Acapulco, Mexico (Nov 2014)
Poster	EMBO | EMBL Symposium: Metabolism meets Epigenetics EMBO, Heidelberg, Germany (Nov 2019).
	VI National Congress of Limnology Institute of Marine Sciences and Limnology, Mexico City, Mexico (Nov 2014)

RESEARCH SKILLS

Cell culture	• Human induced pluripotent stem cells (hiPSCs), human embryonal kidney cells (HEK293), mouse embryonic stem cells (mESCs), mouse mesenchymal stem cells (MSCs), mouse liver organoids, mouse embryonic fibroblasts (MEFs) and, NIH Swiss mouse embryo fibroblast (NIH-3T3).

Cell line characterization	• DNA and RNA extraction, PCR and qRT-PCR, siRNA lipofectamine transfection and, shRNA lentiviral production and transduction, CRISPR-Cas9 design using crRNA • Peptide preparation for LC/MS proteomics, total protein extraction, core histones purification, SDS-PAGE analysis for Western Blotting.
NGS	• RNA-seq, CUT&RUN sequencing, cross-linking immunoprecipitation (CLIP-seq).
Microscopy	• Fixed cell imaging using phase contrast, fluorescence, and confocal systems (Leica) • High-throughput cell density screening by automated microscopy (EVOS), subsequent machine learning data acquisition (iLASTIK) and image analysis (Fiji).
Molecular cloning	• Experimental design, ligation and transformation of mouse codon-optimized DNA fragments or donor plasmid DNA into *E. coli* strains • Competent cell preparation, transformation and plasmid extraction (Mini/Maxi-Prep)

MANAGEMENT AND COMMUNICATION SKILLS

Management	• Managed the annual Ph.D. students' budget to organize academic workshops with externals including payroll processing and accounts payable management responsibilities. • Established and maintained a detailed inventory system that included an updated ordering and supplies allocation scheme. • Co-managed a science communication seminar budget and logistics.
Communication	• Presented scientific research to specialized and general audience in English and Spanish. • Wrote theses and grant applications in English and Spanish. • Collaborated with senior managers to select and schedule workshops for Ph.D. students.

WORKSHOPS AND RESEARCH TRAINING

- Good Manufacturing Practice (GMP academy).
- International Female Scholars (University of Cologne, Cologne).
- Statistical Literacy (Science Craft, Cologne).
- Adobe Illustrator Course (Amselrehhase, Cologne).
- CRISPR/Cas9 – Genome Editing (CEPLAS, Düsseldorf).
- Advanced Scientific Writing (BioScript, Cologne).
- Intercultural communication (Max Planck Institute for Biology of Ageing).

COMPUTER SKILLS

- GraphPad Prism (statistical analysis)
- R-Studio (basic plotting)
- Fiji and iLASTIK (image analysis)
- SnapGene (molecular biology)
- Microsoft Office Suite (Word, Excel, Power Point)
- Adobe Creative Cloud (Adobe Illustrator)
- Team communication tools (Slack and Zoom)
- Inventory Management (Quartzy)

LANGUAGE SKILLS

- Spanish | Native Speaker
- English | Professional Proficiency
- German | Intermediate (B1.1)